CHARACTERIZATION OF NANOPETROPHYSICAL PROPERTIES OF THE MANCOS "B"/ PRAIRIE CANYON MEMBER OF THE MANCOS SHALE, RIO BLANCO, COLORADO

By

SCOTT BRIAN LEASEBURGE

Presented to the Faculty of the Graduate School of

The University of Texas at Arlington in Partial Fulfillment

of the Requirements

for the Degree of

MASTER OF SCIENCE IN

Geology

THE UNIVERSITY OF TEXAS AT ARLINGTON

November 2017

November 17th, 2017

Acknowledgements

First I would like to thank those at the USGS Core Research Center at the Denver Federal Center in Denver, Colorado. They made the process of collecting samples streamlined and were helpful at every available opportunity. The availability to sample from the Core Research Center contributed significantly to the progress of this study.

I would like to thank all of the members of Dr. Hu's research group, especially Yuxiang Zhang, Kibria Golam, Marvin Dunbar and Dillon Worley for their help. There was always a willingness to provide support and to help troubleshoot any issues that arose during experiments. Also collaborating laboratories at the China University of Geoscience (CUG) and Chengdu University of Technology (CDUT) for various sample analyses.

I would like to especially thank Dr. Q.H. Hu, the advisor of this project. I very much appreciate the opportunity to work in this research group on a topic that brings many of my interests together. Through his guidance, research, and lectures, Dr. Hu has shared a vast wealth of knowledge that was foundational to this project. Also I would like to thank committee members Dr. John Wickham and William J. Moulton for their continued support and willingness to participate in this project.

Lastly I would like to thank my loving mother Lisa Polder Leaseburge. Her love and support were fundamental to my continuing education. During times of trial and rough seas she was always the light that guided to safe harbors.

November 17th, 2017

Abstract

CHARACTERIZATION OF NANOPETROPHYSICAL PROPERTIES OF THE MANCOS "B"/ PRAIRIE CANYON MEMBER OF THE MANCOS SHALE,

RIO BLANCO, COLORADO

Scott Brian Leaseburge

The University of Texas at Arlington, 2017

Supervising Professor: Q.H. Hu

Over the past decade hydrocarbon production from unconventional reservoirs has grown to become a significant source of North American domestic energy and will likely continue so for decades to come. However, production from unconventional reservoirs is plagued with low overall recovery and sharp declines in production. Low matrix permeability and poor pore connectively are significant factors limiting recovery and production. Research into the fluid flow characteristics of low permeability reservoirs can lead to extended initial production and greater overall recovery.

Technically recoverable unconventional oil and gas resources in the Mancos Shale of the Piceance Basin are estimated to be 66.3 tcf of natural gas, 74 million barrels of oil and 45 million barrels of natural gas liquids. The informally named Mancos "B" is an anomalously sandy interval of the Manos Shale deposited during the Late Cretaceous as a pro-delta plume. The Mancos "B" forms upward coarsening sequences consisting of mainly clastic sediments. The Mancos "B" has been a producing interval in the Douglas Creek Arch region of northwest Colorado since the late 1950's.

This research focuses on the informal interval, Mancos “B”, sampled from three wells across Rio Blanco, Colorado. This study used a variety of methods that includes: X-Ray diffraction (XRD), total organic carbon (TOC), pyrolysis, core plug helium porosity and permeably, mercury intrusion capillary pressure (MICP), nitrogen gas physisorption, field emission-scanning electron microscopy (FE-SEM), fluid contact angle, and fluid imbibition.

The pore-size distributions of samples fell into two types. Type A distribution consists of a major peak between 500nm-800nm and a minor peak between 10nm-50nm. Type B pore-size distribution entails a single peak at approximately 10nm-50nm. Maturity plays a role in the development of organic hosted porosity (typically 10nm-50nm), but parameters such as lithofacies, as well as TOC content and kerogen type, are contributing variables to how the porosity evolves during maturation. Factors such as maturity, mineral composition, TOC, and depth/burial history all play a role in the final equation of a rock’s pore structure and surface-fluid characteristics. Lithofacies was found to likely be the strongest control on pore-size distribution type.

Samples tended to show a mixed wettability which is likely the result of a combination of hydrophilic minerals supported pore networks and hydrophobic organic matter-hosted pore networks. Imbibition results showed that type A samples had well-connected pore networks for both DI water and n-decane based on stage III slopes. Type B samples tended to have low DI water stage III slopes (0.1-0.3) and relatively high (0.4-0.5) n-decane stage III slopes. This suggests that type B samples have an affinity to contain a well-connected oil-wetting pore system likely due to the porosity that developed in organic matter during maturation but do not have the well-connected water-wetting pore networks that type A samples have. Type A’s well-connected pore networks are likely a result of lithofacies and the main distinction between type B samples.

Table of Contents

List of Figures

List of Tables

Chapter 1

Introduction

Natural gas plays a key role in the energy demands of the Unites States and will continue to do so for decades to come. The Energy Information Administration (EIA) estimated that the Unites States has over 1,744 trillion cubic feet (tcf) of technically recoverable natural gas including 211 tcf of proved reserves (DOE, 2009). Unconventional reservoirs will likely play a significant role in future natural gas and oil production. Onshore technically recoverable unconventional gas, such as shale gas, tight sands, and coalbed methane, account for approximately 60% of recoverable resources (DOE, 2009). Current recovery rates are relatively low with major gas producing shales producing only 12% to 30% of the estimated gas in place and only 5%-10% of oil in place (Hu et al., 2015b). Along with the low recovery rates, there is a drastic decline that shale reservoirs experience after initial production.

The Eagle Ford Shale of Texas, for example, experiences a decline of approximately 70% over the first year of production (Guo et al., 2016). Low recovery and drastic declines in production make it necessary to drill many wells to maintain production. The reasons for large decreases in initial production and low recovery of hydrocarbons in place are partly due to low matrix permeability and diffusion in shale. Hydraulic fracture simulation is necessary to create a large fracture network from which production can occur (Chong et al, 2010). Gas production is likely limited by diffusive transport from matrix storage to the fracture network (Hu et al., 2015a) Therefore research into the pore structure and fluid migration in shales is of considerable importance in order to develop production methods that sustain initial production and allow greater recovery rates.

The Mancos shale was deposited in offshore and open-marine environments of the Cretaceous Interior Seaway during the Late Cretaceous. Dominated by mudrock, the Mancos

Shale formed thick deposits with some areas reaching accumulations of over 5,000 feet in areas of Utah (Kirschbaum, 2003). These thick accumulations blanket most of the Piceance and Uinta Basins, outlined in red on Figure 1-1. USGS in 2016 estimated that technically recoverable unconventional oil and gas resources in the Mancos Shale of the Piceance Basin are 66.3 tcf of natural gas, 74 million barrels of oil and 45 million barrels of natural gas liquids (USGS, 2016).

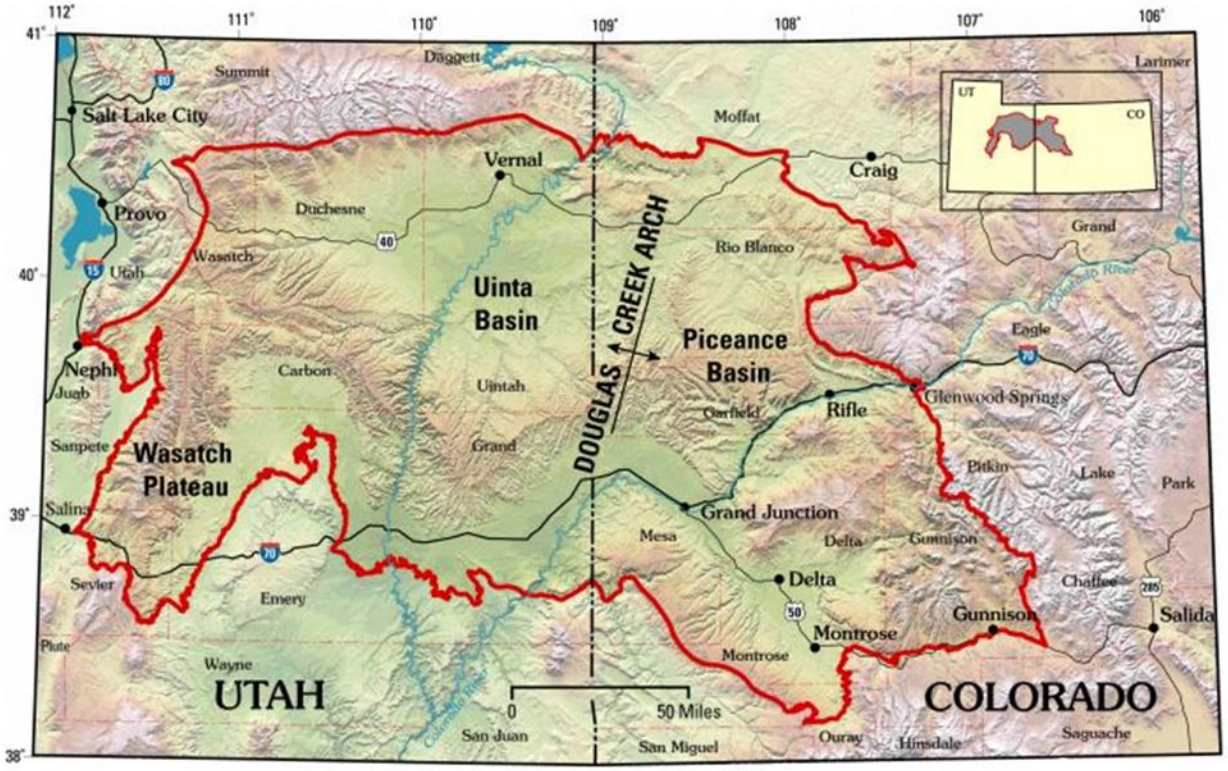

Figure 1-1: Regional map of the Uinta and Piceance Basins (from USGS, 2003).

Considering the significant sediment deposits that make up the entire Mancos Shale, there are many stratigraphic subdivisions. The samples in this study originate from the informally named Mancos “B” unit of the Prairie Canyon Member of the Mancos Shale. The Prairie Canyon Member is located between the upper and lower members of the Blue Gate Member of the Mancos Shale (see Figure 2-4). The Mancos “B”, a sandy interval of the Mancos Shale with oil and gas production, was defined by Kellogg (1977) but initially described by Kopper (1962). The Mancos “B” has been supplying natural gas since the late 1950’s. Early

success was limited due to formation damage and the drilling technology of the time (Kopper, 1962). As seen in Figure 1-2, the Douglas Creek Arch was historically the main area of production from the Mancos “B”. Obtained from the USGS Core Research Center in Denver, Colorado, the samples of this study come from the Mancos “B” interval, from three wells within Rio Blanco county, Colorado as shown in Figure 1-3.

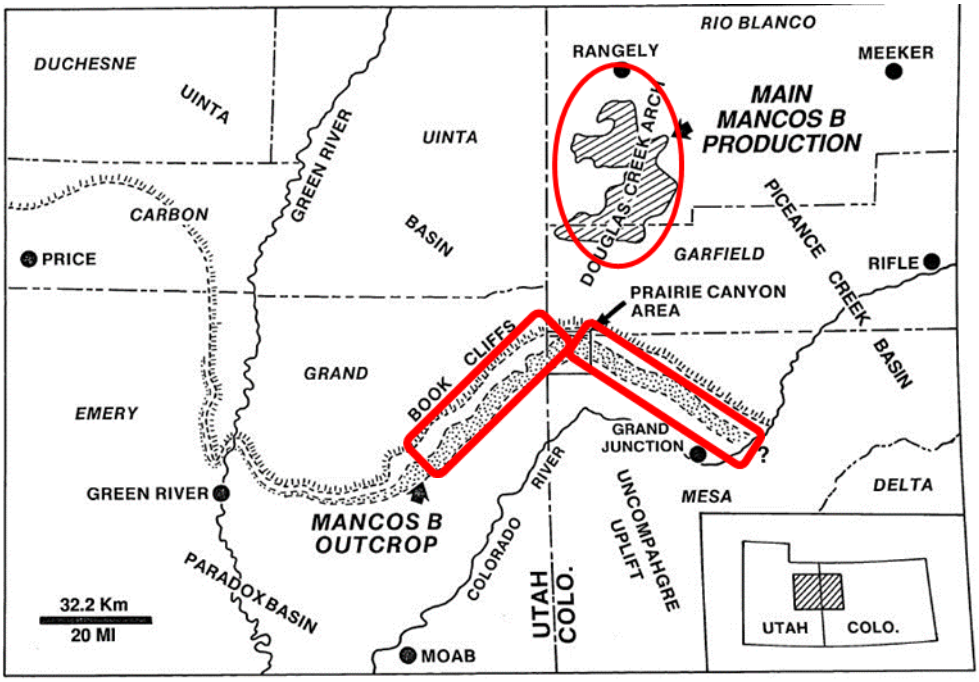

Figure 1-2: Map showing location of outcrops of Mancos “B” and the Douglas Creek Arch, a producing region of the Mancos “B” (from Cole and Young, 1991).

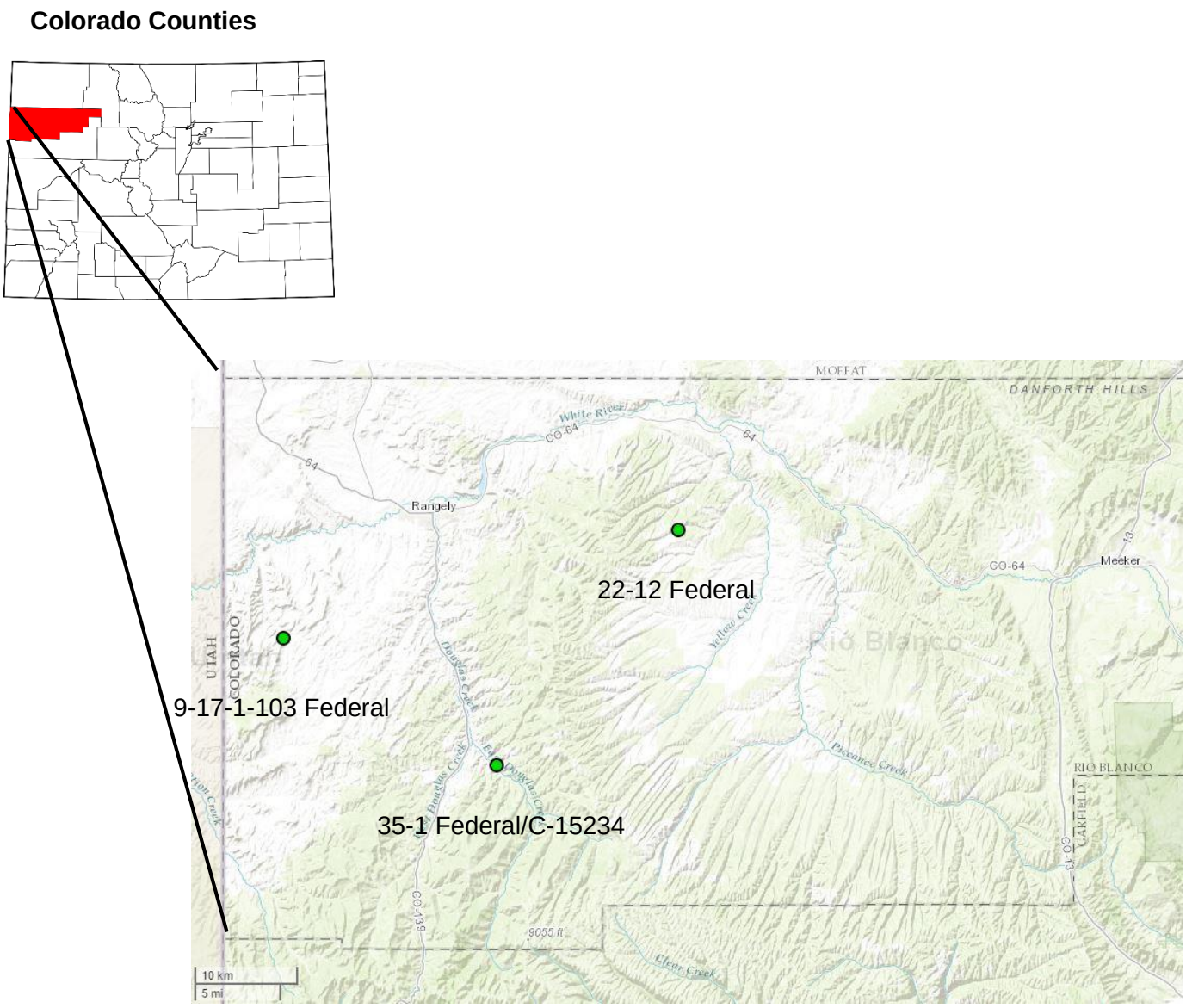

Figure 1-3: Locations of wells that were sampled in western Rio Blanco County. From left (West) to right (East); 9-17-1-103 Federal, 35-1 Federal/C-15234, 22-12 Federal (Drillinginfo.com, 2017).

Chapter 2

Geologic Setting

The Mancos “B” was deposited in the Cretaceous Western Interior Seaway approximately 100 miles from the western shore during the Late Cretaceous as a pro-delta plume (Cole and Young, 1991). Suggested to be a third order parasequence lowstand systems track deposited during eustatic sea level fall, the Mancos “B” contains fourth and fifth order parasequences that typically form upward coarsening gradations from shales to muddy sandstones. These upward coarsening sequences (on the scale from a few to tens of meters) are commonly topped with sandy dolomitic concretions. These concretions are thought to have resulted from periods of slight sea level increase and low sediment supply (Cole and Young, 1991).

Accommodation space for sediments is contributed to the Sevier foreland basin that was the result of thrust-sheet loading in the Sevier orogenic belt. The Sevier orogeny provided eastward thrusting along the Sevier orogenic belt induced by active subduction along the western margin of the North American continent (Johnson, 2003). Basin fill of mostly clastic sediments was produced from the erosion of the Sevier orogenic belt highlands and deposited eastward to the coast by fluvial systems (Hampton, 1999). Deposition of the Upper Mancos Shale, which encompasses the Mancos “B”, coincides with the early stages of the Laramide orogeny in the area. At the end of the Late Cretaceous, the Laramide orogeny created uplifts that segmented the central part of the foreland basin. The “thick skinned” (basement involved thrusts) Laramide orogeny created reverse faults that partitioned the vast Sevier foreland basin into separate smaller basins. The Laramide uplifts, active from the end of the Late Cretaceous through the Eocene, is what is responsible for creating the Uinta and Piceance basins, both of which contain thick deposits of Mancos Shale (Johnson, 2003).

While the Mancos “B” can be traced throughout large regions of Utah and Colorado this study focuses on samples from the Piceance Basin in Rio County, Colorado. The Mancos “B” is estimated to be deposited 100 miles east of the latest Santonian to late-early Campanian shoreline below storm base (Cole et al., 1997). Figure 2-1 from Robert and Kirschbaum (1995) shows the paleogeography of the region during early Campanian age.

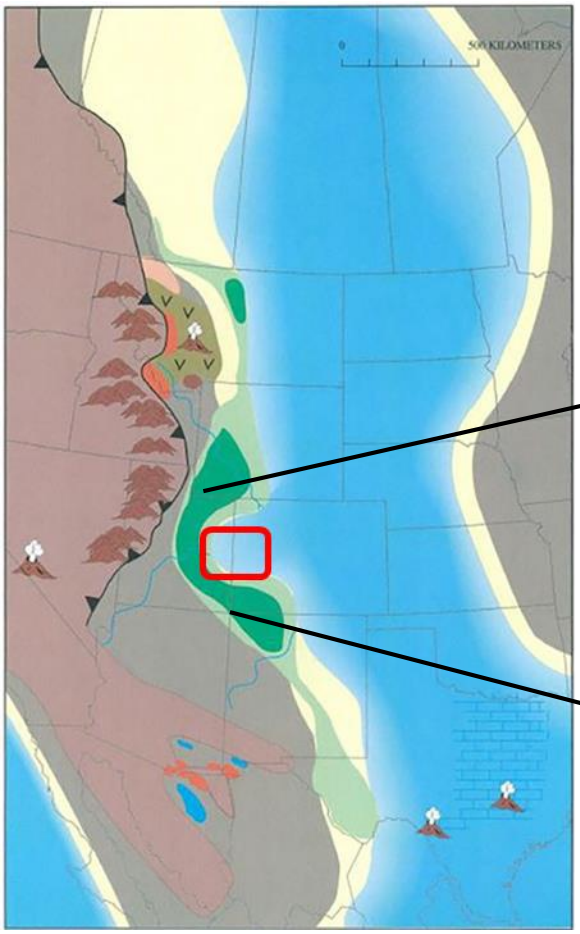

Figure 2-1: Paleogeographic map of the Western Interior Seaway during Early Campanian 83.5-79 Ma, study area in red box (from Roberts and Kirschbaum, 1995).

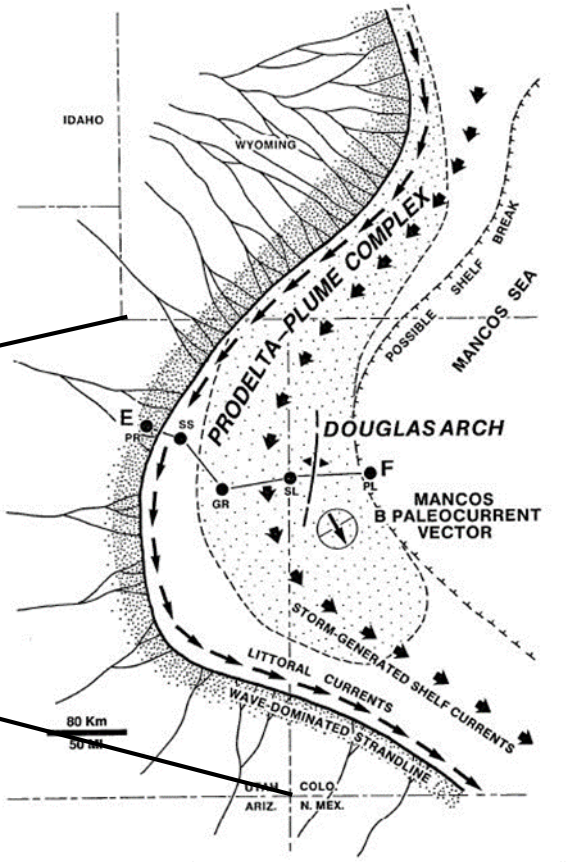

Figure 2-2: Paleogeographic map of the regional delta system. Fluvial systems sourced with sediments from the Sevier orogenic belt empty into the western shore of the Western Interior Seaway. Finer clastic particles washed out to sea formed the pro-delta deposits of the Mancos “B” Zone (from Cole and Young, 1991).

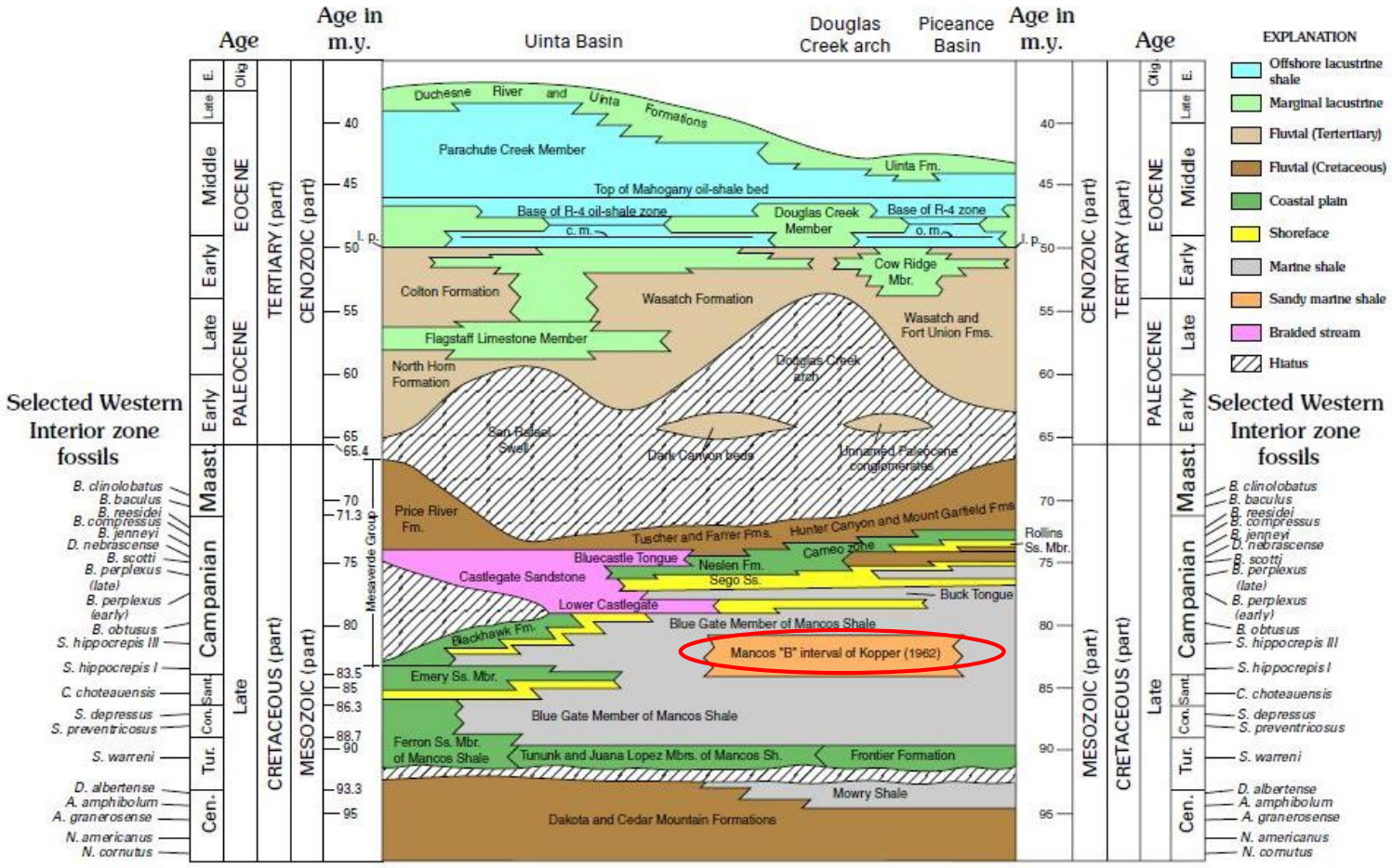

Figure 2-3: Regional stratigraphy of Uinta and Piceance Basins including Douglas Creek Arch. Mancos “B” of Kopper (1962) circled in red (from Johnson, 2003).

The Mancos “B”, as informally defined by Kellogg (1977), occupies approximately the lower 800 feet of the Prairie Canyon Member. The Prairie Canyon Member is stratigraphically located between the upper and lower Blue Gate Members of the Mancos Shale as seen in Figure 2-3 and Figure 2-4. Notice in Figure 2-4 the upward coarsening lithology.

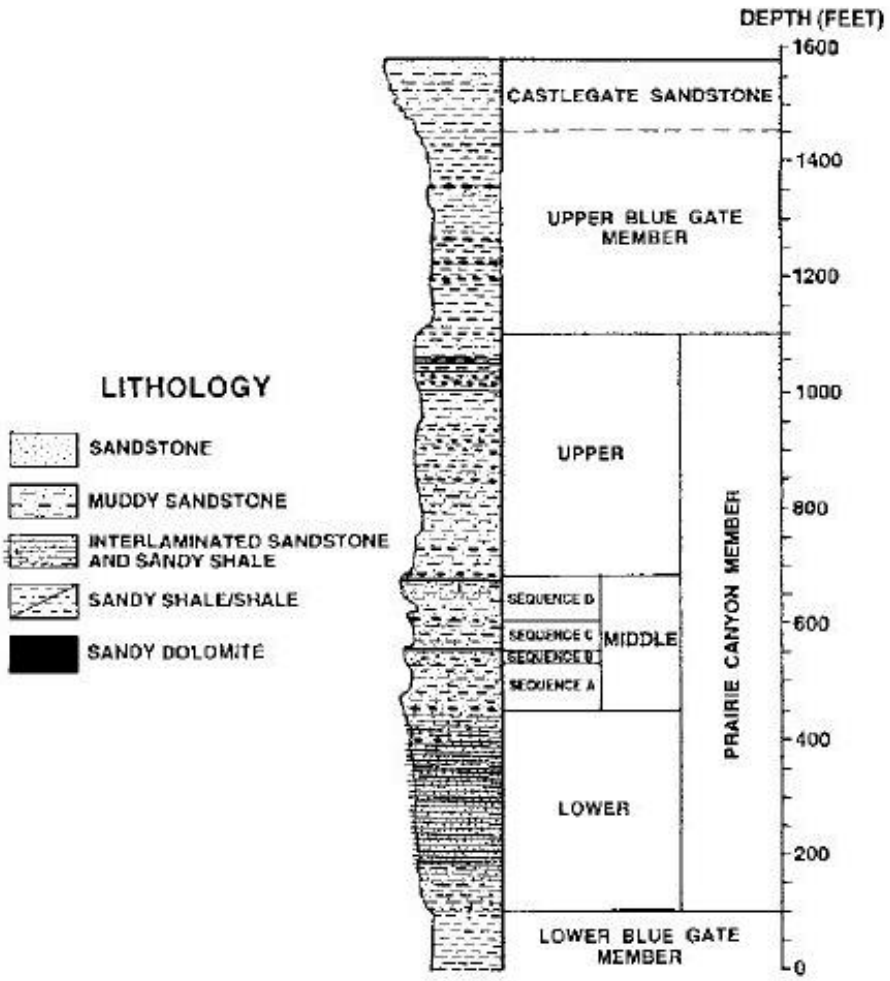

Figure 2-4: Composite type section of Prairie Canyon Member of Mancos Shale. The Blue Gate Members form part of the upper third of the Mancos Shale (from Cole and Young, 1991).

Chapter 3

Methods

3-1 Sample Procurement

All samples were obtained from the USGS Core Research Center (CRC) located at the Denver Federal Center in Denver, Colorado. Three wells were sampled. The intended objective was to select samples that would represent 3 levels of maturity: immature, early oil window, and high maturity/gas window. Initial maturity was estimated by a combination of pyrolysis and vitrinite reflectance data supplied by the CRC (see Appendix A). This information was used in sample selection to obtain samples from different wells with varying maturities of the Mancos "B".

Sample ID	Well name	Latitude	Longitude	Depth (feet)	Estimated Maturity (CRC data)
35F-2380	35-1 Federal/C-15234	39.83476	-108.693378	2380	Immature
35F-2386	35-1 Federal/C-15234	39.83476	-108.693378	2386	Immature
9F-3891	9-17-1-103 Federal	39.962477	-108.972507	3891	Early Oil
9F-3971	9-17-1-103 Federal	39.962477	-108.972507	3971	Early Oil
9F-3973	9-17-1-103 Federal	39.962477	-108.972507	3973	Early Oil
22F-6340	22-12 Federal	39.83476	-108.693378	6340	N/A
22F-12103	22-12 Federal	39.83476	-108.693378	12103	Mature/Gas
22F-12105	22-12 Federal	39.83476	-108.693378	12105	Mature/Gas

Table 3-1: Table of sample information from Mancos "B" formation.

Wells 35-1 Federal/C-15234 and 22-12 Federal had 1 inch core plugs cut from their respective core slabs. 9-17-1-103 Federal was instead a “cutting” due to the smaller size of the core available from the well. All samples (except 22F-6340) displayed a fairly high degree of lamination. Samples 35F-2380, 9F-3971 and 9F-3973 were particularly brittle along planes of lamination and fractured while being cut from the core slab as seen in Figure 3-1-4. Sample 22F-6340 is of the Mesaverde formation and while largely not discussed in this project due to its irrelevance to the Mancos “B”, results for most tests have been provided due to its usefulness to future projects.

Figure 3-1-1: Picture of core from well 35-1 Federal/C-15234 showing approximate locations of sampling (from CRC, 2017).

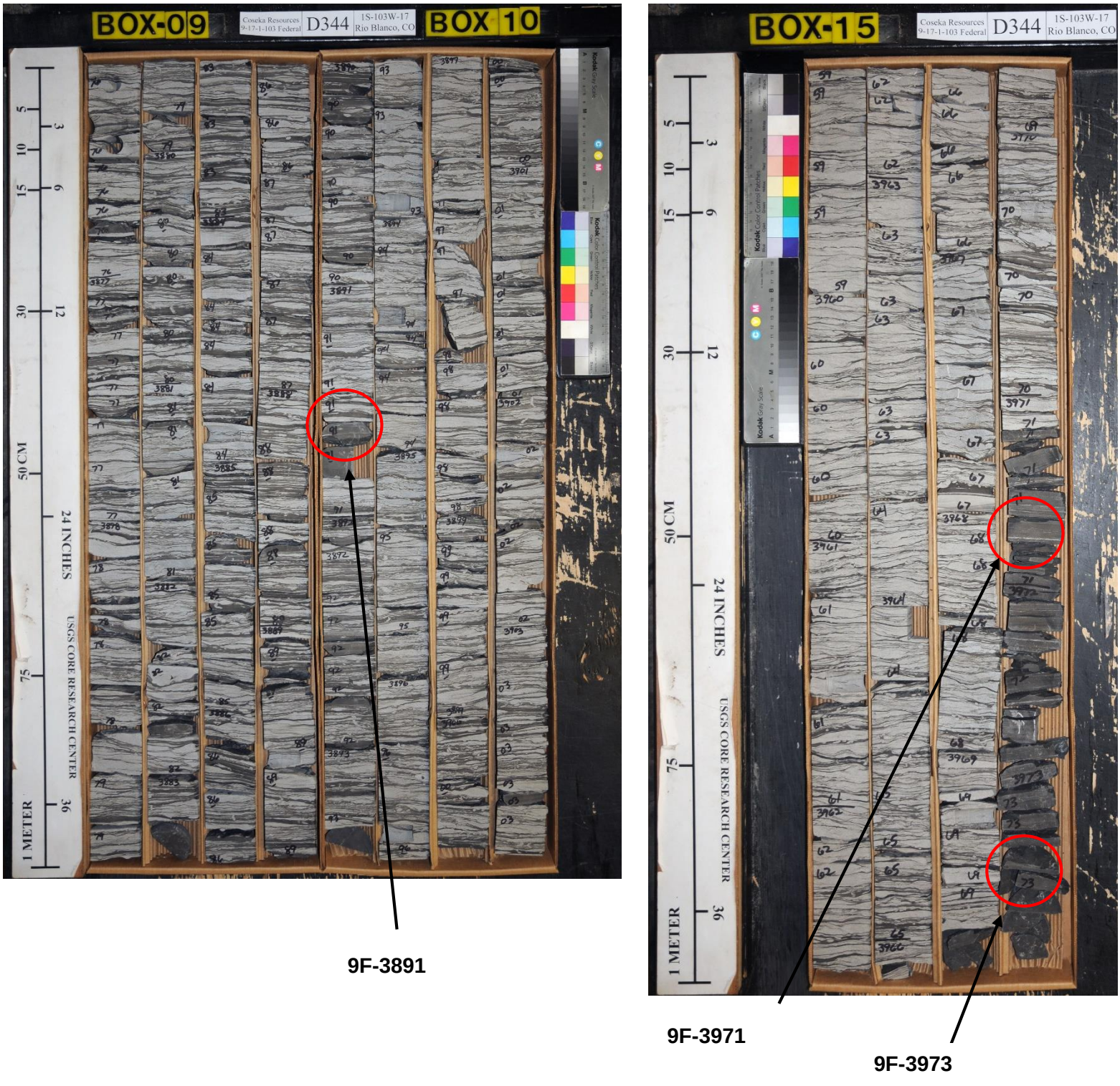

Figure 3-1-2: Picture of core from well 9-17-1-103 Federal showing approximate locations of sampling (from CRC, 2017).

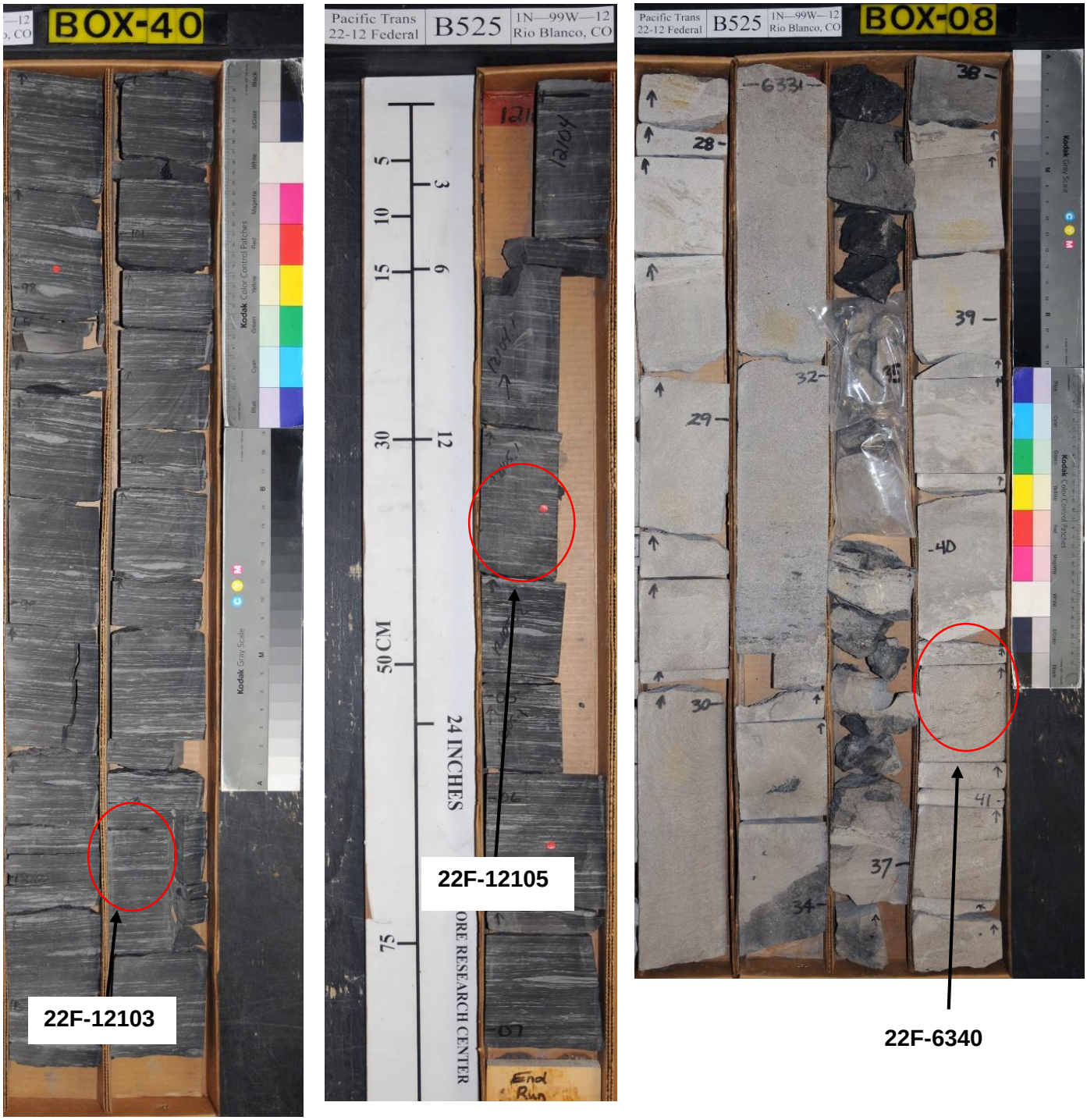

Figure: 3-1-3: Pictures of core from well 22-12 Federal showing approximate locations of sampling (from CRC, 2017).

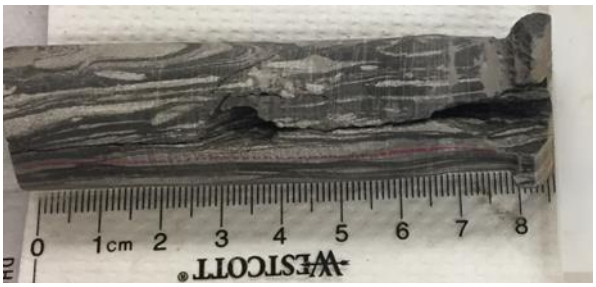

35F-2380

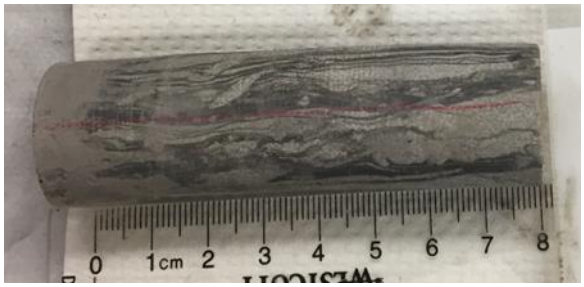

35F-2386

9F-3891

9F-3971

9F-3973

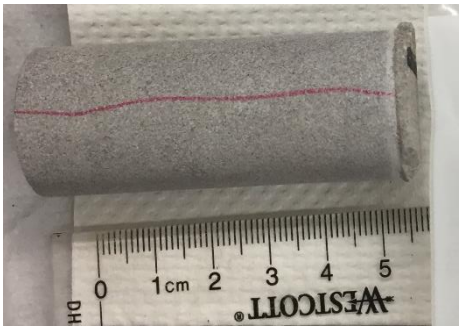

22F-6340

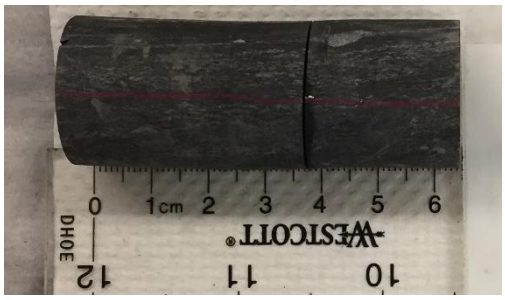

22F-12103

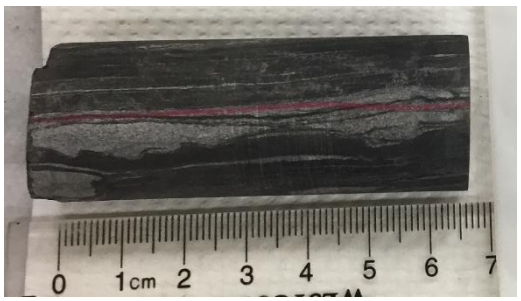

22F-12105

Figure 3-1-4: Sample photos after being cut from core slab.

3-2 Sample Preparation

Sample preparation was dependent on the intended experiments. A variety of sample types were needed for all experiments: 1-inch diameter core plug, cubes, thin slabs, GRI (Gas Research Institute) sized particles, and “powder” sized particles. In the preparation of cubes and thin slabs, a 1cm length of the core plug (or cutting for 9F samples) was sawed off and trimmed until the desired dimensions were acquired using the saw pictured in Figure 3-2-1. Cubes were generally rectangular prisms with each dimension roughly equal to 1 cm. For some of the more brittle samples cutting was difficult due to the tendency of samples to fracture along planes of lamination. The cubes of these more brittle samples were much more predisposed to have one dimension in the 0.5-0.7 cm range due to this tendency to fracture along planes of lamination. The thin slabs were generally fabricated from the trimmings that accumulated during cube production. These thin slabs were between 2-3 mm thick and roughly 1 cm^2 in the other two dimensions.

Figure 3-2-1: Saw used in dry cutting of samples.

GRI and powder sized particles were produced from sample trimmings left over from cube and thin slab processing. These trimmings were ground using a simple mortar and pestle. Two sieves allowed for GRI sized particles to be collected: those sized particles that could fit through a #20 sieve but not a #35. Powder was produced by grinding the rock sample until it fit through a #200 sieve. For the production of powder it was attempted to provide as much of the final product having come from the initial sample used. For example if 5 grams of powder was necessary this 5 grams was made form 6 grams of solid rock instead of grinding 10 grams until 5 grams where made. This was to help prevent any skewed results due to differing mineralogy and the effect that may have on its ability to be reduced in sized—e.g., more clay-rich laminations more readily breaking down thus making up a greater overall percentage than is actually present in the rock.

3-3 X-Ray Diffraction (XRD)

X-ray diffraction (XRD) allows for the mineral composition of a sample to be calculated based upon the individual “d” spacing between atoms in a mineral’s crystal lattice. The relationship described in Bragg’s law allows for the “d” spacing measurement (Bragg, 1913). All XRD testing was conducted at the Shimadzu Institute located at The University of Texas at Arlington using powder sized particles. Procedure in Appendix B.

Bragg’s Law

$$n\lambda = 2d \sin(\theta) \qquad \text{(Equation 3-3-1)}$$

λ= The wavelength of the rays

θ= The angle between the incident rays and the surface of the crystal

d= The spacing between layers of atoms

n= constructive interference when n is an integer

Figure 3-3-1: MaximaX XRD-7000: Shimadzu X-ray Diffractometer.

3-4 Total Organic Carbon (TOC)

Total organic carbon (TOC) is the carbon deposited in sediments from the remains of organisms. TOC testing was conducted at the Shimadzu Institute of The University of Texas at Arlington using a Shimadezu SSM-5000A as seen in Figure 3-4-1. For some samples the total carbon and total inorganic carbon (mainly from dolomite) was determined. TOC was then found from the difference between total carbon and total inorganic carbon. Powder sized particles are used for this testing. Procedure is in Appendix B.

Figure 3-4-1: Shimadzu SSM-5000A, TOC instrument at Shimadzu Institute.

3-5 Pyrolysis

Rock pyrolysis allows for the determination of chemical properties such as kerogen type and serves to estimate the maturity of a sample by T_{max}. A powdered sample is progressively heated to 600ºC in an inert environment. As the sample begins to increase in temperature, the hydrocarbons already present in the rock (either free or adsorbed) are volatilized. These hydrocarbons are measured and termed S_1. As temperature continues to increase, the kerogen present in the sample begins to generate hydrocarbons and hydrocarbon-like compounds. The measure of these new hydrocarbons formed by the pyrolysis of kerogen is S_2. Oxygen containing volatiles such as carbon dioxide are also released and measured as S_3. The residual carbon content of the sample after heating is termed S_4. Another important parameter gained from rock pyrolysis is T_{max} which corresponds to the maximum hydrocarbon generation during the experiment and is the peak of S_2. T_{max} is used to estimate the maturity of the sample (Tissot and Welte, 1984). All pyrolysis testing was conducted by China University of Geoscience (CUG) in Wuhan, China.

Figure 3-5-1: CUG pyrolysis machine.

3-6 Helium Porosity and Permeability

Helium Porosity was used to evaluate the porosity and permeability of 1-inch diameter, ~3-4cm long core plugs. Four samples were tested at the Chengdu University of Technology (CDUT) in Chengdu, China: 35F-2386; 22F-12105; 22F-6340; 22F-12103. Tests measured permeability parallel to laminations (horizontal permeability). With a diameter of 0.2nm helium can access some of the smallest pores, even smaller than methane can with its diameter of 0.38nm (Tissot and Welte, 1984). Using a larger sample (core plug vs. cube sample, GRI, powder) allows for factors such as fractures and laminations to play a greater role more akin to behavior at reservoir scale. Procedure is in Appendix C.

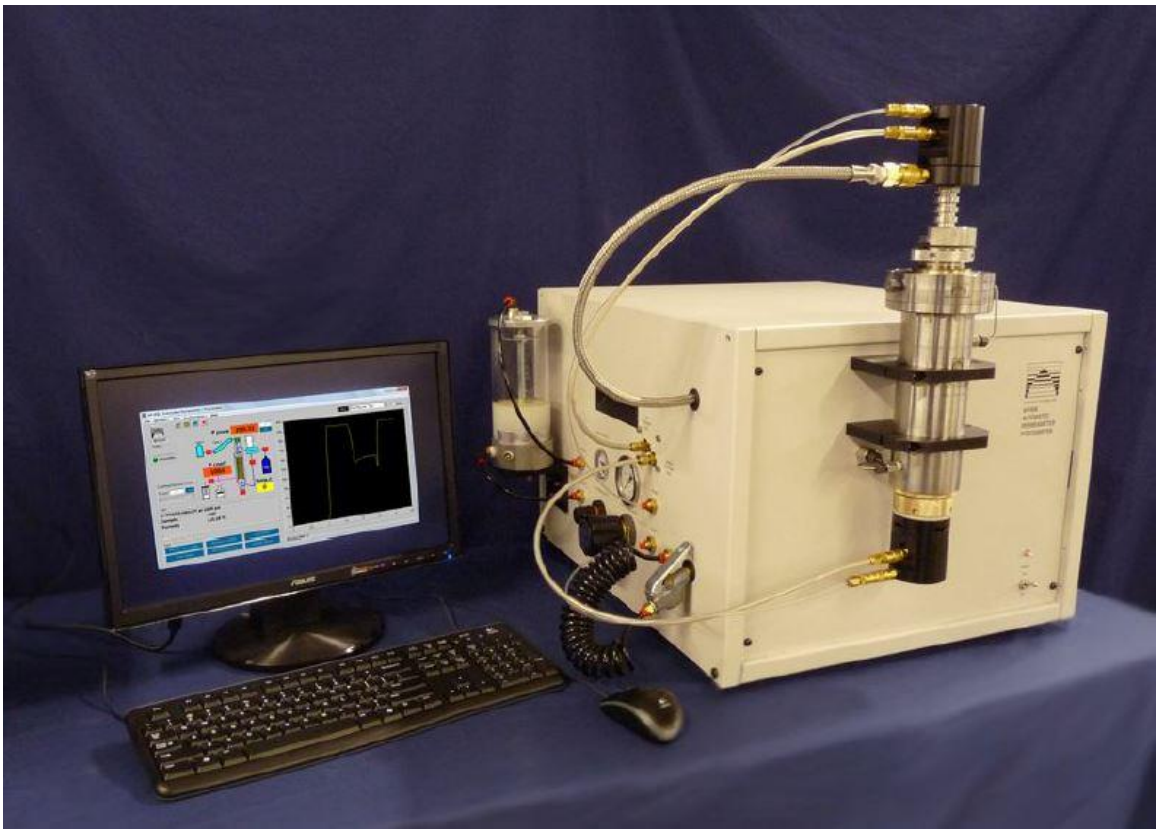

Figure 3-6-1: AP-608 Automated Permeameter-Porosimeter at CDUT used for helium porosity and permeability.

3-7 Mercury Intrusion Capillary Pressure (MICP)

MICP is used to directly measure densities, porosity, pore volume, total pore area, pore-throat size distribution, and median pore-throat size while allowing for estimates of permeability and tortuosity to be made. Using a Micromeritrics Autopore IV 9510 that utilizes pressures up to 60,000 psi, pore throats as small as 2.8nm in diameter and as large as 50µm in diameter can be measured (Gao and Hu, 2013). Mercury has a high surface energy and is non-wetting to materials naturally found in geological materials. This dictates that only external pressure is able to force mercury to invade pores once the capillary pressure is exceeded (Hu et al, 2015a). Therefore the Washburn equation (Equation 3-4-1) shows that the size of pore throats that are intruded is inversely proportional to the applied external pressure (Washburn, 1921; Gao and Hu, 2013).

Washburn Equation

$$\Delta P = -2\frac{y\cos\theta}{R} \qquad \text{(Equation 3-4-1)}$$

ΔP= External pressure applied
y= Surface tension of mercury (485 dynes)
θ= Contact angle between mercury and pore wall
R= Pore throat radius

Using the Washburn Equation 3-4-1 assumes that there is a constant surface tension and contact angle. Previous research has shown that as pore diameters decrease to the scale typically found in unconventional reservoirs the contact angle will increase exponentially while an increase in droplet radius from 1 to 10 nm leads to a 76.8% increase in surface tension (Wang et al, 2016). Therefore a modified Washburn Equation is needed that uses surface tension and contact angle as a function of pore throat radius to calculate parameters. Equation

3-4-2 describes a modified Washburn equation called the Newton-Raphson method (Wang et al, 2016). The function for R, f(R), is shown in Equation 3-4-3. A solution of zero for Equation 3-4-3 describes the pressure needed to overcome the capillary pressure of the pore.

Modified Washburn Equation

$$\Delta P = -\frac{2y_{Hg}(R)cos\theta_{Hg}(R)}{R} \qquad \text{Equation 3-4-2}$$

$$f(R) = p_c R + 2y_{Hg}(R)\cos\theta_{Hg}(R) \qquad \text{Equation 3-4-3}$$

p_c= Capillary pressure of intruded pore

By using the Modified Washburn Equation and measuring the quantity of mercury that intrudes at each pressure step, a pore-size distribution can be made. From this pore-size distribution parameters such as porosity can be determined. The Modified Washburn Equation is limited in that it assumes that all pore throats are cylindrical (later shown to not always be true in these samples) but is still a good approximation of pore-throats (Hu et al, 2015a).

Permeability can be indirectly inferred by using the Katz-Thompson Equation (1987) as described by Gao and Hu (2013) (Equation 3-4-4). This is done by determining the pore throat size at which hydraulic conductance is at a maximum. Maximum hydraulic conductance is determined by an inflection point in a graph of cumulative intrusion of mercury into the sample by pressure. A pore diameter has a specific capillary pressure that must be exceeded before mercury is intruded into the pores. An inflection point represents the pressure in which a pore network is intruded.

Katz-Thompson Equation

$$k=\left(\frac{1}{89}\right)(L_{Max})^2\left(\frac{L_{max}}{Lc}\right)\Phi S(L_{Max}) \qquad \text{Equation 3-4-4}$$

k= Permeability (μm^2)

L_{max}= Pore-throat diameter when hydraulic conductance is at a maximum (μm)

L_c= Pore-throat diameter at inflection point (μm)

$S(L_{max})$= Mercury saturation- ratio of cumulative intrusion at L_{max} to the total pore volume

To perform MICP an approximately 1 cm^3 cube is dried at 60°C for at least 48 hours to remove any moisture. The sample is allowed to cool at room temperature in a desiccator. The sample is weighed after cooling and the correct penetrometer is selected based upon sample size and porosity. The sample is sealed in the penetrometer, weighed again, and placed into the low-pressure chamber where it is evacuated to 99.993% vacuum to remove any remaining air or moisture. After evacuation, low-pressure intrusion commences and fills to a maximum pressure of 30 psi. This is used to measure the relatively large pores separately from the smaller pores that require much higher pressures. After low-pressure analysis is conducted the penetrometer is removed and weighed again to account for the mercury inside the penetrometer.

The next step is to conduct the high-pressure analysis in the high-pressure chamber. This chamber is able to utilize pressures up to 60,000 psi. Pressure is increased from 30 psi to 60,000 psi with 30 seconds off equilibrium per each pressure step. After reaching 60,000 psi, pressure is reduced and the amount of mercury extruded is measured. The sample is disposed of in a mercury safe disposal container and the raw data is extracted for processing.

3-8 Nitrogen Gas Physisorption

Low pressure nitrogen physisorption was conducted at China University of Geoscience in Wuhan, China on sample 35F-2380 using GRI sized particles. Nitrogen physisorption allows us to determine a sample's sorption-desorption isotherm as described by Sing (1985). When nitrogen gas is exposed to a surface at 77Kº in liquid phase, a specific number of gas molecules will adsorb on to the surface by van der Waals forces. This process is termed physical adsorption or physisorption. By using this process, the pore geometry can be inferred by isotherms formed by adsorption and desorption (Bertier et al, 2016). Procedure is in Appendix D.

Figure 3-8-1: An Autosorb iQ/ASiQwin at CUG.

3-9 Field Emission-Scanning Electron Microscopy

Field Emission-Scanning Electron Microscopy (FE-SEM) images, after argon ion milling, were conducted for two samples: 9F-3971 and 22F-12103 using thin slabs. These images allow us to see details on the scale of a few nanometers. FE-SEM imaging was conducted using a Zeiss Merlin Compact (Fig.3-9-1) at the Institute of Geology and Geophysics, Chinese Academy of Science (ACS-IGG), Beijing, China.

FE-SEM works by liberating electrons from a field emission source and accelerating those electrons in a high electrical field gradient. Primary electrons are focused and deflected by electronic lenses to produce a narrow scan beam that bombards the object. This produces secondary electrons that are emitted from the object being analyzed. The surface structure of the object is determined by the angle and velocity of the emitted secondary electrons. These electrons produce a weak signal that is then amplified and processed into an image. FE-SEM differs from other SEM methods in that it uses a “cold” source for electrons as opposed to the 2800^{o}C tungsten filament used in conventional SEM methods.

Figure 3-9-1: Zeiss Merlin Compact.

3-10 Contact Angle for Wettability

A sample's wettability is determined based upon a fluid's interaction with the rock. A rock's predisposition to behaving in a hydrophobic or hydrophilic manner is the prominent controlling factor on the contact angle measured. This experiment utilizes the thin slab sample type and two fluids, API brine and n-decane. API (American Petroleum Institute) brine is a solution of deionized water with sodium and calcium salts dissolved that is meant to emulate saline formation fluids. N-decane is used to emulate oil. A pipette will drop approximately 2 uL of each fluid on a thin slab of the sample allowing the wettability (through contact angle between fluid and surface) of each to be observed. A sample that exhibits good wetting for a particular fluid will allow for the fluid to spread out on the sample's surface producing a low contact angle. A poorly wetting surface will resist this spreading and maintain a much smaller area of fluid to surface contact resulting in a large contact angle. A SL200KB Optical Contact Angle Meter (Figure 3-10-1) was used with testing done at CUG.

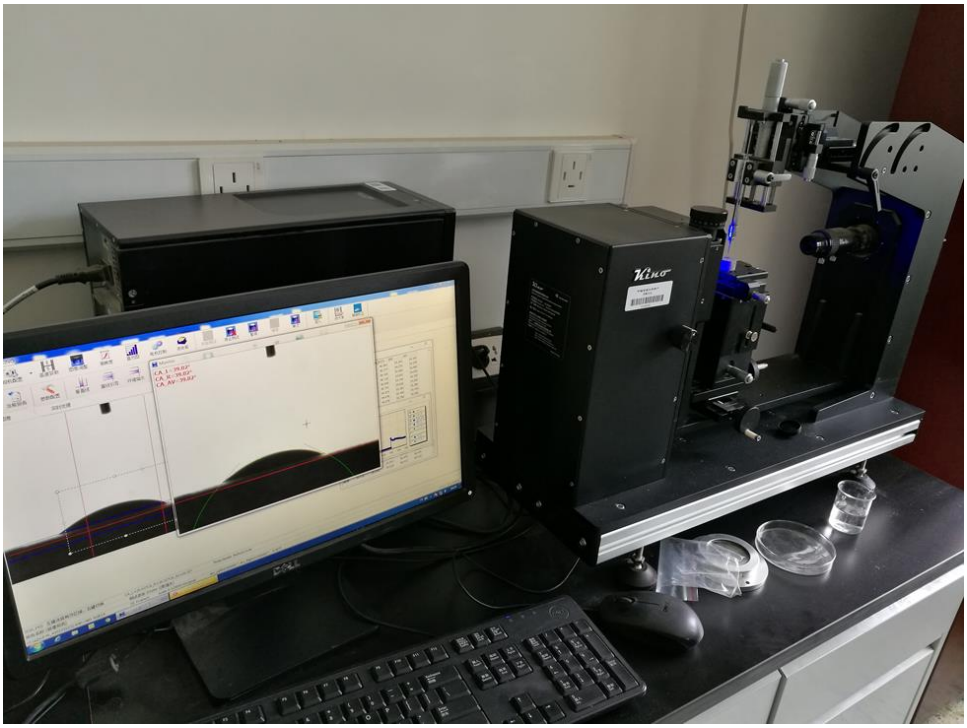

Figure 3-10-1: SL200KB Optical Contact Angle Meter.

3-11 Spontaneous Fluid Imbibition

Imbibition tests are used to determine pore connectivity. It is a process driven by capillary pressure that involves a non-wetting fluid displacing a wetting fluid (Gao and Hu, 2012). The test involves exposing one side of a cube shaped sample to a fluid and measuring the fluid uptake over time. The cube used has had the four faces of the cube's perimeter epoxied to insure that fluid only imbibes from the face exposed to the fluid. The top and bottom of the sample is left exposed. Cubes are epoxied in a way to allow fluid to be imbibed parallel to bedding/laminations. A weighting apparatus that combines a chamber where the sample is suspended and a scale is used to measure the cumulative imbibition of fluid. In the chamber the sample is suspended above a petri dish of the selected fluid. Initially, the sample will be dried at a temperature of 60ºC for at least two days to remove any accessible water and weighted. For samples that were tested using DI water, tests were run for ~24 hours. N-decane tests lasted ~8 hours though 22F-12103/12105 ran for 20-24 hours. Afterward the test samples are weighed to compare to recorded results for sample gain. Differences between the recorded weight gain from the scale during the experiment and the before and after weights recorded separately can be attributed to a "pull-down" effect. This "pull-down" effect, described by Hu et al (2001), is the result of a reduction in the buoyant forces acting on the sample. This is due to the slight decrease in water level in the petri dish's finite reservoir. As the fluid level falls but the sample's position remains constant buoyant forces helping to suspend the cube decrease causing a false high reading of imbibed fluid. The error caused by this is proportional to the ratio of sample to reservoir cross-sectional area (Hu et al., 2001)

The capillary pressure that drives imbibition is affected by the wettability of the sample while porosity and pore connectivity are controls on the permeability of the sample. This is significant in that imbibition is controlled by capillary pressure and permeability (Hu et al, 2001).

Equation 3-11-1 from Philip (1957) describes the relationship between cumulative fluid imbibition, sorptivity and time.

Cumulative uptake of water by imbibition

$$I(t)=St^{0.5}+At \qquad \text{Equation 3-11-1}$$

I(t)= Cumulative imbibition (mm)

S= Sorptivity (mm/√sec)

t= Time (sec)

A= Empirically determined constant

Philip (1957) states that the term “At” from Equation 3-11-1 is negligible when the gravity potential gradients are small relative to matric potential gradients. This condition is met in testing for this project so the “At” term can be ignored.

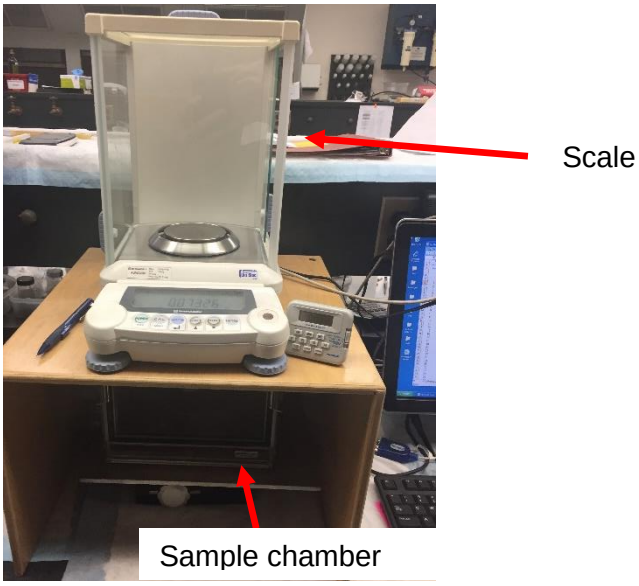

Figure 3-11-1: Imbibition apparatus used for imbibition experiments.

Chapter 4

Results

4-1 X-Ray Diffraction (XRD)

X-ray diffraction allows for mineralogy to be determined by a mineral's "d" spacing within a crystal's lattice. Tables 4-1-1 and 4-1-2 compile the results from the Shimadzu Institute. Results generally conclude with lithology descriptions from sources such as Cole and Young (1991) among others particulary the relatively low concentrations of carbonates (typically dolomite). Figure 4-1-1 is a Schlumberger ternary diagram that catagorizes the samples based upon their measurement of QFM (quartz, feldspar, mica), clays and carbonates. Most samples fall within the mixed silicous mudstone grouping. Samples are relatively rich in quartz with many samples having approximately 50% making up its minerology. Samples are relatively low in carbonates. This is in agreement with other research (Cole et al, 1997; Hampton, 1999; Cole and Young, 1991; Kellogg, 1977) that proposed the Mancos "B" to be mainly clastic sediments erodoed off of uplifts created by the Sever Orogeny.

Sample ID	QFM	Clays	Carbonates
35F-2380	69.77	8.58	21.65
35F-2386	54.60	26.37	19.03
9F-3891	73.27	2.24	24.49
9F-3971	54.52	26.08	19.40
9F-3973	44.29	44.80	10.92
22F-6340	94.30	5.70	0.00
22F-12103	64.01	21.79	14.20
22F-12105	53.38	31.18	15.44

Table 4-1-1: X-ray diffraction results (%) from Shimadzu Institute.

35F-2380	Wt%
Albite	6
Calcite	5.3
Clinoenstatite	4.5
Clintonite-1M	3.5
Dolomite	15.9
Fraipontite-1O	0.5
Illite-2M1	3.2
Kaolinite-1A	1.2
Microcline, intermediate	3.7
Pyrite	2.2
Quartz	54.1

35F-2386	Wt%
Calcite	3.5
Dolomite	14.9
Illite-2M1	1.1
Illite-2M2	24.4
Microcline, intermediate	8.9
Oligoclase	1.1
Pyrite	3.3
Quartz	42.8

9F-3891	Wt%
Albite	2.5
Calcite	3.9
Dolomite	20.1
Donpeacorite	4.4
Illite-2M1	2.2
Microcline, intermediate	3.3
Pyrite	2
Quartz	61.6

9F-3971	Wt%
Albite	8.3
Calcite	2.9
Dolomite	16
Glauconite	6.7
Grossite	5.2
Illite-1M	16.2
Kaolinite-1A	2.5
Microcline, intermediate	3.1
Pyrite	2.5
Quartz	36.5

9F-3973	Wt%
Calcite	3.2
Dolomite	7.5
Fraipontite-1O	4
Illite-2M2	39
Kaolinite-1A	0.9
Microcline, intermediate	8.4
Pyrite	2
Quartz	35

22F-6340	Wt%
Halloysite-14A	2.7
Illite-2M1	0.9
Kaolinite-1A	2.2
Quartz	94.3

22F-12103	Wt%
Akermanite	2
Albite	11.6
Dolomite	12.8
Fraipontite-1O	6
Glauconite	11.6
Magnesiochloritoid	5.1
Pyrite	1
Quartz	50

22F-12105	Wt%
Albite	7.9
Ankerite	13
Dolomite	2.3
Fraipontite-1O	5.3
Illite-1M	25.6
Pyrite	0.9
Quartz	45

Tables 4-5-2: Detailed XRD analysis results.

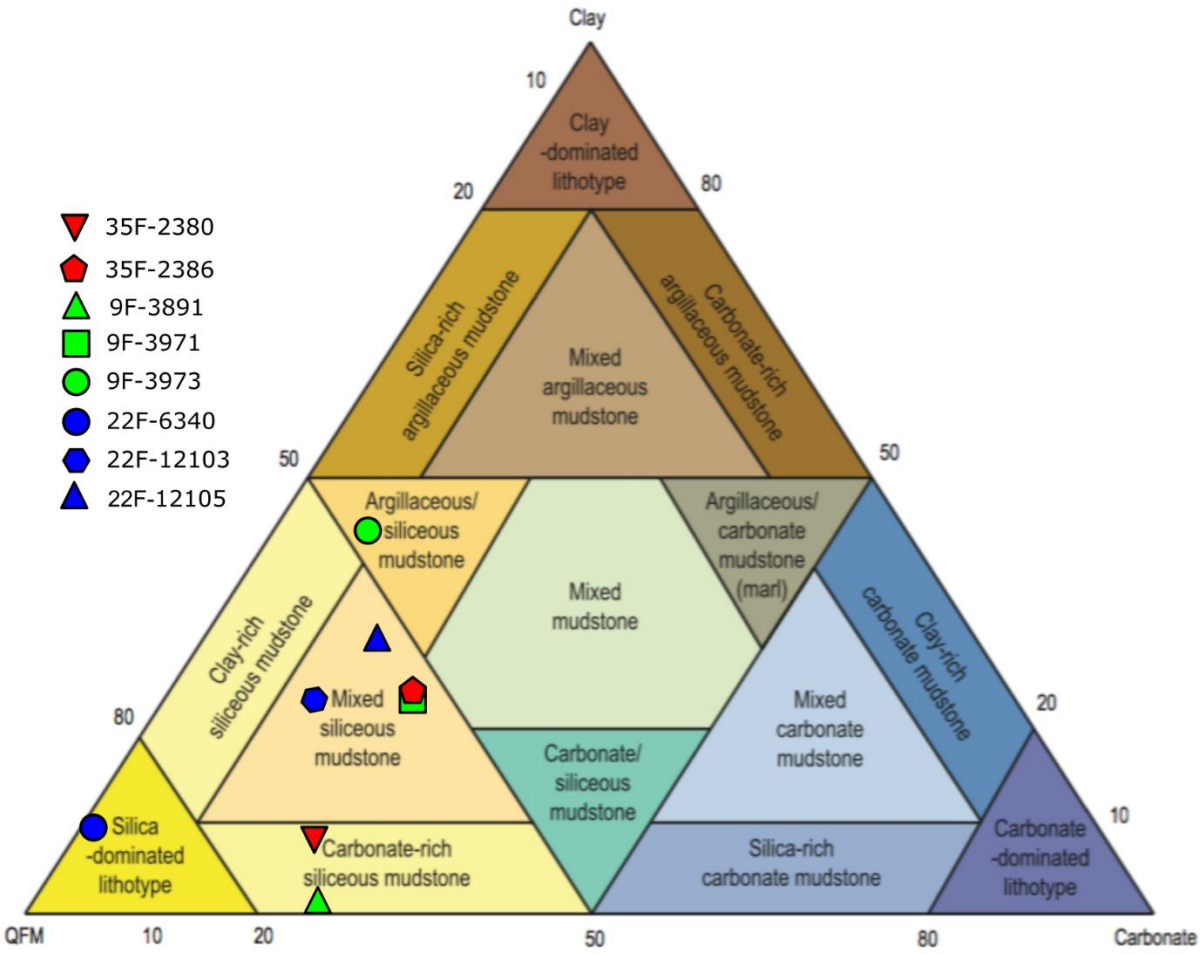

Figure 4-1-1: Schlumberger ternary diagram of mineralogy from X-ray diffraction analysis.

4-2 Total Organic Carbon (TOC)

Total organic carbon (TOC) as measured by the Shimadzu Institute using a Shimadzu SSM-5000A. Table 4-2-1 compiles the TOC results. TOC values range from 0.671% to 1.854% (excluding sample 22F-6340).

Sample	TC (%)	IC (%)	TOC (%)
35F-2380	7.654	6.983	0.671
35F-2386			0.777
9F-3891			0.675
9F-3971	3.745	1.891	1.854
9F-3973	3.173	1.897	1.276
22F- 6340	2.847	0.1002	2.747
22F-12103			1.148
22F-12105	2.998	1.699	1.299

Table 4-2-1: Compilation of TOC results from Shimadzu Institute.

4-3 Pyrolysis

Pyrolysis data is compiled in Table 4-3-1 for all 8 samples. From this pyrolysis data maturity and kerogen type can be estimated. Figure 4-3-1 is Weatherford Laboratories' graph for determining kerogen type from hydrogen index (HI) vs T-max. The HI is calculated by:

$$HI = (S_2/TOC) \times 100$$ (Tissot & Welte, 1984)

Results from the HI/T-max plot of Figure 4-3-1 show that most samples fall within the type III gas prone category. Samples 22F-12103 and 22F-12105 both fall into the type IV range. This is significant in that these samples lack the hydrogen necessary to be hydrocarbon producing. As is later addressed in the discussion of this paper, kerogen type has a significant impact on how much of the TOC in a sample is able to generate hydrocarbons during maturation (Jarvie, 2014).

Sample ID	S1 mg HC/g	S2 mg HC/g	S4 mg C/g	T_{max}	HI S_2x100/TOC
35F2380	0.23	0.67	8.18	434	75
35F2386	0.3	0.63	6.61	426	85
9F3891	0.15	0.45	5.96	424	69
9F3971	0.35	1.33	10.81	429	109
9F3973	0.5	1.56	11.51	429	118
22F6340	0.05	0.08	0.07	429	400
22F12103	0.27	0.37	10.82	462	32
22F12105	0.24	0.55	15.51	469	34

Table 4-3-1: Pyrolysis data from CUG.

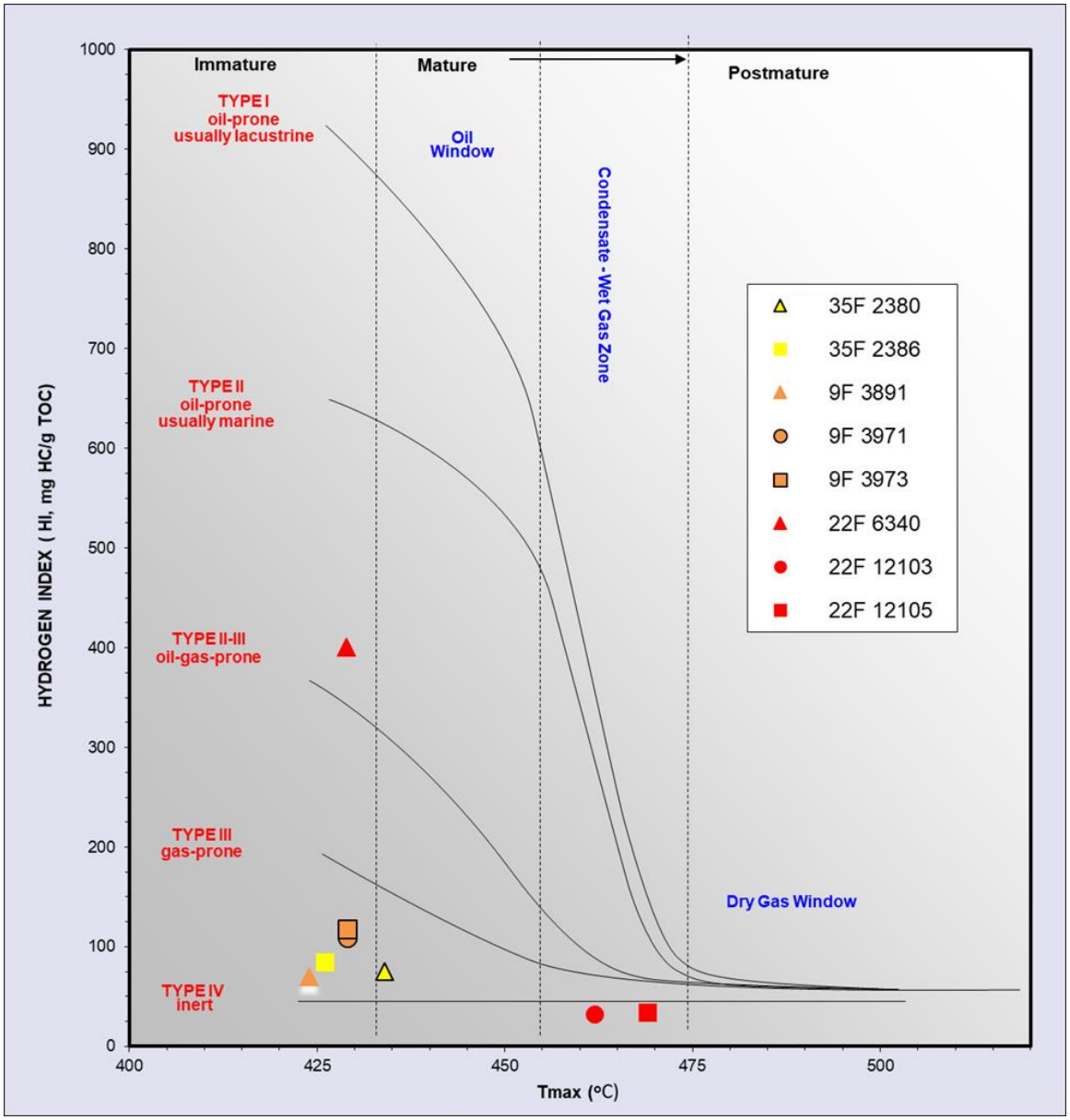

Figure 4-3-1: Weatherford Laboratories kerogen type determination by HI index versus T-max.

4-4 Helium Porosity and Permeability

Helium analysis allows for porosity and permeability measurements at a larger scale than other tests such as MICP that use 1-cm^3 sized cubes. This presents some interesting results when compared to other tests. While typically the larger the sample size, the smaller resulting permeability; the opposite trend is apparent from these samples when compared to MICP results for permeability. Also the porosity from the helium experiments is roughly twice as high for some samples when compared to MICP (see Figure 4-4-1). While the diameter of helium is an order of magnitude smaller at 0.2nm compared to the minimum pore-throat size of ~2.8 nm MICP can measure, the extra pores the helium is able to invade is unlikely to be the source in the disparity between MICP and helium porosity results. More importantly though, the larger the sample size, the greater the proportion of isolated pores there are not accessible to either helium or mercury. Instead the increased porosity and permeability is likely due to fractures and/or high porosity/permeability zones, a product of being highly laminated.

Another important contribution for the discrepancy between MICP and helium testing is the effect of anisotropic permeability on a sample. Laminated mudstones of silt and clay like those samples obtained for this work (see Figure 3-1-4) are likely to have horizontal to vertical permeability ratios over 10^3 (Aplin and Moore, 2016). This is significant in that MICP tests take an omnidirectional approach while helium tests are unidirectional. In this project the plugs were cut so that the helium would travel parallel to bedding. Permeability tests that measure parallel to bedding in highly laminated rocks will yield much higher permeability than methods that take into account permeability in all directions. This difference helps account for the disparity between helium porosity/permeability measurements and MICP.

Sample ID	Particle density (g/cm^3)	Porosity (%)	Permeability (µD)	Permeability-Klinkinberg (µD)
35F 2386	2.387	10.89	22,270	21,106
22F 6340	2.47	6.821	6	3
22F 12103	2.56	3.653	1	0
22F 12105	2.59	6.17	90	65

Table 4-4-1: Results of helium porosity and permeability from CDUT.

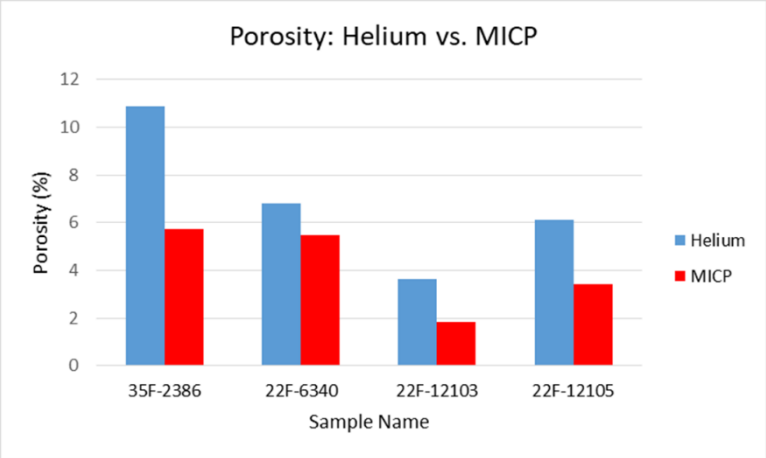

Figure 4-4-1: Comparison of helium porosity to MICP porosity.

4-5 Mercury Intrusion Capillary Pressure (MICP)

Mercury Intrusion Capillary Pressure (MICP) is one of the key tests in this project due to the wealth of information it is able to provide. Table 4-5-1 details some of the more significant parameters such as permeability, porosity and median pore-throat diameter. Figures 4-5-2 through 4-5-4 show the pore-size distribution of all samples from the 3 wells as pie charts. This helps to visualize the dominant pore systems for each sample. Figures 4-5-5 and 4-5-6 help to visualize the pore-size distribution comparing the samples to one another. Figure 4-5-5 is especially helpful to outline which pore-size intervals are most prominent among the samples

while 4-5-6 is essentially the same information as the pie charts but in a format that allows easy comparison between samples.

Both samples 35F-2386 and 9F-3891 have little to no mercury intrusion in pores smaller than 10 nm (see Figure 4-5-1 for example). Since the smallest of pores are absent this skews the harmonic mean for permeability and is the reason for both samples having permeability 3-4 orders of magnitude greater than the other samples. As discussed in more detail later, 35F-2386 likely lacks pores less than 50nm due to low maturity while 9F-3891 likely lacks pores less than 10nm due to low clay content.

Pore-size distribution of samples fall into either two categories: type A and type B. Type A pore-size distribution consists of a major peak between 500nm-800nm and a minor peak between 10nm-50nm. Type B pore-size distribution entails a single peak at approximately 10nm-50nm. This is discussed in more detail in the discussion, Section 5-2.

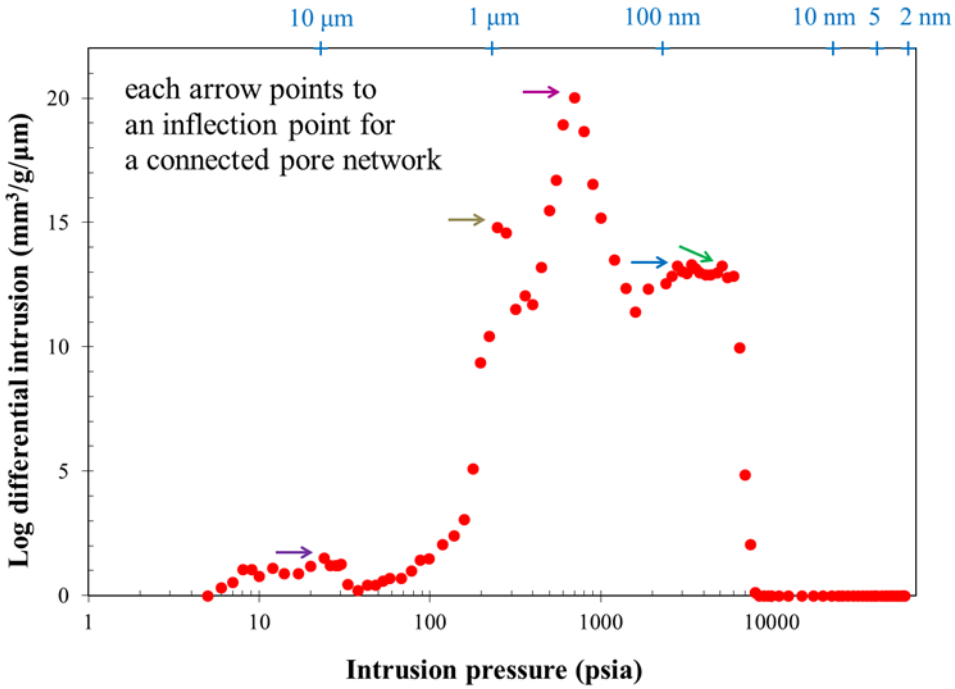

Figure 4-5-1: MICP pore-size distribution for sample 35F-2386. Note the lack of mercury intrusion in pores less than ~50nm.

	35F 2380	35F 2386	9F 3891	9F 3971	9F 3973	22F 6340	22F 12103	22F 12105
Bulk Density (g/cm^3)	2.648	2.4378	2.4721	2.5426	2.4963	2.482	2.604	2.5719
Total Pore Volume (cm^3/g)	0.0279	0.0236	0.0286	0.0155	0.017	0.022	0.0070	0.0133
Total Pore Area (m^2/g)	4.734	0.837	1.654	8.143	8.893	2.478	3.186	5.82
Median Throat Diameter (Area, nm)	8.4	53.8	21.8	6.0	6.0	17.9	6.1	6.9
Median Throat Diameter (4V/A, nm)	23.6	112.7	69.1	7.6	7.6	35.6	8.9	9.2
Porosity (%)	6.98	5.75	6.03	3.94	4.23	5.47	1.831	3.426
Harmonic Mean for k (nD)	56.2	11,158	24,858	99	12.3	69	55.4	6.63
Geometric Mean for k (nD)	2600	22,700	121,000	13	26	461	384	26
Geometric Mean 1st 3 inflection points	x	28,000	x	x	x	1,000	1,000	9,000

Table 4-5-1: Compilation of MICP results.

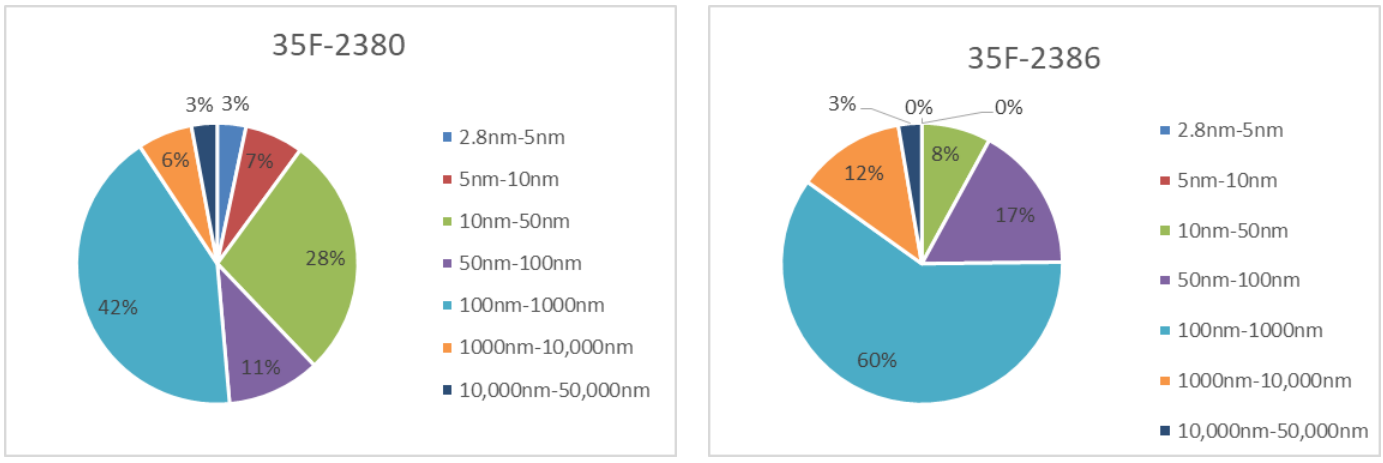

Figure 4-5-2: Pore-throat size distribution of samples from well 35-1 Federal/C-15234.

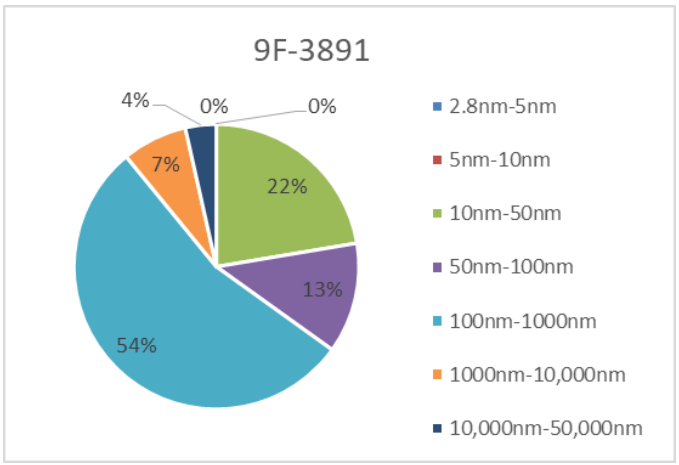

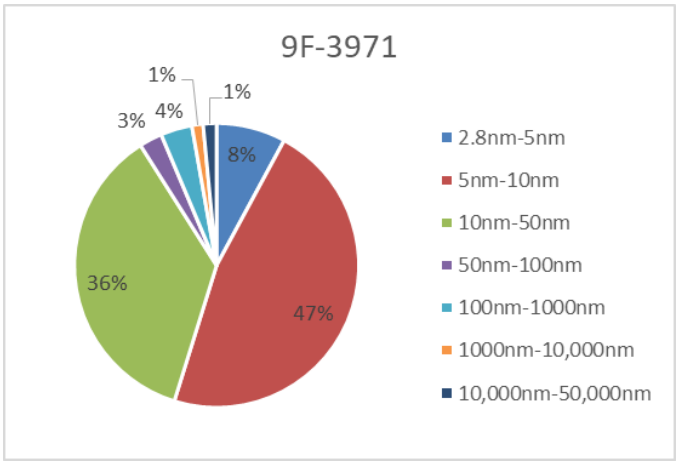

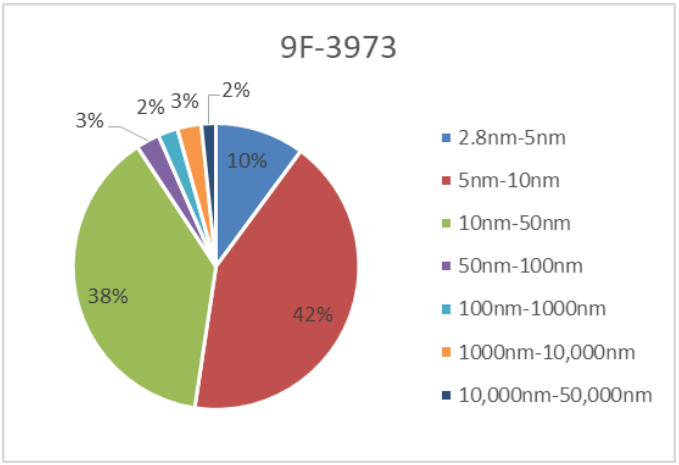

Figure 4-5-3: Pore-size distribution of samples from well 9-17-1-103 Federal.

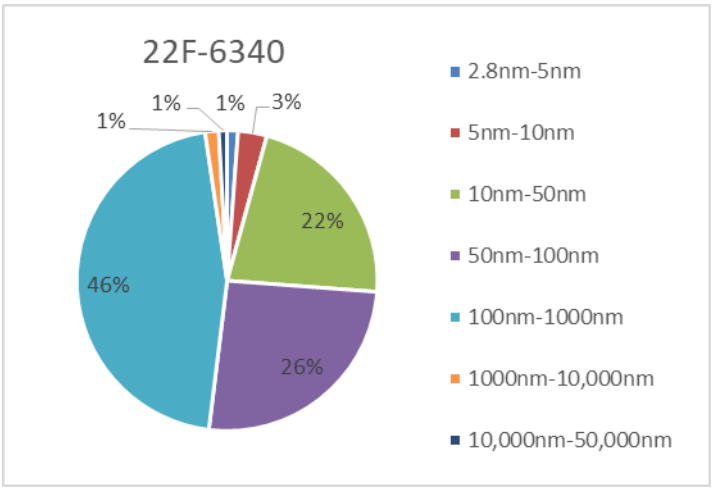

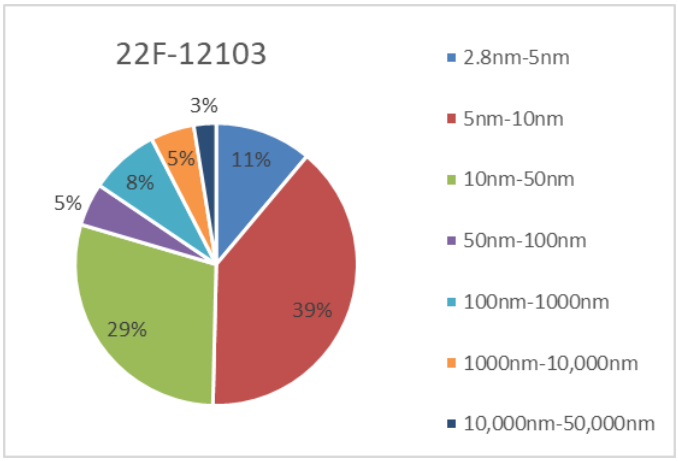

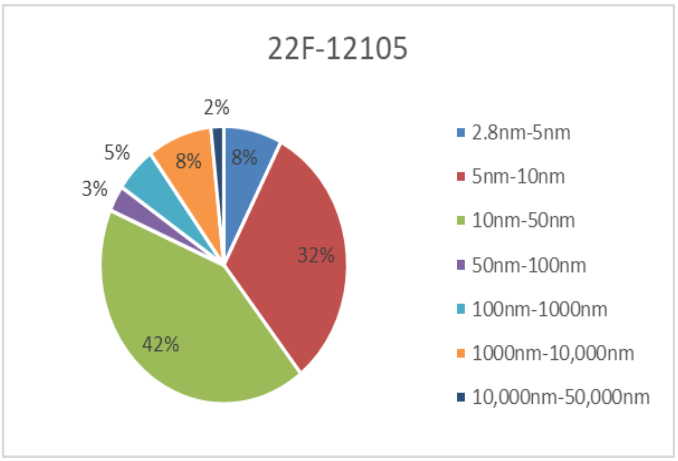

Figure 4-5-4: Pore-size distribution of samples from well 22-12 Federal.

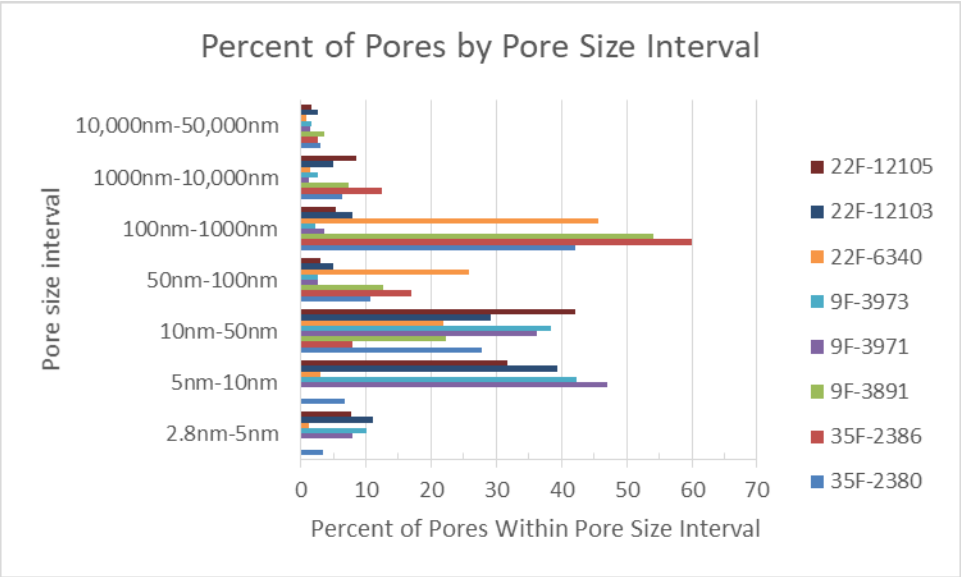

Figure 4-5-6: Graphical representation of pore-size interval's occurrence by percentage of a given sample.

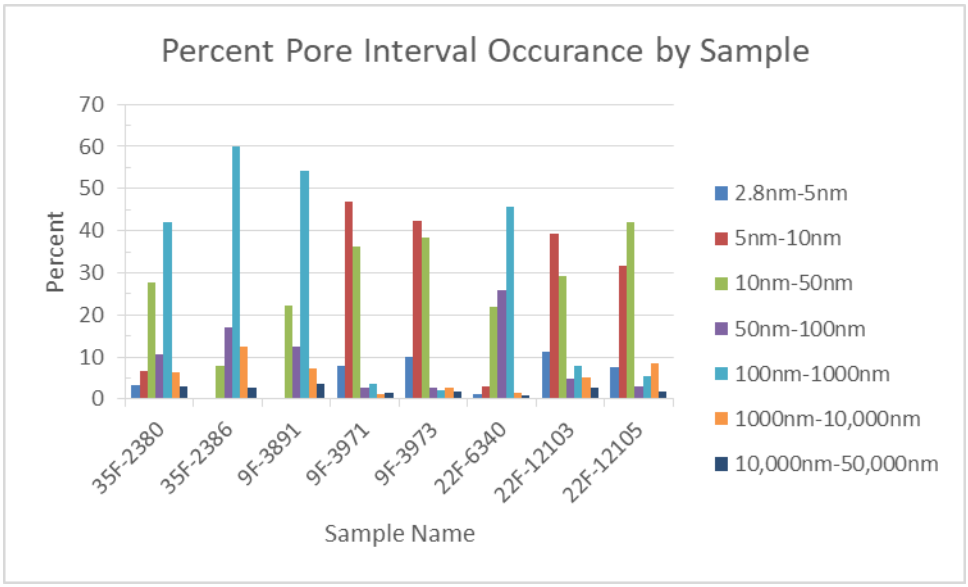

Figure 4-5-5: Graphical representation of how common (by percentage) pore-throat sizes are in a given interval.

4-6 Nitrogen Gas Physisorption

One sample, 35F-2380, was tested using nitrogen physisorption. By graphing the adsorption and desorption of liquid nitrogen at 77ºK observations about the particles that make up the sample and pore geometry can be determined. A graph of volume adsorbed verses relative pressure (the ratio of absolute gas pressure to saturation pressure) as described in Sing (1985) allows an isotherm to be made. From Figure 4-6-1 a Type 3 hysteresis loop is observed. Sing (1985) describes this isotherm type as being made by plate-like particles that produce slit-shaped pores. In the context of these samples this likely suggests clay platelets are a significant influence on the pore geometry. Additional observations such as FE-SEM imaging in Section 4-7 furthers this inference.

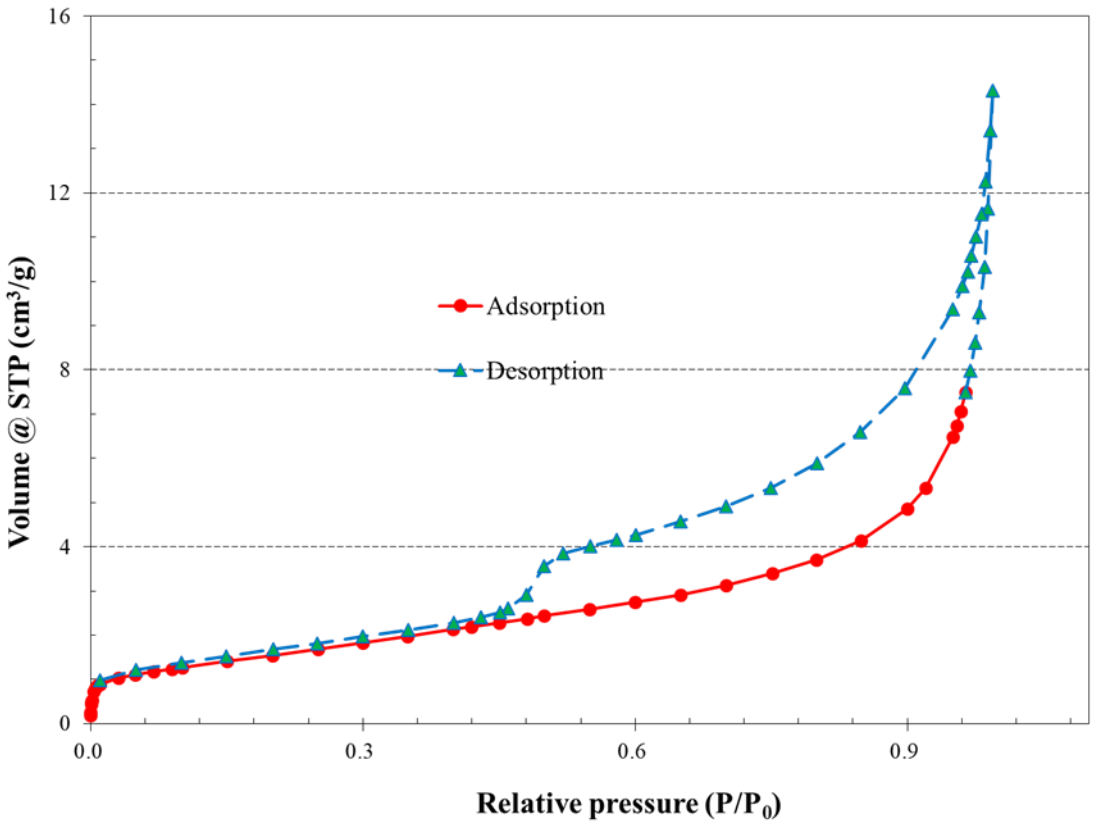

Figure 4-6-1: Isotherm of 35F-2380.

4-7 FE-SEM

Field emission-scanning electron microscope (FE-SEM) images were taken for two samples: 9F-3971 and 22F-12103. Figure 4-7-1 allows for the visualization of the inter-particle porosity from sample 9F-3971. While different samples, FE-SEM images show slit-shaped pores as suggested in nitrogen gas physisorption. Figure 4-7-2 details organic matter-hosted pores. Organic pores are typically much smaller than inter-particle pores and form during the maturation of organic material. These pores are the pores hosted within the dark patches of materials (organic matter). While a magnitude of order smaller in size, the organic pores from FE-SEM imaging appear to have a less overall elongation of pore geometry. Curtis (2012) found similar results, slit-like pores in the matrix and more round-shaped pores hosted within organic matter.

Figures 4-7-3 and 4-7-4 are images from sample 22F-12103 and display many similar characteristics to 9F-3971. The similarities include the numerous slit-shaped pores as seen in Figure 4-7-3 and the more rounded organic hosted pores outlined in figure 4-7-4 like in Figure 4-7-2. Figure 4-7-4 also has an interesting accumulation of bright cubic shaped pyrite surrounded by organic matter. Figure 4-7-5 is of relatively lower magnification that allows for the imaging of micro-fractures and pockets of µm sized organic matter.

Many elongated slit-like pores, with large length to width ratios.

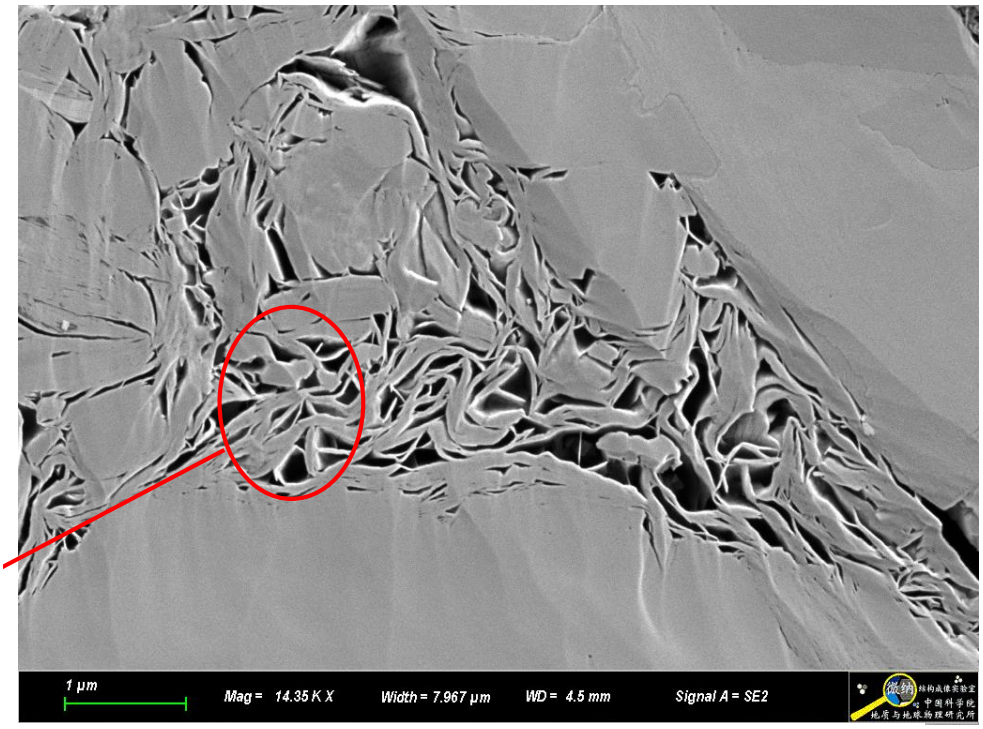

Figure 4-7-1: SEM image details slit-shaped inter-particle pores in clay rich matrix from thin slabs of sample 9F-3971.

Pores hosted within organic matter with more rounded geometry.

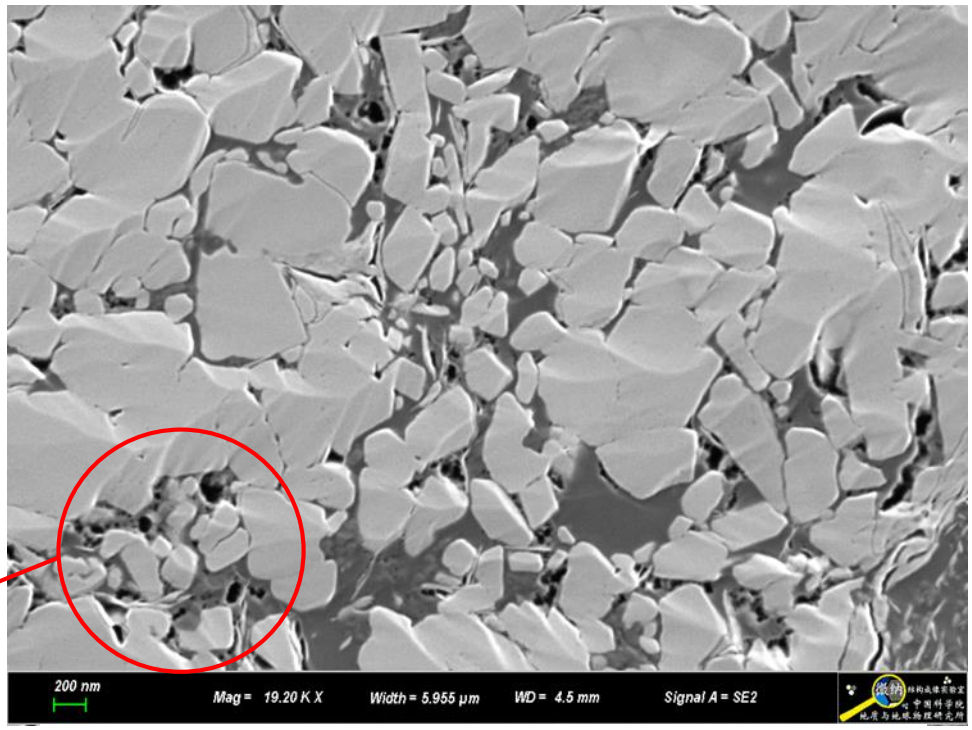

Figure 4-7-2: SEM image of sample 9F-3971 details slit shaped inter-particle pores and organic matter hosted pores with smaller length to width ratios (more rounded).

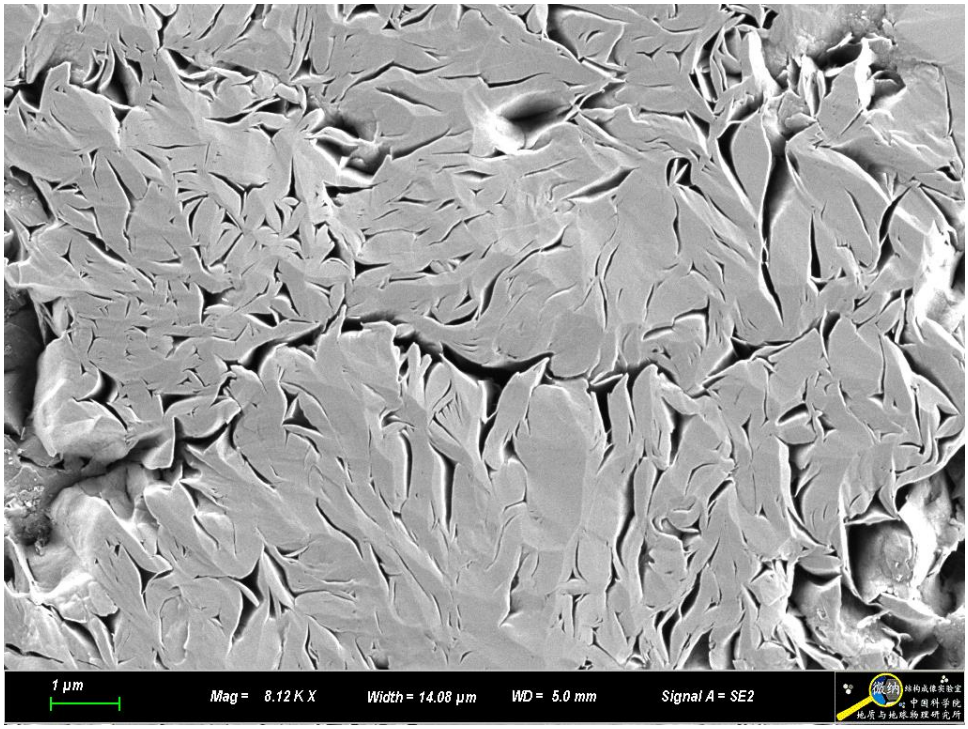

Figure 4-7-3: SEM image details slit shaped inter-particle pores from thin slabs of sample 22F-12103.

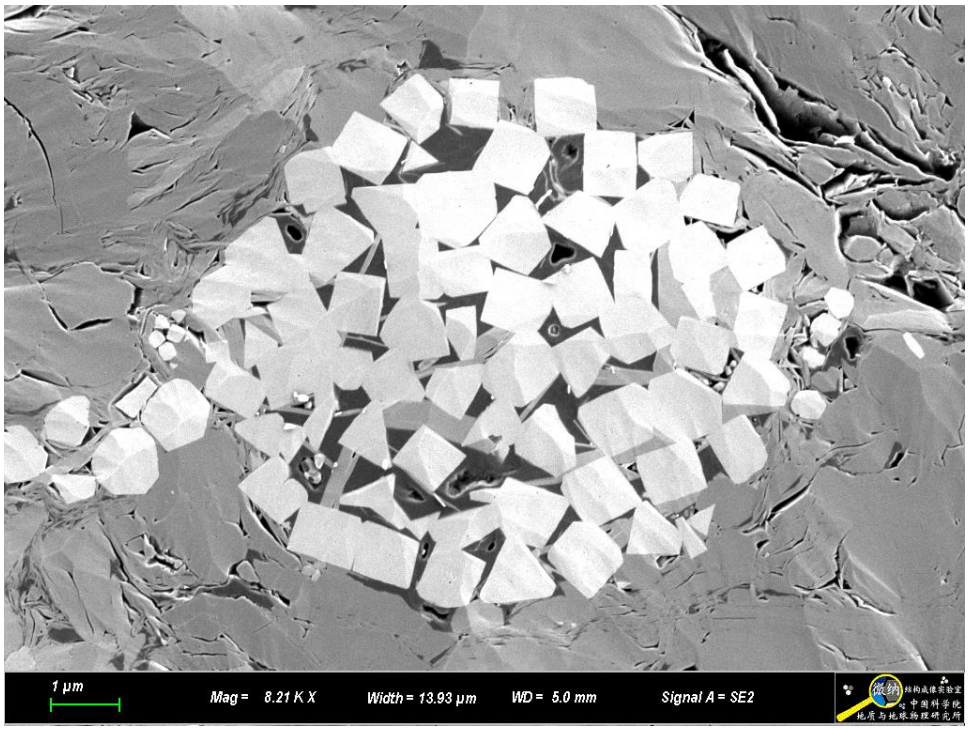

Figure 4-7-4: SEM image details slit shaped inter-particle pores from thin slabs of sample 22F-12103, bright white cube shapes are pyrite crystals surround by organic matter.

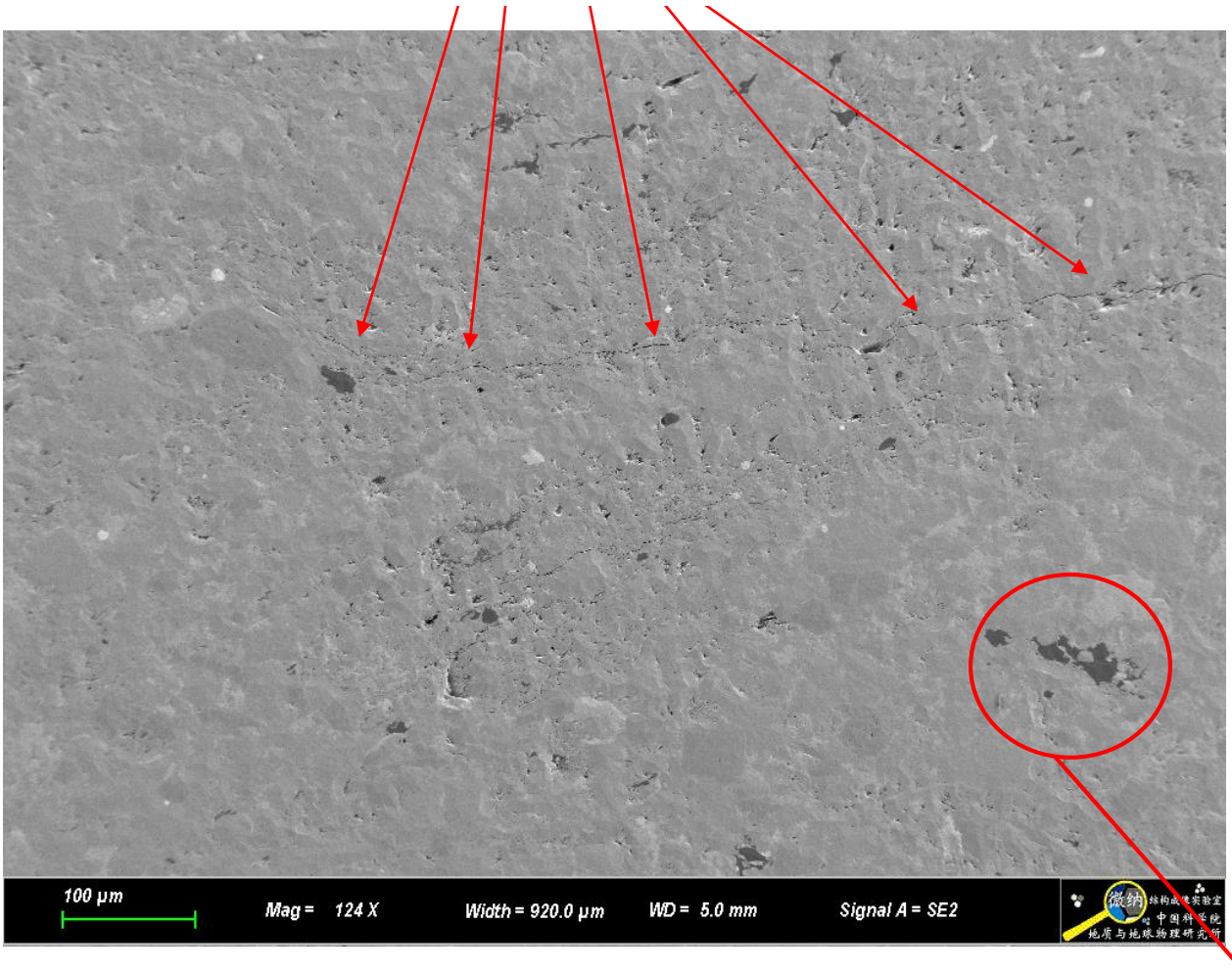

Figure 4-7-5: Larger scale image that allows for visualization of pockets of µm sized organic matter and micro-fractures.

4-8 Contact Angle and Wettability

Contact angle was used to determine the wetting characteristics of the samples. A mixed wettability that leans more toward oil-wetting is suggested from the data. As seen in the graphs in Figures 4-8-3 through 4-8-5, n-decane quickly approached a contact angle nearing zero. This suggests that all samples are very oil-wetting at the relatively large scale of several mm. While API brine (used to emulate saline formation fluids) does show a relatively higher contact angle it is not so high as to suggest strong hydrophobic conditions. Table 4-1 compiles the estimated contact angle at 30 seconds (dashed vertical lines on graphs). For samples with a result range from zero to a number—e.g. 7.89 to 0, no discernable angle could be measured at 30 seconds. The first number in this situation is the last obtainable measurement.

Sample ID	API brine (^{0})	n-decane (^{0})
35F-2380	10.96	7.89 to 0
35F-2386	9 to 0	5.78 to 0
9F-3891	42.71	5.67 to 0
9F-3971	39.04	4.34 to 0
9F-3973	No data	4.38 to 0
22F-6340	8.16 to 0	4.46 to 0
22F-12103	24.27	11.39 to 0
22F-12105	15.03	7.91 to 0

Table 4-8-1: Compilation of contact angle results.

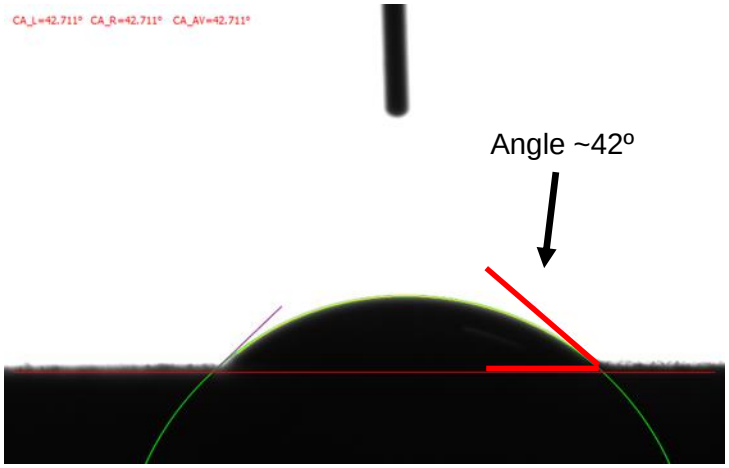

Figure 4-8-1: API brine contact angle of 9F-3891 at 30 seconds.

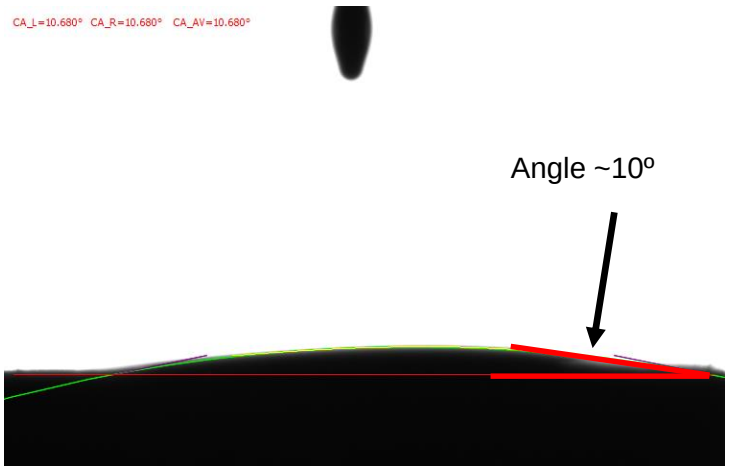

Figure 4-8-2: N-decane contact angle of 22F-12105 at ~1 second.

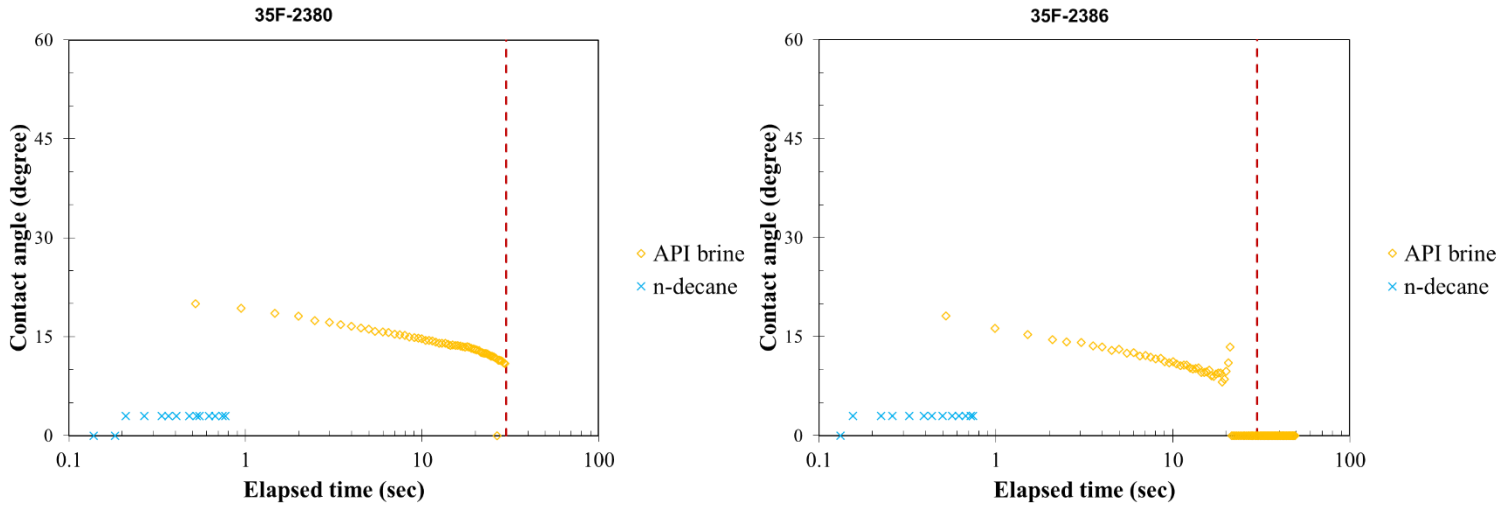

Figure 4-8-3: Contact angle results for samples from well 35-1 Federal/C-15234.

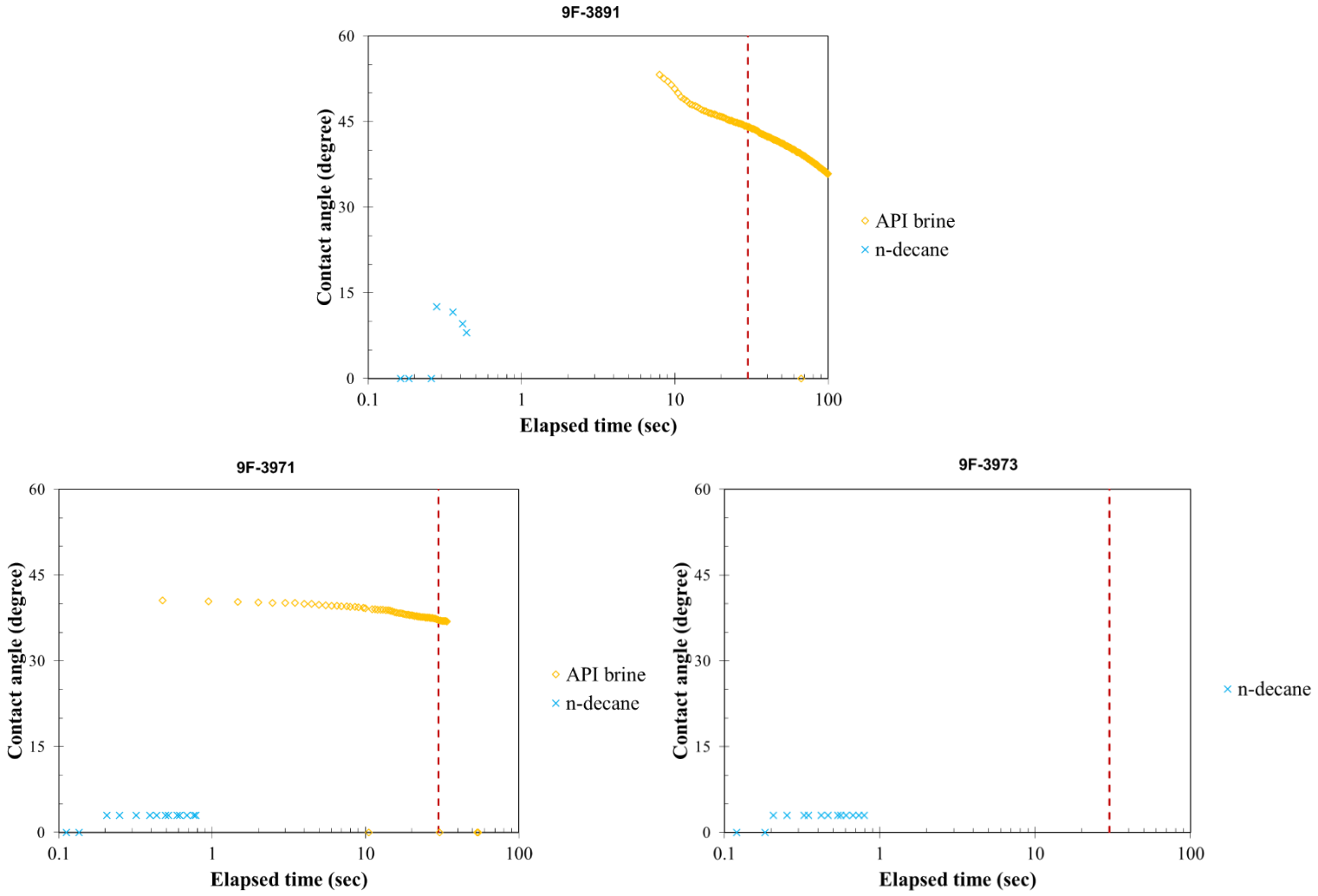

Figure 4-8-4: Contact angle results for samples from well 9-17-1-103 Federal.

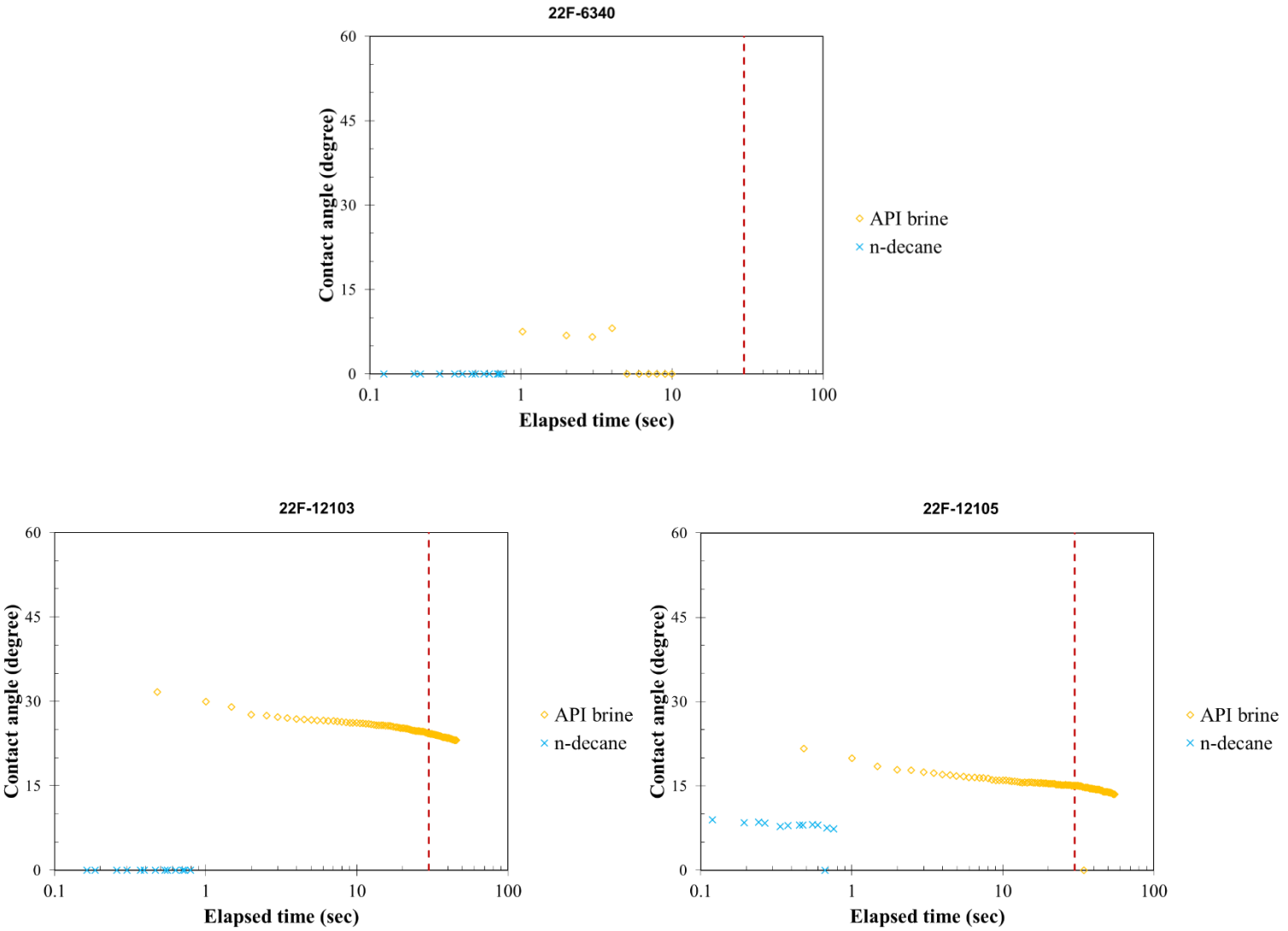

Figure 4-1-5: Contact angle results for samples from well 22-12 Federal.

4-9 Imbibition

Imbibition experiments help to further the understanding of a sample's matrix pore network characteristics. Mathematically analogous to diffusion in a well-connected pore space imbibition will create a wetting front in the sample that advances with the square root of time. If porosity within a well-connected sample is constant and gravitational effects are negligible, then the cumulative mass of the fluid imbibed with also follow a square root of time relationship (Hu et al., 2012). By comparing results of experiments to the square root of time relationship displayed by classical homogeneous materials (slope of 0.5) sample pore connectively (even at different points within the sample/varying distances from the edge of a sample) can be determined. This is significant in that the sample's edge is analogous to a fracture. As the wetting front advances in the sample, the rate of imbibition will slow as well-connected porosity is filled. The remaining pores are those that form a more poorly connected pore network throughout the sample. This is depicted by the change in slope of the linear regression in the log-log plots of cumulative imbibition versus time as seen in Figures 4-9-1 through 4-9-8. Table 4-9-1 compiles imbibition results.

Sample ID	Fluid	Stage I	Stage II	Stage III	Stage IV
35F-2380	DI water	1.065	x	0.449	0.105
	n-decane	x	x	0.589	0.097
35F-2386	DI water	0.974	x	0.411	0.107
	n-decane		0.759	0.246	x
9F-3891	DI water	x	x	0.650	0.131
	n-decane	2.63	x	0.668	0.032
9F-3971	DI water	x	x	0.305	x
	n-decane	3.741	0.715	0.398	x
9F-3973	DI water	x	x	0.26	x
	n-decane	x	1.68	0.59	x
22F-6340	DI water	x	x	0.960	0.14
	n-decane	x	x	0.616	0.042
22F-12103	DI water	1.338	0.624	0.175	x
	n-decane	x	0.847	0.469	x
22F-12105	DI water	x	x	0.203	x
	n-decane	x	x	0.415	x

Table 4-9-1: Compilation of imbibition data.

Results from imbibition displayed slopes referred to as stages. Stage I is associated with the initial settling of the sample, this slope generally only lasts from 30 seconds to a few minutes. Stage II represents fluid uptake onto the surface of the sample, and generally 500 µm into the sample, which has better connectivity than the interior of the samples. Stage III is associated with fluid imbibition through the edge-accessible and connected pore spaces of the interior which represents pore connectivity of the rock matrix. Stage IV represents a low slope associated with fluid reaching the top. No sample displays all 4 stages/slopes.

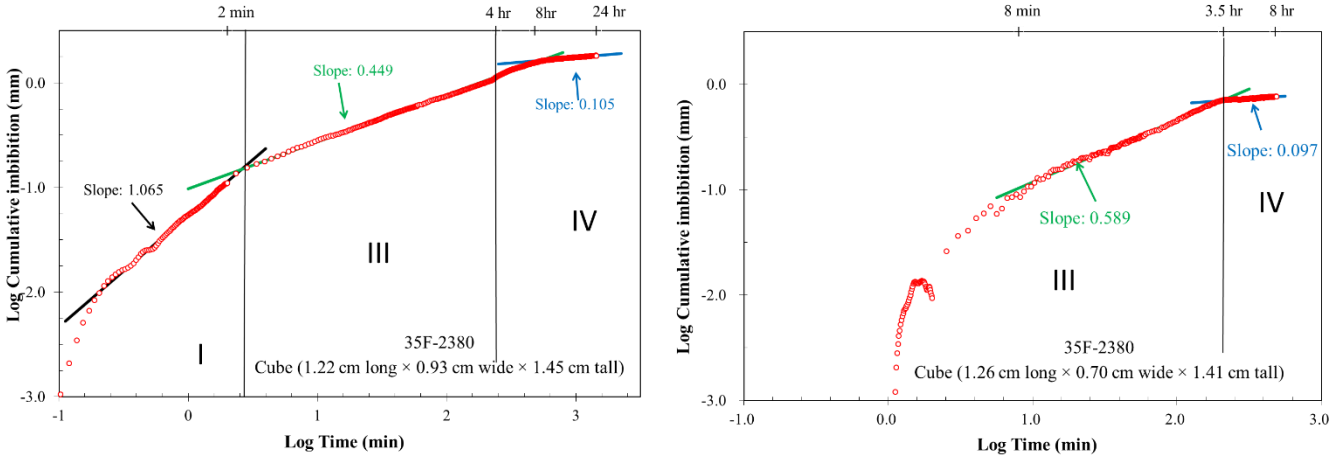

Figure 4-9-1: Imbibition plots for sample 35F-2380, DI water (left) and n-decane (right).

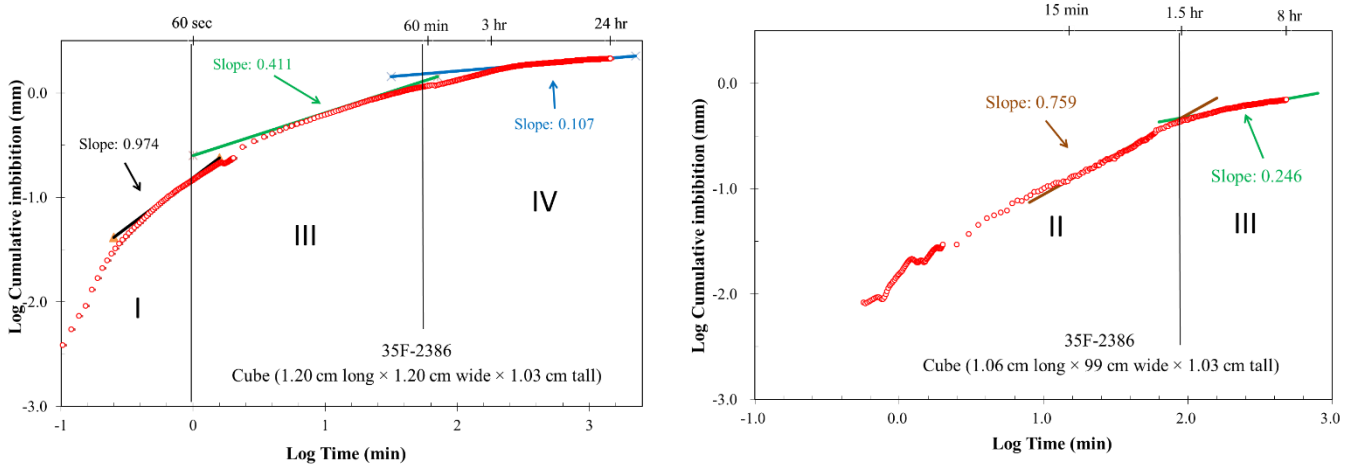

Figure 4-9-2: Imbibition plots for sample 35F-2386, DI water (left) and n-decane (right).

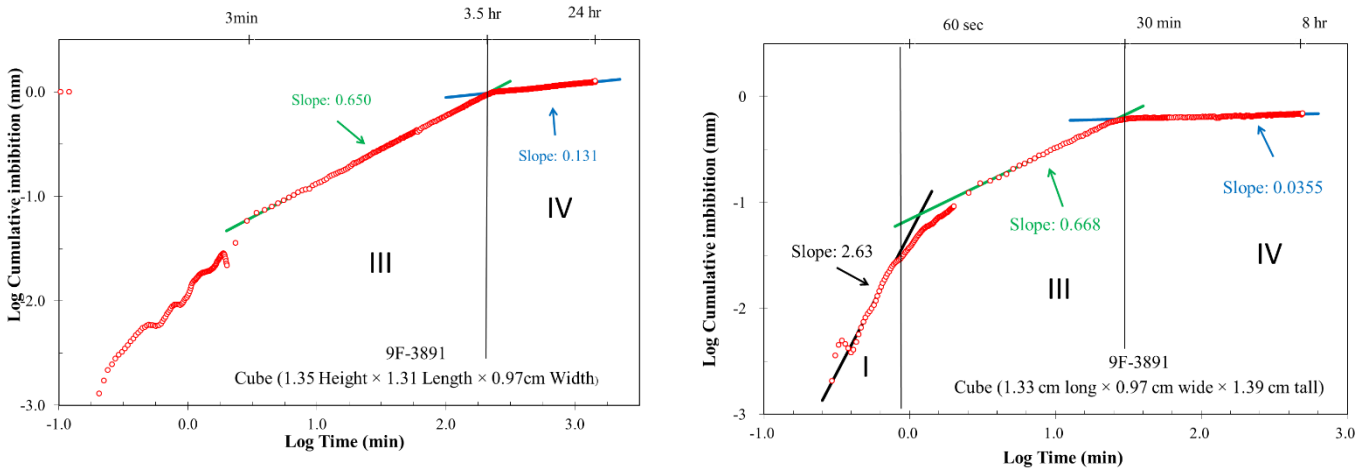

Figure 4-9-3: Imbibition plots for sample 9F-3891, DI water (left) and n-decane (right).

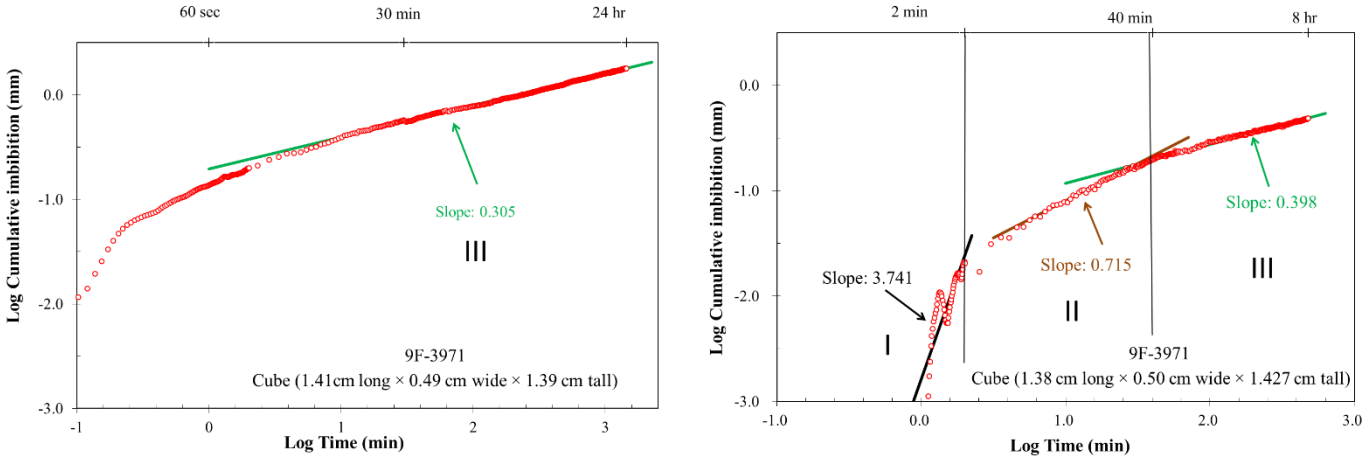

Figure 4-9-4: Imbibition plots for sample 9F-3971, DI water (left) and n-decane (right).

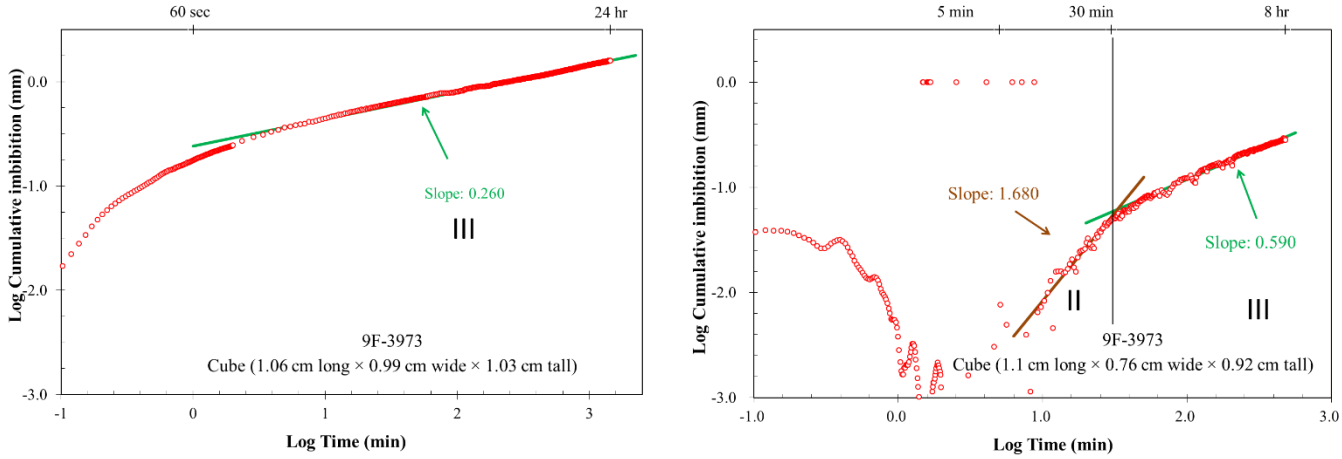

Figure 4-9-5: Imbibition plots for sample 9F-3973, DI water (left) and n-decane (right).

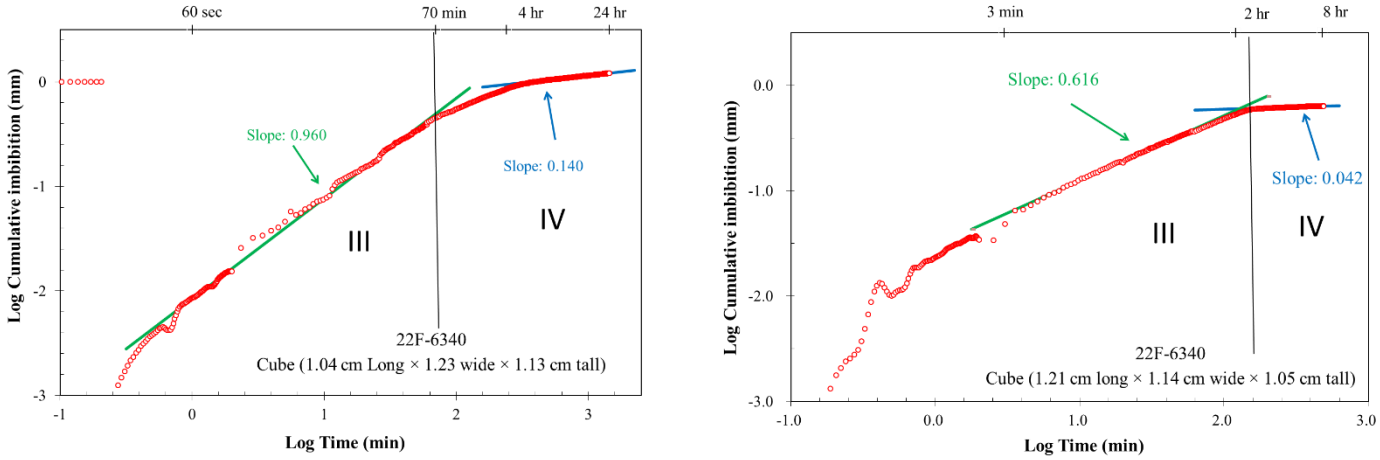

Figure 4-9-6: Imbibition plots for sample 22F-6340, DI water (left) and n-decane (right).

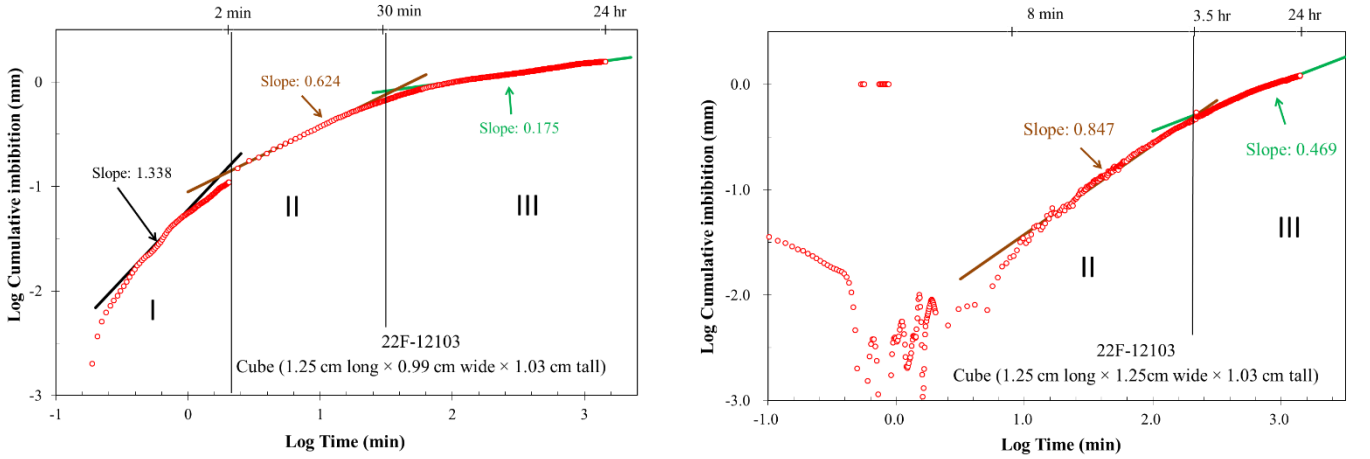

Figure 4-9-7: Imbibition plots for sample 22F-12103, DI water (left) and n-decane (right).

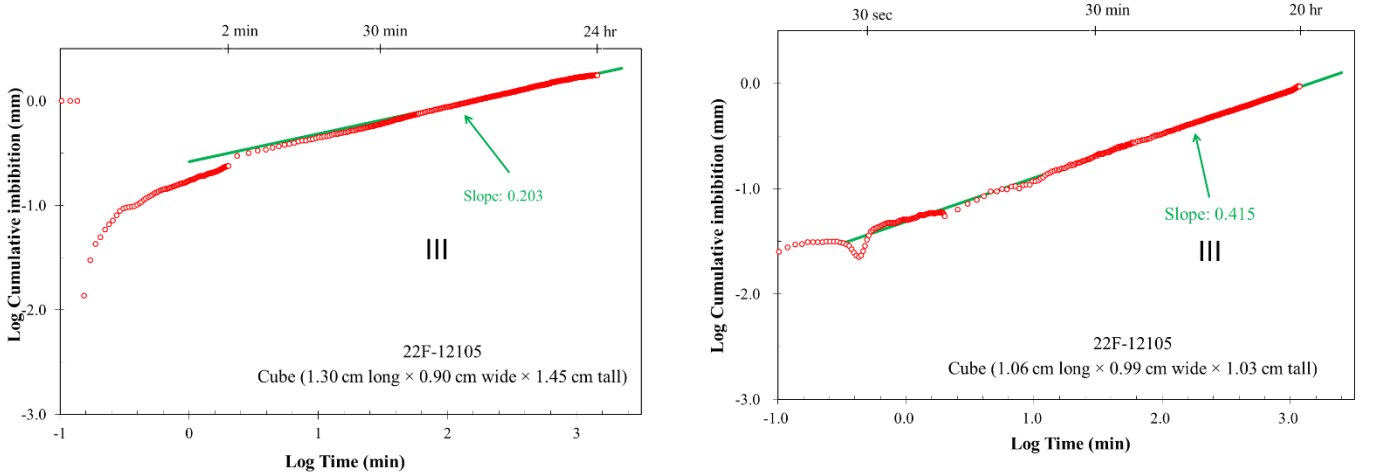

Figure 4-9-8: Imbibition plots for sample 22F-12105, DI water (left) and n-decane (right).

4-10 Production Data

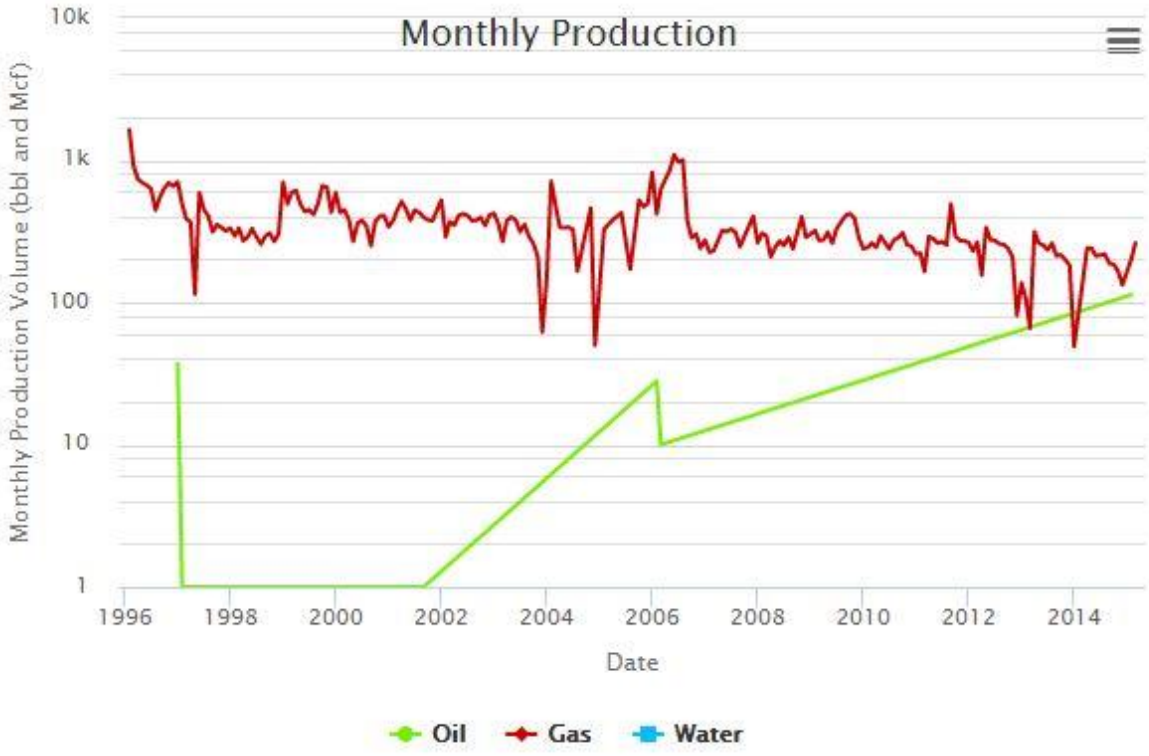

Figure 4-10-1: Production of well Federal 9-17-1-103 (Drillinginfo, 2017).

Well	Completed	Production
35-1 Federal/C-15234	March 9th, 1977	Dry hole
9-17-1-103 Federal	June 11th, 1981 Fracture treatment: January 2nd, 1996	February 1996 until March 2015
22-12 Federal	April 7th, 1981	Dry hole

Table 4-10-1: Drilling information (Drillinginfo, 2017).

Chapter 5

Discussion

5-1 Mineralogy and Geochemistry

Pyrolysis, XRD and TOC measurements allow for determination of chemical properties and mineral content. While not a strong relationship, TOC and clay do show a positive relationship as seen in Figure 5-1-1. This may suggest that areas of high clay content will likely have more TOC. Recalling from the geologic setting of this paper, Cole and Young (1991) discussed how the Mancos “B” is composed of many upward coarsening sequences composted of clay rich stratigraphy that grades into more silt and sand rich deposits. This sequence could potentially produce what Jarvie (2014) describes as a hybrid system, clay and organic rich deposits generate hydrocarbons that are expelled into an over-lying juxtaposed clay and organic lean interval. This organic lean interval tends to have better production characteristics. These include limited adsorptive affinities and a more brittle/prone to fracture mineralogy. This hybrid system tends to produce some of the best shale oil systems. Two examples from other regions are the Bakken Shale of North Dakota and the Eagle Ford Shale of Texas.

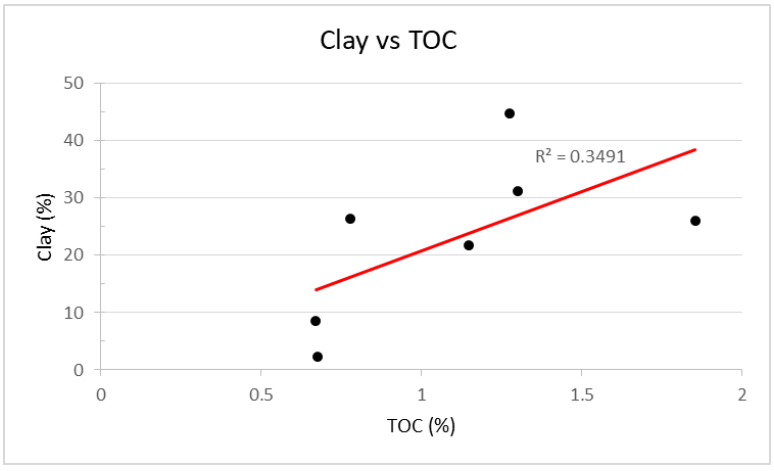

Figure 5-1-1: Graph of clay content versus TOC.

Kerogen type is also significant in hydrocarbon formation and therefore helpful in predicting production properties. From Jarvie (2014) we find that TOC is composed of two main components: a portion that can generate petroleum during maturation and a portion that will generate little to no significant hydrocarbons. These were named Generative Organic Carbon and Non-Generative Organic Carbon respectively. From Table 5-4-1, we can see that vastly different proportions of the original TOC can generate hydrocarbons based upon kerogen type.

Kerogen Type	Hydrogen Index Range	Generative Organic Carbon
Type I	>700	>60%
Type II	350-700	30%-60%
Type II/III	200-349	17%-29%
Type III	50-199	4%-28%
Type IV	<50	<4%

Table 5-4-1: Generative organic carbon values based on hydrogen index (Jarvie, 2014).

The kerogen type of samples in this project (see Figure 4-3-1) based upon hydrogen index and TOC fall within type III with samples 22F-12103 and 22F-12105 being type IV. That is significant because under the best of circumstances only under a third of the TOC will have the chemical properties to form hydrocarbons for type III samples and little to no hydrocarbons for type IV samples.

5-2 Pore Characterization Types: Type A vs. Type B

MICP results show a bimodal pore-size distribution between samples. Samples either tend to show a double peak pore-size distribution geometry that typically consists of a major peak between 500nm-800nm and a minor peak between 10nm-50nm or a single peak pore-size distribution geometry with one peak at approximately 10nm-50nm (Figures 5-2-1, 5-2-2). In this project these two patterns of pore-size distribution will be termed “type A” and “type B” with type A referring to the double peak pore-size distribution and type B to the single peak pore-size distribution. Table 5-2-1 organizes samples by pore-size distribution type. An example of type A pore-size distribution is shown in Figure 5-2-1 while a type B is shown in Figure 5-2-2. Since organic matter hosted pores are typically in the ~10nm range and develop during maturation it would be expected for more mature samples to fall within the type B pore-size distribution. From Figure 5-2-3 we can see that this is the situation for the most mature samples. This association between higher maturity and type B distribution begins to break down when taken into account that each of the two types has 3 samples all with relatively close maturities based on T_{max} (Figure 5-2-3). This suggests that there is more than just maturity affecting pore-size distribution.

Type A		**Type B**	
Sample ID	T-max	Sample ID	T-max
35F-2380	434	9F-3971	429
35F-2386	426	9F-3973	429
9F-3891	424	22F-12103	462
		22F-12105	469

Table 5-2-1: Samples by pore-size distribution type. T-max values from CUG.

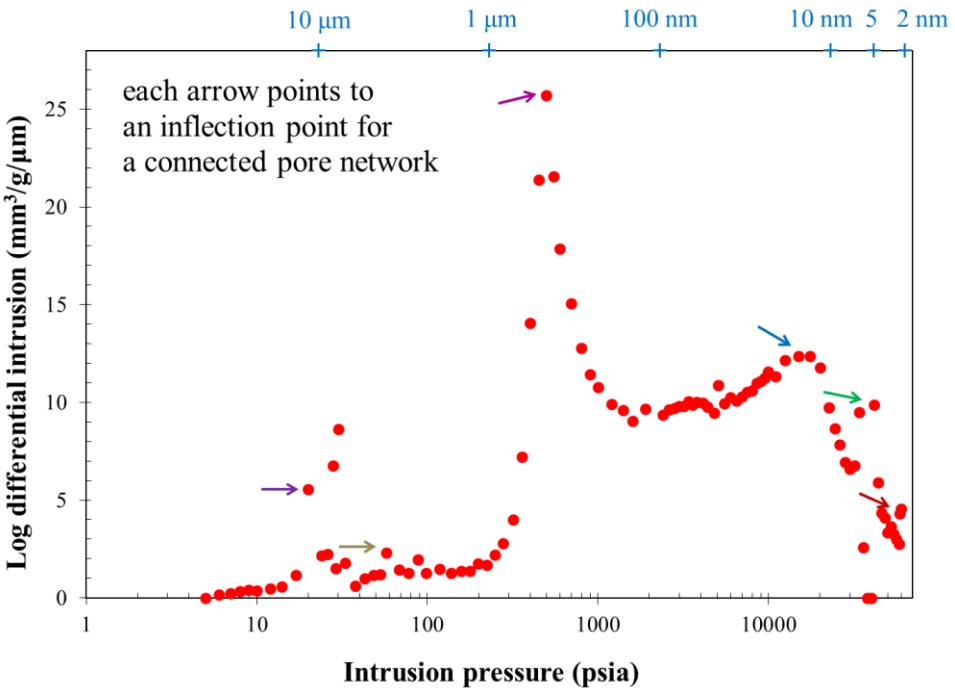

Figure 5-2-1: Type A pore-size distribution of sample 35F-2380 from MICP. Note major peak at ~800nm and minor at ~20nm.

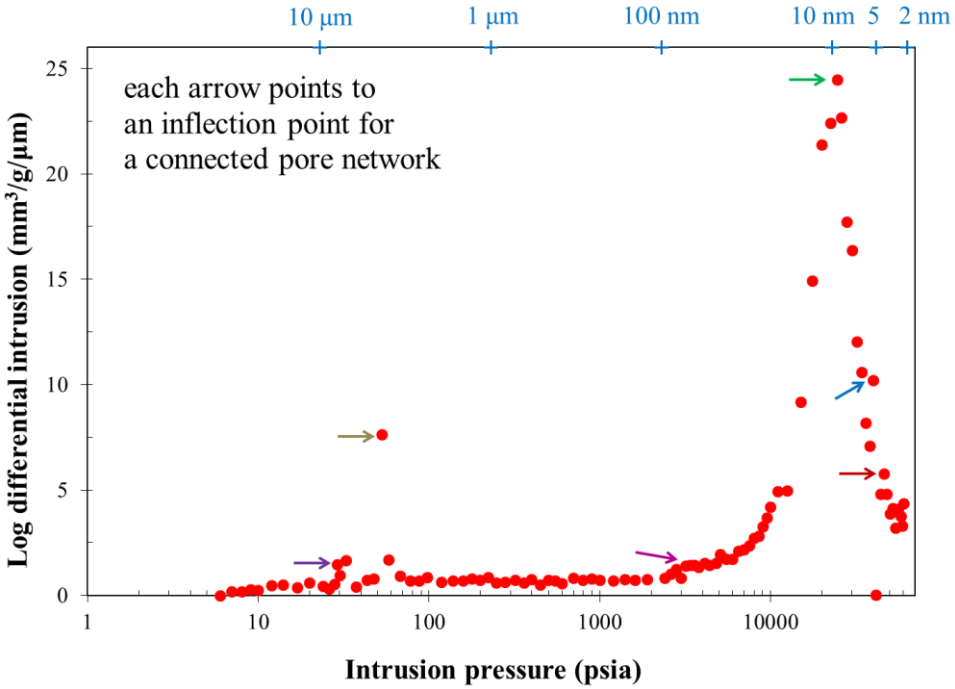

Figure 5-2-2: Type B pore-size distribution of sample 22F-12105 from MICP. Note major peak at ~10nm.

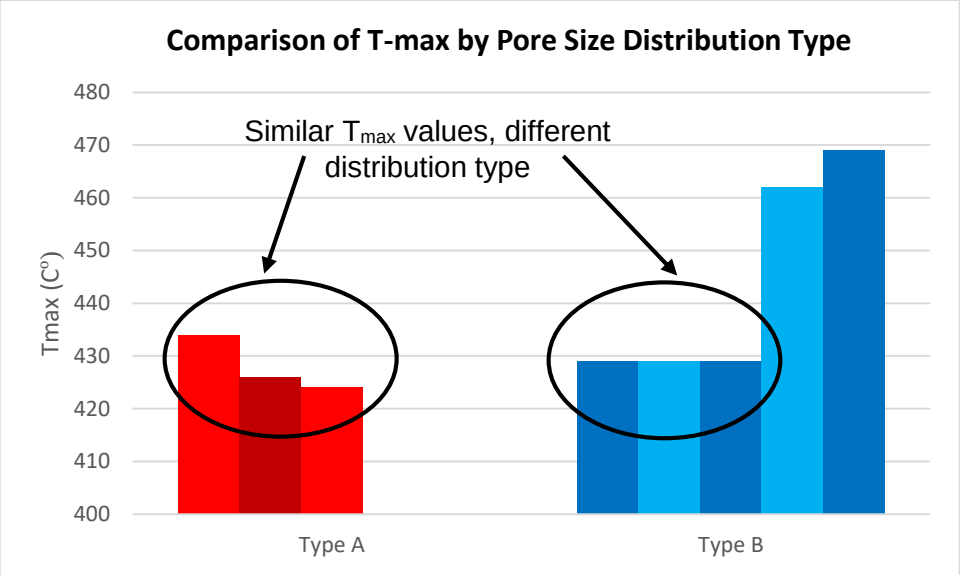

Figure 5-2-3: Comparison of estimated maturity (T-max) by sample type.

Another aspect that could influence pore-size distribution is the effect of compaction. The three type A samples happen to be the three shallowest samples. This could suggest that since type A has a major peak in the inter-particle pore range that type B does not, and that compaction decreases the space between grains among other effects, depth/compaction is a control on pore-size distribution. This hypothesis that compaction is a variable in pore type is in agreement with results when considering the two 35F samples but does not tell the full story since 9F-3891 also falls within type A. While it is likely that the difference in depth between the 35F samples and the 9F samples of over 1,500 feet could result in different amounts of compaction, the difference in depth of ~100 feet between 9F-3891 and 9F-3971/3973 is not as likely to cause a drastic change in pore-size distribution. Therefore it is likely that compaction isn't the only variable, like maturity, influencing pore-size distribution.

Comparing 9F-3891 to samples 9F-3971 and 9F-3973 (use Figure 3-1-4 and Table 4-1-1 for reference) there is a large discrepancy in clay content. This lack of clay could have a twofold

effect on pore-size distribution. First a lack of clay may have preserved inter-particle porosity during compaction were samples with higher clay content had clay platelets filling such voids. This would help explain the source of the large peak in the hundreds of nm range of type A . Secondly as seen in Figure 5-2-5 there tends to be a positive relationship between TOC and clay content. Curtis (2012) discusses how nano-porosity tends to establish it's self as secondary porosity during maturation within organic matter. Considering the relationship between TOC and clay it may be appropriate to postulate that the lack of clay (and therefore predominant organic-matter hosted nano-pore sized porosity) is responsible for 9F-3891 having essentially zero porosity smaller than ~10nm unlike the other 9F samples as seen in Figure 5-2-4.

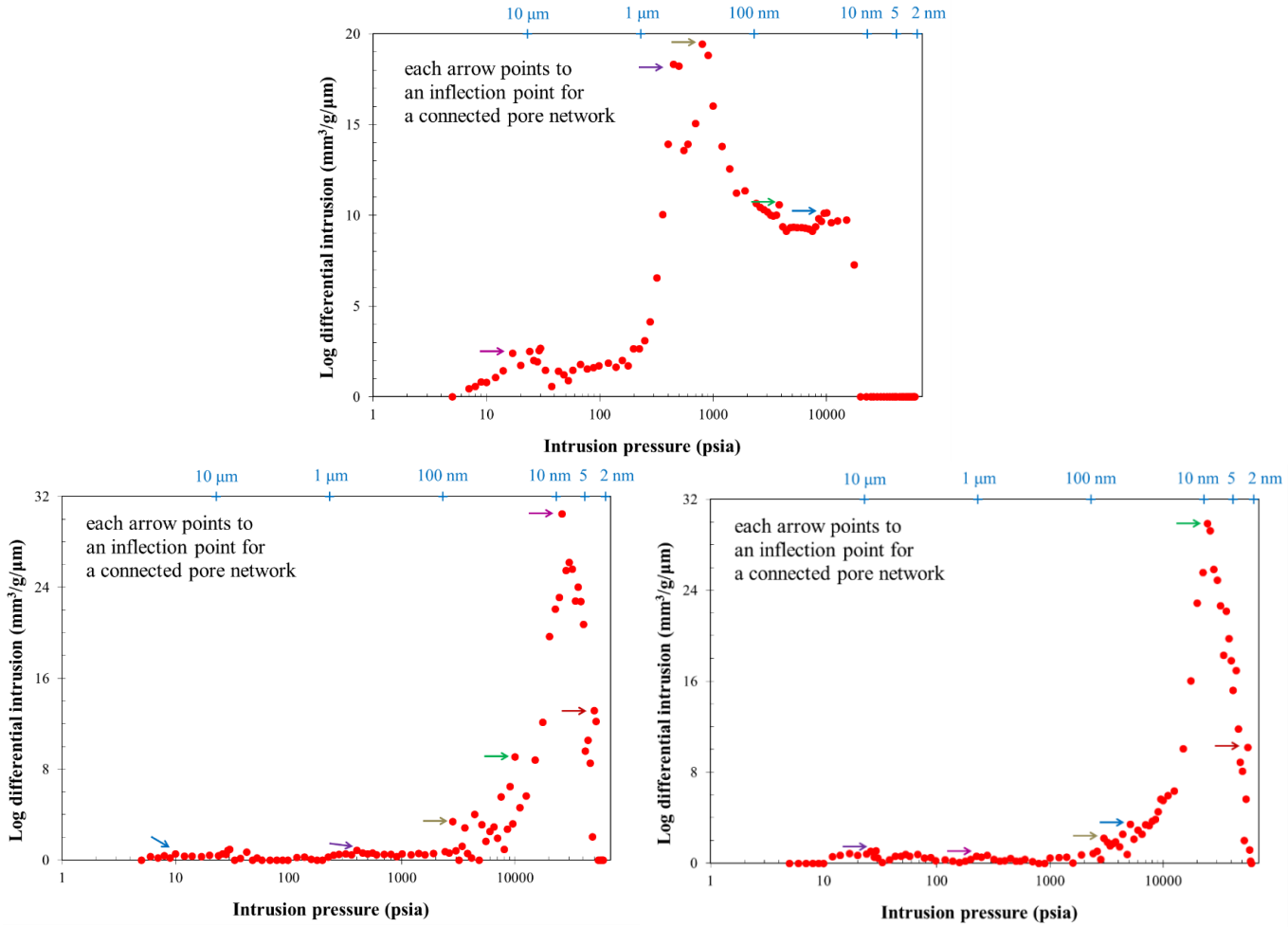

Figure 5-2-4: Pore-size distribution for samples 9F-3891 (top), 9F-3971 (bottom left) and 9F 3973 (bottom right). Note the lack of mercury intrusion for sample 9F-3891 below 10nm, this may be due to the low clay content of the sample.

Besides the difference in pore-size distribution there is also likely a disparity in pore geometry in type A and type B samples. Sample 35F-2380 (type A), the only sample to undergo nitrogen physisorption, was suggested to be a type 3 hysteresis loop based upon Sing (1985). A type 3 hysteresis loop is characterized by plate-like particles giving rise to slit-shaped pores. Given this and FE-SEM imaging of type B sample 9F-3971, both type A and type B contain these slit-shaped pores. Due to their different pore-size distributions their ratio of slit-shape matrix pores compared to more rounded organic matter hosted porosity is different with type A being much greater. From Figure 4-7-3 sample 22F-12103 is seen to contain slit-shaped pores in the 100-1000nm range but from its pore-size distribution (Figure 4-5-4) we see that for this sample a 100-1000nm pore-size is not prevalent at 8% of total. Therefore it is likely that type A and type B pore geometry differs in that type A tend to be made up of these 100nm to 1000nm slit-shaped inter-particle pores while type B have a greater proportion of their porosity coming from more rounded organic matter hosted pores.

5-3 Porosity and Permeability

In a hybrid petroleum system a source rock is juxtaposed with organic-lean rock, and tends to not show a correlation between porosity and TOC in highly mature shale formations. A positive correlation between porosity and TOC is suggested by Jarvie (2014) to mean that most of the porosity in a mature system is hosted in organic matter. In Figure 5-3-1 the porosity (from MICP) has been plotted against TOC, and a general negative correlation is found. These results cannot be directly related to the Jarvie (2014) relationship between clay and TOC, due to the relatively low maturity of some of the samples. Curtis (2012) states that typically organic hosted porosity doesn't form until a vitrinite reflectance value of 0.8% or more. It is important to note that sample 9F-3971 did show organic hosted porosity in FE-SEM images (Figure 4-9-2) at only an estimated vitrinite reflectance of 0.69% (CRC, 2017). Since there is some established organic hosted porosity in 9F-3971 from SEM imaging (and therefore likely 9F-3973 too) and

the two 22F samples have an estimated vitrinite reflectance greater than 0.8%, these samples were plotted separately in figure 5-3-2. Figure 5-3-2 produces a slight positive relationship between porosity and TOC (small sample size likely contributes to low R^2 value). This suggests that in more mature samples organic hosted porosity holds a greater portion of the porosity compared to type A. This is further supported by MICP pore-size distributions (see figure 4-5-6) that show the bulk of the porosity being in the 10nm-50nm range for the relatively more mature samples.

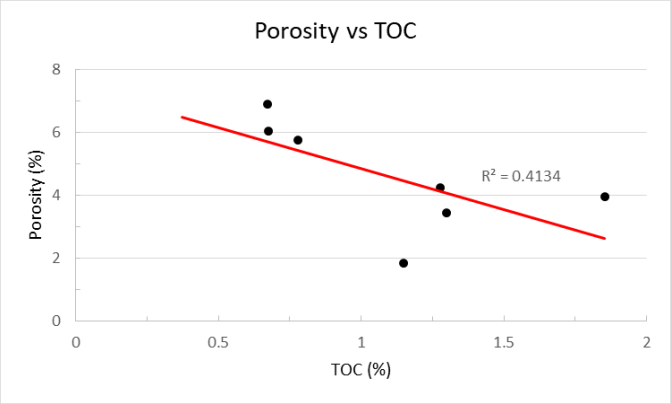

Figure 5-3-1: Porosity vs TOC for all samples.

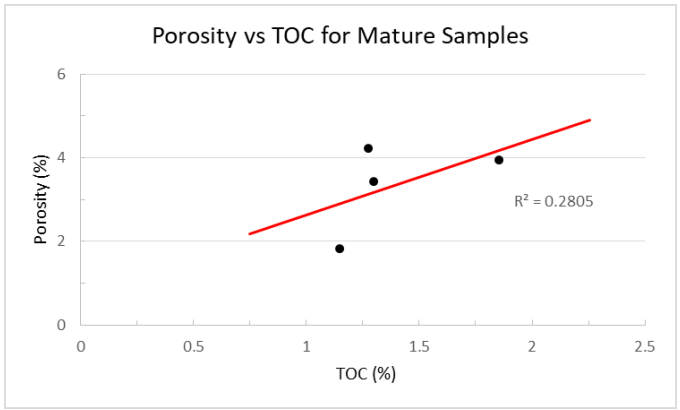

Figure 5-3-2: Porosity vs TOC for only the relatively mature samples

Helium porosity and permeability measurements show the significance that fractures and laminations have on the fluid flow characteristics of a sample. The larger sized sample of the plug used for helium tests had significantly higher porosity and permeability than MICP results. Zones of high porosity and permeability, likely an effect of lamination, are probably partly responsible for the discrepancy in Helium vs MICP results. Also helium traveled parallel to bedding while mercury intruded from all directions. Due to the highly anisotropic behavior of laminated shales this would only serve to amplify the differences in results. This behavior highlights just how important the orientation of laminations and bedding planes is to the movement of fluids within a highly laminated unit such as the Mancos “B”.

5-4 Pore Network Wettability and Connectivity

The results from contact angle experiments tend to show a mixed wettability that leans toward more oil-wetting. As we can see from Table 4-8-1 all samples were extremely oil wetting with n-decane spreading quickly to a point that an angle could not be measured only seconds after application (Figure 4-8-2). Water wettability between samples is more variable than oil wettability. While most samples displayed similar wettability between API brine and n-decane, samples 9F-3891 and 9F-3971 were outliers that showed more hydrophobic behavior with larger API brine contact angles. Figure 5-4-1 graphs T_{max} (estimate of maturity) to contact angle of API Brine to compare maturity to water wettability. Since samples of relatively low maturity measured both higher and lower contact angles than the most mature samples it is unlikely water wettability at a macro-scale is being influenced by maturity of samples. Instead mineral composition is likely the greatest factor in contact angle.

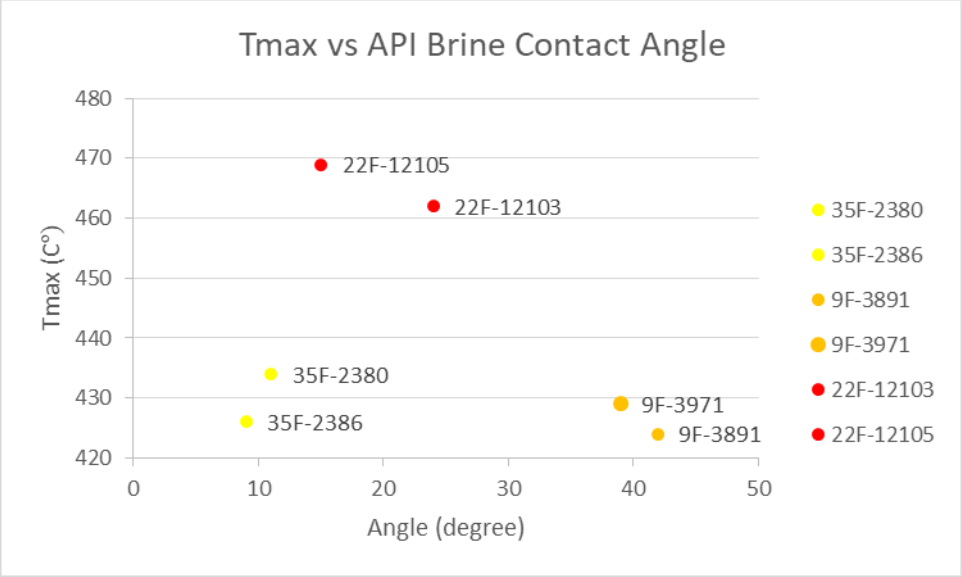

Figure 5-4-1: Graph of T_{max} versus API brine contact angle.

Imbibition results generally conclude with wettability results in that the samples are of a mixed wettability leaning towards oil wet. This is suggested by the higher imbibition slopes of samples when tested with n-decane compared to API brine. Type A samples tended to be well connected in both n-decane and DI water tests. Samples 35F-2380 and 9F-3891 share very similar imbibition slopes with each having stage III slopes lasting 3.5-4 hours and a slope that indicates high connectivity. Comparing these two samples to 35F-2386, 35F-2386 is not as well connected in regards to oil-wetting pores. N-decane testing did not reach the top like the other two type A samples while having similar dimensions as them. Also the n-decane stage III slope is much lower at 0.246 compared to >0.5 for the other two type A samples. Mineralogy may play a role here as 35F-2386 is composed of 26% clay minerals while 35F-2380 and 9F-3891 have 8.5% and 2.2% respectively. With type A samples' relatively good fluid properties (for shale) but low TOC, poor kerogen type (type III), and low maturity, units composed of type A like samples are a likely candidate for production from hydraulic fracture simulation if there is evidence that the unit has been sourced in a conventional sense from a more mature and TOC rich unit. USGS (2016) suggests that production in the Mancos "B" in the Douglas Creek Arch area comes from conventional tight reservoirs.

Type B samples are less connected than type A samples (especially water-wetting pores networks) as evident by their stage III slopes and the fact fluid didn't reach the top like in type A samples (no stage IV). Type B samples have a relatively well-connected oil-wetting pore network based upon the stage III slope values. This network is likely formed during maturation as organic matter begins to produce hydrocarbons. This creates organic hosted (which are oil-wetting) pores. Unlike type A samples, type B samples do not have well-connected water-wetting pore networks. With the exception of 22F-12103, DI water imbibition in type B samples produced a low and constant stage III slope.

Chapter 6

Conclusion

MICP results indicated that two types of pore-size distributions generally occurred. Type A is characterized by a major peak between 500nm-800nm and a minor peak between 10nm-50nm. Type B pore-size distribution entails a single peak at approximately 10nm-50nm. While maturity plays a role in pore-size distribution it is suggested from the data that mineralogy/lithofacies is the dominant factor in pore-size distribution type. The type III and type IV kerogen found in these samples will be gas prone and limit the amount of hydrocarbons generated due to their high percentages of Non-Generative Organic Carbon.

This is some evidence that clay content has multiple effects on samples. First there was a slight positive trend between clay content and TOC. Secondly samples with very low clay content such as 35F-2380 and 9F-3891 tended to have less pores smaller than 10nm. Clay content, likely due to its association with TOC, tended to improve oil-wetting pore connectivity in imbibition tests. Maturity is significant in the formation of organic hosted pores. Since clay is associated with organic matter (TOC) intervals of low clay may lack the organic matter necessary for organic hosted pores to form with maturation. Also samples with greater clay content developed greater connected oil-wetting pore networks.

Immature samples tended to be mainly slit-shaped pores with 100-1000nm pore-throats while more mature samples tended to have a combination of both with the majority of pore volume in more rounded organic hosted pores. Curtis (2012) stated that slit-like pores are prone to collapse due to increased effective pressure as hydrocarbons are produced. Besides the low matrix permeability of shales, the closing of pores will exacerbate declines in production. This problem is likely to be more prevalent in lower maturity rocks that haven't formed the more rounded and therefore more resilient organic hosted pores. This suggests that during hydraulic

fracture treatments in lower maturity rocks proppant used in the fracking fluid meant to keep pores open during production may play a more significant role than in highly mature formations.

Imbibition results show that type A samples are well connected for both DI water and n-decane tests. Type B samples displayed poor connectivity with DI water in contrast but had fairly good (slope near 0.4- 0.5) n-decane connectivity. Organic hosted pores that form during maturation are likely to contribute to the oil-wetting connected pore networks of type B samples. Units composed of Type A samples might be a good candidates for production if a given unit has been charged with hydrocarbons from a source rock like in a conventional petroleum system. Type B samples are likely to produce a more unconventional petroleum system (both source and reservoir) with best production likely to come from areas of high TOC and type III kerogen.

Appendix A- Core Research Center Data

The USGS Core Research Center maintains data that was provided from previous researcher's experiments on core samples taken from their storage facility. For the well Federal 9-17-1-103, pyrolysis data sourced from the Core Research Center and summarized in Table Appendix A-1 for depths 3891.8' and 3972.8'. Figure Appendix A-1 is a graph of hydrogen index versus T_{max} similar to Figure 4-4-1. While the CRC data tends to have higher S2 and T-max values, both plots of HI versus T-max produce similar results of type III/IV kerogen.

Well	Depth (ft.)	TOC (%)	S1 mg HC/g	S2 mg HC/g	S3 mg CO_2/g	S3 mg CO/g	T-max	HI S_2x100/TOC	OI S_3x100/TOC	PI $S_1/(S_1+S_2)$	OSI S_1x100/TOC	VR_o-Eq
Federal 9-17-1-103	3891.8	1.12	0.17	1.58	0.1	0.03	436	141	8.93	0.1	15.18	0.69
Federal 9-17-1-103	3972.8	1.22	0.16	2.29	0.07	0.3	433	187	5.74	0.07	13.11	0.63

Table Appendix A-1: Summary of pyrolysis data from CRC.

Table Appendix A-2 shows the vitrinite reflectance for well 35-1 Federal/C-15234 at depth 2383ft. This reflectance was taken as an initial estimate for maturity in sample selection of 35F-2380 and 35F-2386. The assumption was made that these shallower depth samples where likely to be less mature than other samples as is reflected in the vitrinite reflectance in Table Appendix A-2. In contrast, pyrolysis testing in this project suggested that the 35F samples were of similar maturity to the 9F samples

Well	Depth (feet)	Vitrinite Reflectance (R_{max})
35-1 Federal/C-15234	2383	0.375

Table Appendix A-2: Vitrinite reflectance from CRC of a sample near the depths of the CO 35F samples of this project.

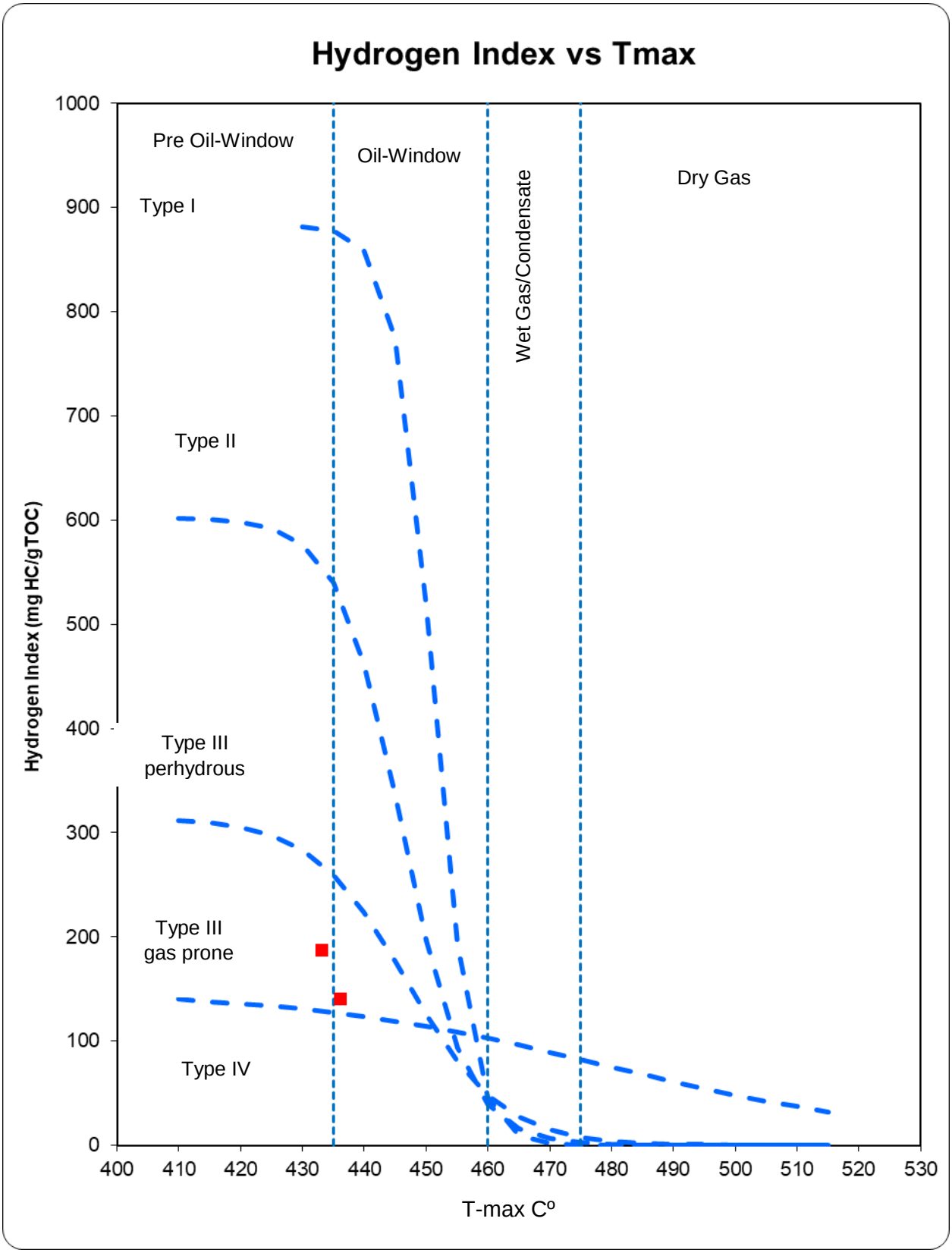

Figure Appendix A-1: Plot of hydrogen index versus T-max from pyrolysis data to determine kerogen type.

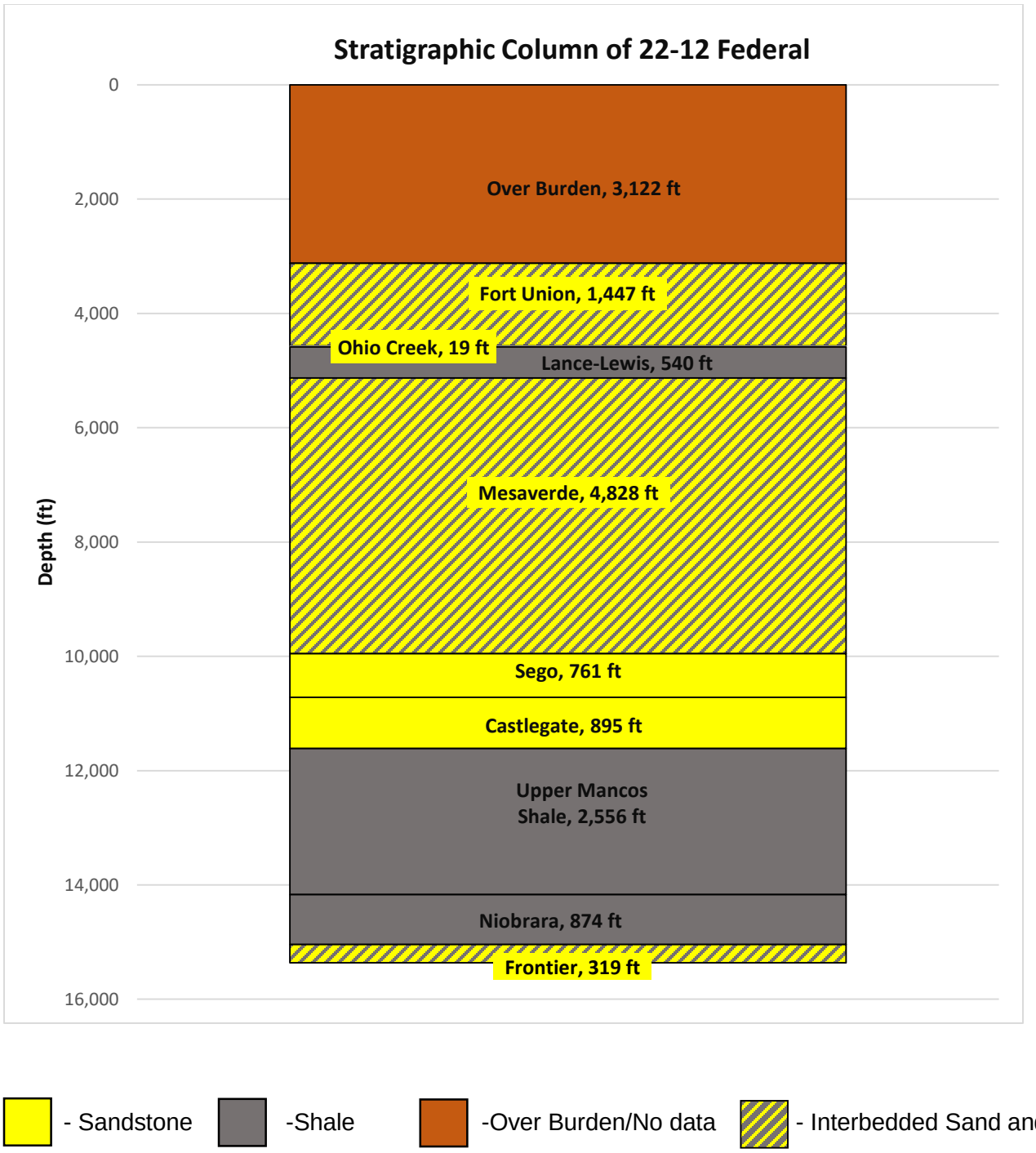

Figure Appendix A-2: Stratigraphy of well 22-12 Federal approximated from formation tops.

Appendix B- Shimadzu Institute

MaximaX XRD-7000: Shimadzu X-ray Diffractometer

Sample Preparation

- Prepare your sample by compacting the sample into the sample holder using a glass slide
- Avoid vertical loading by removing excess sample with the edge of the glass slide
- Attempt to make your sample as flat and homogenous as possible; once this is completed your sample is ready to be analyzed.

Power Operations

- Turn the chiller on by pressing the power button (on the face of the chiller), a green light will illuminate.
    - Allow the chiller to sit for ~20 minutes to adjust to the proper temperature.
- Turn the XRD on by pressing the power button on the left hand side. The green power button will illuminate on the front panel of the XRD.

XRD Calibration:

- Locate and open the [PCXRD] program on the desktop. The main “XRD-6100/7000” panel will display.
- Click the [Display and Setup] icon, a “door alarm check” window will pop up. Follow the prompt to open and close the XRD door, once complete click “Close”. An “IOcon” window will pop up with the message “Now Calibration! If ready OK”, Click “OK”.
- The XRD is officially calibrated and ready to process your sample.

Setting Analysis Conditions:

- To set the processing conditions go to the “XRD 6100/7000” panel.
- Click on the [Right Gonio Condition] icon to open the [Analysis Condition Edit Program] window
- Click the blue bar under [Measurement Mode: Standard] to open the [Standard Condition Edit] window.
- Most of the settings in the [Standard Condition Edit] window will be preset. Only a few conditions will need to be changed.
- The following general condition settings will work for a wide array of materials.
  It’s very important to follow these next steps, double check any settings you change ensuring to follow these guidelines precisely. This will minimize minor mistakes when processing materials and will prevent damage to the detector.
    - Scanning condition: Scan Range (deg) = 2°-70° □ Optional Condition: Check the box [Option Enable]
    - Beta Attachment: Control Mode: Rotation
      Rotation Speed (rpm): 6

- Slit Condition: Slit Conditions are preset, and must be verified on the XRD to ensure the proper slit sizes match the settings listed under the Slit Conditions.
    - Checking the Slits:
        - Open the XRD door, on the left side of the XRD is the X-ray tube, the Divergence Slit is attached to the left side of the divergence soller slits.
        - On the right hand side will be the detector arm which contains a set of Scattering soller slits, the Scattering Slit faces the sample (Left) and the Receiving Slit faces the detector (Right).
        - If they are not the same sizes as what is preset in the [Slit Condition] box change the slit's so they do match.
    - Standard Slit Settings:
        - Divergence Slit: 1.0°
        - Scattering Slit: 1.0°
        - Receiving Slit: 0.3 mm

- Double check your settings and make sure they are correct, if they are click [OK].
- A [File & Sample Condition Edit] window will display; change the [Group name] to match your destination folder name and change [File name] and [Sample Name] to match your sample name, click [New].
    - Later samples can be created by simply changing the file and sample names and clicking [Modify].
- Click [Close] on the [Standard Condition Edit] window.

Starting the XRD Processing:

- Locate and click the [Right Giono Analysis] icon on the [XRD-6100/7000] panel.
- Your current sample name should appear highlighted blue in the upper portion of the [Right Gonio System: AnalysisCondition Edit Program] window. Highlight your sample and click [Append], this adds your sample to the list in the bottom portion of the window labeled [Entry for Analysis], click [Start]. Your sample should appear in the bottom of the [Right Giono Analysis & Spooler Program] window, click [Start] in this window. This officially starts the analysis process.
    - Indicators for Analysis: A clicking sound will come from the XRD when the locking mechanism on sliding door locks. On the face of the XRD a yellow light should illuminate under [X-RAYS ON].
- Leave all software windows open and allow the XRD to process your sample, this should take ~30 minutes.

Completed XRD Processing:

- A complete peak spectrum should appear in the [Right Giono Analysis & Spooler Program] window upon completion.
- The green [Analyzing!] Box should disappear and the yellow [X-RAYS ON] light should turn off.
- If you have more samples to analyze, continue to run your samples in the same manner listed above.

Opening Peak Profile Spectrum:

- Locate and open the icon for the [MDI jade 9] software on the Desktop.
- Under [file], click [Read], locate the folder [xddat] under [favorites]. Locate the folder where your samples are saved.
- In your folder, each sample should have a [.RAW] file, use this file to open your selected spectrum in the [Jade 9] software.

Identifying Minerals in Peak Spectrum:

It's important to have an educated background on the sample you're analyzing. Knowledge regarding the bulk composition and what you're searching for will greatly reduce the amount of time spent IDing the various peaks in the spectrum.

- Locate the [Find Peaks] icon on the main tool bar next to the [Floppy Disk/Save] icon, this will identify and mark any statistically significant peaks within the spectrum
- Choose a mineral database: At the top of the panel to the right of the spectrum window, there will be a drop down menu choose the [RDB-Minerals] as the database. The RDB-Mineral database should be predominately used to identify most minerals in your spectra.
    - If you cannot find a mineral in the RDB-Minerals database change to the [PDF+4 Minerals] database library, but be sure to change back to the RDB database once the mineral is located.
- Begin searching for minerals based on your pre-existing knowledge regarding the sample. When you identify minerals that fit your peak spectrum hit [Enter] on the keyboard, this process will add the minerals to a compiled list of those minerals which you identified in the spectrum.
- Once you have exhausted your initial hypothetical list of minerals, a helpful tool to use is the [Line Based Search/Match]. Go to the main tool bar and locate [Identify] and select the [Line Based Search] option.
    - This tool will compile a list of minerals by searching a selected PDF database for entries with peaks which are statistical matches for the peaks identified within your spectrum.
    - Settings:
        - [Two-Theta Error Window] max setting should be no more than 0.24%
        - [Top Hits to List] max setting 80
    - Set the parameters and click the blue [Play] icon next to the [X] to run the search and generate a list of possible phases that might fit your spectra. *Note: the line based search should not be used as a primary way to identify the bulk mineral mode of the sample as the software is not consistent when generating phases and will possibly leave out important phases for the spectrum*.

Model Analysis:

- Once all minerals have been ID'd, check that they have been added to the mineral list by pushing [Enter] on the keyboard.
- Click the [%] icon next to the drop-down mineral list located on the toolbar in the middle of the window to begin modal analysis.
    - An overlay will appear with different chart configurations of the modal results, to change the configurations of the chart use the drop down menu in the chart window.

- To view the modal analysis in text format: locate and click the […] icon near the [%] icon. This will list the minerals by name, chemical formula, and the normalized weight percent for each mineral. It will also state if the mineral is a [major], [minor], [trace], or [absent] component in the sample.
- If you would like to remove a mineral from your mineral list at any time, highlight the mineral and press [Delete] on the keyboard. [Absent] phases should be removed from the list by this method.

Analysis Check with Pattern Deconvolution:

- A key indication that the peak spectrum has been fully fitted and identified is by using the [Pattern Deconvolution] tool which automatically runs with the modal analysis.
    - The pattern deconvolution tool will generate a red overlay spectrum on top of the original white spectrum.
    - This process is generating a [Best Fit Profile] composed of the selected mineral standards from the [Mineral PDF database library] with your sample spectrum.
    - If all minerals have been properly identified, then the red deconvolution overlay will match the peak spectra for each peak. If there are peaks that don't have the red deconvolution overlay then those peaks have not been identified.
- Continue processing your spectrum until your original spectra and the deconvolution spectra match.

Saving Data:

To save your data,

- Go to [file] and [Save], save your data under [Current work as *.SAV]. This will save all analysis as a separate file.

Shimadzu TOC-V_{ws} SSM-5000A

The SSM-5000A is a solid sample module which can run two types of analysis, Total Carbon (TC) and Inorganic Carbon (IC), both of which are analyzed by a nondispersive infrared detector (NDIR). By subtracting the IC values from TC values, the Total Organic Carbon (TOC) of a sample can be quantified.

Methods

The TC method

- Uses the electric furnace to heat the combustion tube to 900°C, this allows the carbon combustion oxidation reaction to occur and will yield carbon dioxide which will be analyzed through the NDIR.

The IC method

- Uses the electric furnace to heat the combustion tube to 300°C, and, by adding 0.4 mL of 33% Phosphoric Acid (H_3PO_4), for the carbonate acidification reaction to occur, will yield carbon dioxide which will be analyzed through the NDIR.

Sample Table

a. Open [TOC-V Sample Table Editor] icon and enter your initials

b. Click the [New] icon in the [Sample Table] window

c. Select [SSM-5000A] for the H/W System Settings

d. Select icon labeled [Connect] located on the top row of the window

e. Right click on the number 1 in the Sample Table window and select the [Insert Sample] tab

f. Select [Calibration curve] parameter and search in the Thawspace (T:) Drive for the folder labeled [SSM-5000A_CalCurve].

g. Depending on which type of analysis will be run you will choose the file "TC_CalCurve_SSM5000-A" for Total Carbon or the "IC_CalCurve_SSM5000-A" for Inorganic Carbon.

h. Select [Next], then specify your [Default Sample Name] (e.g., Bob-Shales) and specify your [Default Sample ID] (e.g., LS_1200)

i. Select [Next], then assure the units are in mg/L and leave the [Expected Conc. Range] as is, this number is negligible.

j. Select [Next] and assure your integration time is maxed out at 20:00 min, then select [Finish].

Sample Boat

There are two distinct Tupperware boxes with sample boats depending on which method is used.

a. When using the TC method, use the box labeled “Heat Treated Sample Boats”.

b. When using the IC method, use the box labeled “Acid Treated Sample Boats”.

i. Use tweezers to grab a clean sample boat from its respective box and place it on the scale.

ii. Once the scale has balanced out and a right directional arrow appears on the screen, press the [O/T] button to tare the scale.

iii. Carefully use the scoopula to scoop a small amount of your sample into the boat. (ideal weight 30-70 mg)

iv. Once the scale has balanced out, record the weight in mg. This value is used to calculate the concentration of carbon.

Collecting TC

a. Return to the [Sample Table] and click on row number 1 where you inserted your first sample and make sure it is highlighted.

b. Select the [Start] icon located to the left on the second row of the [Sample Table Editor] window.

c. To run your first sample you will be required to name your Sample Table in the Thawspace (T:) Drive (e.g., Bob_Shales_2017_05_01).

d. Next, you will be prompted to enter the weight (mg) of your sample obtained from the balance. DO NOT PRESS START.

e. Carefully open the TC chamber by turning the blue knob counter clockwise and slide the cover over to the right.

f. Place the boat on the metal sample boat holder, make sure it is aligned so that it fits securely in the boat holder.

g. Slid the cover back over the chamber and make sure it is tightened by rotating the blue knob in the clockwise direction.

h. Return to the Enter Sample Amount screen and once the weight is input select [Start].

i. If all background conditions are met, a green [Ready] icon will appear on the top right window and you will be prompted to [Push the sample boat into the measurement position] which you do by pushing the front blue knob all the way forward.

j. To view your measurements, click the second blue icon in your sample window, it has an icon of a graph and a syringe.

k. Once your measurement is complete, you will be prompted to pull the boat back to the cooling position, this is the position located between the [sample change] and [measuring] position on the top panel of the instrument.

l. Once the boat has cooled sufficiently, you will be prompted to pull the boat back to the preparation position.

m. Once the sample boat has reached the [sample change] position, a table with your Total Carbon Concentration will appear.

n. Open the chamber cover by rotating the blue knob counter clockwise and sliding it over to the right. o. *CAUTION* sample boat will still be extremely hot, use the tweezers and carefully pick up the boat and place it on the hot plate.

p. To run another sample for TC analysis, repeat the previous steps as necessary.

Collecting IC

a. Return to the [Sample Table] and click on row number 1 where you inserted your first sample and make sure it is highlighted.

b. Select the [Start] icon located to the left on the second row of the [Sample Table Editor] window.

c. To run your first sample you will be required to name your Sample Table in the Thawspace (T:) Drive (e.g., Bob_Shales_2017_05_01).

d. Next, you will be prompted to enter the weight (mg) of your sample obtained from the balance. DO NOT PRESS START.

e. Carefully open the IC chamber by turning the green knob counter clockwise and slide the cover over to the right.

f. Place the boat on the metal sample boat holder, make sure it is aligned so that it fits securely in the boat holder.

g. Slid the cover back over the chamber and make sure it is tightened by rotating the green knob in the clockwise direction.

h. Return to the Enter Sample Amount screen and once the weight is input select [Start].

i. If all background conditions are met, a green [Ready] icon will appear on the top right window. Although you will be prompted to [Push the sample boat into the measurement position], *WAIT* First, pull up on the white plastic nozzle attached to the bottle of phosphoric acid and allow it to fully inject 0.4 mL of acid into the sample boat so IC reaction can occur.

j. Once the acid has fully injected into the sample boat, push the front green knob all the way forward to the measuring position.

k. To view your measurements, click the second blue icon in your sample window, it has an icon of a graph and a syringe.

l. Once your measurement is complete, you will be prompted to pull the boat back to the cooling position, this is the position located between the [sample change] and [measuring] position on the top panel of the instrument.

m. Once the boat has cooled sufficiently, you will be prompted to pull the boat back to the preparation position.

n. Once the sample boat has reached the [sample change] position, a table with your Inorganic Carbon Concentration will appear.

o. Open the chamber cover by rotating the green knob counter clockwise and sliding it over to the right. p. *CAUTION* sample boat will still be extremely hot and may have residual phosphoric acid, use the tweezers and carefully pick up the boat and place it in the beaker with yellow tape labeled Dilute Phosphoric Acid.

q. To run another sample for IC analysis, repeat the previous steps as necessary.

Saving Results

a. Once all TC and IC sample analysis has been completed you can compile a comprehensive report of all your data to save.

b. Select the [File] tab in the top menu bar, scroll down and select [Print] and scroll to the right and select [Sample Report-All]

c. Ensure that the printer is set to [Microsoft XPS Document Writer] and click [OK]

d. Save your file to the Thawspace (T:) Drive so that you can email yourself the results for use the UTA Box sync cloud service.

e. Once all analyses are saved it would behoove you to open up an MS Excel spreadsheet and create a table of all of your samples with TC in one column and IC in another to easily subtract them to get the sample TOC values. Remember: TOC = TC - IC

Appendix C- AP-608 Operating Procedures

1. GENERAL OPERATING PROCEDURES AND CALIBRATIONS

1.1. General Operating Guidelines

- It is highly recommended that the AP-608 be utilized with helium as the measuring medium; however, nitrogen can also be used when helium is not available.
- NOTE: Permeability measurements on samples less than 0.05 millidarcies should be made using nitrogen as the flowing gas to reduce errors.
- NOTE: Ambient (room) temperature should remain constant during any measurement procedure to within +/- 2 degrees C. If temperature changes more than 2 degrees during operation of this instrument, the accuracy of the data will be compromised.
- The optimum pressure setting for the confining fluid reservoir is 25 - 30 psi.
-To minimize measurement time with low permeability samples, plug diameter should be large (1.5 inches) and length short (<1.5 inches).
-To reduce measurement time with low permeability samples, the maximum fall off time can be reduced in the Configuration window. A complete pressure decay is not required to calculate permeability.
- To minimize thermal effects with high permeability plugs, small diameter (1 inch) and long lengths (>2 inches) should be used.
- For medium and high permeability core samples, an Equilibrium Timeout setting (Configuration Window) of one minute is sufficient. Low permeability core samples can take much longer to stabilize. When testing a low permeability core, setting the Equilibrium Timeout to 2 minutes or longer is advisable.
- When a core sample has been unloaded from the coreholder, no software commands should be entered until another core sample has been placed in the coreholder. One exception to this rule is the EXIT command.
-NOTE: It is recommended that the air gun at the side panel is used to blow out

the inside of the sleeve between every core sample tested. This will minimize the scratches to the end plugs due to rock dust.

1.2. Initial Filling of the Confining Pressure System with Fluid

To charge the coreholder with confining fluid, begin by loading the coreholder with a core sample or a stainless steel test plug. Do not use the software Load / Unload function for this procedure.

- Insert the solid steel plug in to the coreholder from the bottom.
-Follow the steel plug with the downstream end plug/end cap assembly. Turn the end cap until it is fully engaged. Do not over tighten.
- With one hand hold the locking mechanism back, and with the other hand lower the adjustable end plug down as far as it will go (until it meets the plug face). Caution – at least 1/3 of the axial nut threads must be engaged before lowering the adjustable end plug.
- At this point, the locking mechanism may or may not engage the ribbed shaft. In either case, turn the axial nut clockwise until the locking mechanism engages and the upper end plug is firmly in contact with the face of the plug.
- The recommended confining fluid is a 10:1 mixture of water and water-soluble oil.
- Prepare 500 ml of confining fluid by adding 50 ml of water-soluble oil to 450 ml of water (do not add water to oil). Stir solution until well mixed. Solution should be a white-milky color.
- Set the manual air regulator on the back panel of the instrument to zero.
- Remove the small plug from the top of the confining fluid reservoir (not the large nut) and carefully pour the confining solution into the reservoir. Replace the plug.
- Remove the plug located at the top, left side of the axial head assembly and replace with a plastic drain line. Place the other end of the plastic line in a flask or beaker to catch overflow.
- Adjust the confining fluid reservoir pressure regulator to apply 25 psi of air pressure.

- Using the control software, open valve 5. The air pressure will push confining fluid from the reservoir through valve 5 to the coreholder. The confining fluid will displace air from the system and the coreholder out through the plastic drain line.
- When confining fluid begins to flow out through the plastic drain line, close valve 5.
- Remove the plastic drain line and replace the plug.
- To purge any remaining air from the confining pressure intensifier, select Purge and then Fill. Repeat this sequence two or three times.

1.3. Preparing the Core Samples

Core samples should be clean and dry for best results. Core samples are usually cleaned with solvents and dried in an oven prior to gas permeability and/or porosity measurements. Oils are usually removed with hot toluene or xylene and salts are usually leached from the core samples with hot methanol. The samples are normally dried in a mechanical convection oven at a temperature of 240 degrees Fahrenheit for at least 12 hours or in a vacuum oven at 180 degrees Fahrenheit 82^{o}C) for a minimum of 4 hours for high permeability samples, 8 to 12 hours for moderate to low permeability samples. If clays or other water hydratable minerals are suspected, the samples should be cleaned with cool solvents and dried in a humidity-controlled environment at temperatures below 212 degrees Fahrenheit (100^{o}C) until stable weights are measured. (Usually clayey samples should be dried in a humidity oven at a temperature of 145 degrees Fahrenheit and a humidity of 45 percent.)

Core samples should be right cylinders. A core plug sample should posses perpendicular end faces to within +/- 0.005 inches for best results in the AP-608 permeameter-porosimeter. Any gap between the end face of the sample and the coreholder end plugs will be measured as pore volume/porosity. A good right cylinder is always the first step to quality petrophysical determinations.

1.4. Loading and Unloading a Core Sample into the Coreholder

1. All core samples should be precision right cylinders with end faces parallel to within +/- 0.005 inches.
2. If there is not a core sample already in the coreholder, skip to step 6. If there is a

core sample already in the coreholder, set the pressure intensifier to Load / unload. This will apply a vacuum to the confining sleeve in the coreholder. NOTE: The Load / unload function can only be used if a core sample is currently in the coreholder.

3. Turn the axial nut counter-clockwise to relieve any axial pressure.

4. With one hand, slide the locking mechanism back and with the other hand retract the adjustable end plug upward as far as it will go by pulling up on the upstream valve assembly (valve 6).

5. Turn the downstream end cap counter-clockwise until the lower end plug assembly can be removed from the coreholder. The core sample should drop out when the end plug is removed.

6. Insert a core sample into the coreholder from the bottom.

7. Follow the core sample with the downstream end cap / end plug assembly. Turn the end cap clockwise until it is fully engaged. Do not over tighten.

8. With one hand, slide the locking mechanism back (stretch the o-ring), and with the other hand, lower the adjustable end plug down as far as it will go (until it meets the core sample). Caution: At least 1/3 of the axial nut threads (at the top of the coreholder) should always be engaged before lowering the adjustable end plug.

9. At this point, the locking mechanism may or may not engage the ribbed shaft. In either case, turn the axial nut clockwise until the slide nut engages and the upper end plug is firmly in contact with the face of the core.

10. Connect the air lines, the PEEK gas lines, and the braided steel line to the valves before proceeding with a test. The longer lines go to the upstream valve and the shorter lines go to the downstream valve. The braided steel line goes to the quick connect fitting on the upstream valve.

11. To unload a core sample, start by reducing the confining pressure to atmospheric pressure.

12. Set the pressure intensifier to Load / unload. This will apply a vacuum to the

confining sleeve in the coreholder.

13. Turn the axial nut counter-clockwise to relieve any axial pressure.

14. With one hand, slide the locking mechanism back and with the other hand retract the adjustable end plug upward as far as it will go by pulling up on the upstream valve assembly (valve 6).

15. Turn the downstream end cap counter-clockwise until the lower end plug assembly can be removed from the coreholder. The core sample should drop out when the end plug is removed.

16. The coreholder will remain in the Unload condition until a new command is entered using the control software.

Appendix D- Nitrogen Gas Physisorption Procedure

First it is necessary to remove the moisture from the samples as volatile substances and free water will impede the ability for nitrogen molecules to adsorption onto the surface of the sample. This is done by degassing samples after the sample has been dried in an oven at 60^{o}C for 48 hours. The prepared sample (0.05g) is placed into the sample cell. Evacuation of air is performed. An isotherm tube is attached to the sample cell. Then the manifold and sample tube are also evacuated after the necessary amount of volume is reached. Once reached the liquid nitrogen is used to cool the manifold to -196.15^{o}C. This allows free space to be determined at the analysis temperature. The sample port is opened to allow nitrogen to adsorb onto the sample surface. The nitrogen pressure, temperature and the quantity of nitrogen gas removed from the manifold is recorded.

References

Aplin, A.C., J.K.S. Moore. 2016. Observations of pore systems of natural siliciclastic mudstones. *The Clay Minerals Society Workshop Lectures Series*. Vol. 21. Ch.3, 33-44.

Bertier, B., K. Schweinar, H. Stanjek, A. Ghanizadeh, C.R. Clarkson, A. Busch, N. Kampman, D. Prinz, A. Amann-Hildenbrand, B.M. Krooss, V. Pipich. 2016. On the use and abuse of N_2 physisorption for the characterization of the pore structure of shales. *The Clay Minerals Society Workshop Lectures Series,* Vol. 21, Chapter 12, pp.151-161.

Bragg, W.H.; W.L. Bragg. 1913. "The Reflexion of X-rays by Crystals". *Proceedings of the Royal Society* 88 (605): 428–38

Chong, K.K., B. Grieser. O. Jaripatke. A. Passman. SPE. Halliburton. 2010. A Completions Roadmap to Shale-Play Development: A Review of Successful Approaches toward Shale-Play Stimulation in the Last Two Decades. *Society of Petroleum Engineers*. SPE 130369.

Cole, R. D., R. G. Young, 1991, Facies characterization and architecture of a muddy shelf sandstone complex: Mancos B interval of the Upper Cretaceous Mancos Shale, northwest Colorado-northeast Utah, in A. D. Miall and N. Tyler, eds., Three-dimensional facies architecture of terrigenous clastic sediments and its implications for hydrocarbon discovery and recovery: *SEPM, Concepts in Sedimentology and Paleontology*, pp. 277-286.

Cole, R. D., R. G. Young, and G. C. Willis, 1997, The Prairie Canyon member, a new unit of the upper Cretaceous Mancos Shale, west-central Colorado and east-central Utah: *Utah Geological Survey,* Miscellaneous Publication 97-4, 23 pp.

Core Research Center, 2017 https://my.usgs.gov/crcwc/core/report/11085.

Cole, R. D., R. G. Young, and G. C. Willis, 1997, The Prairie Canyon member, a new unit of the upper Cretaceous Mancos Shale, west-central Colorado and east-central Utah: *Utah Geological Survey, Miscellaneous Publication* 97-4, 23 pp.

Curtis, M.E., B.J. Cardott, C.H. Sondergeld, C.S. Rai, 2012. Development of organic porosity in the Woodford Shale with increasing thermal maturity: *International Journal of Coal Geology, 103, pp.* 26-31

Drillinginfo.com. 2017. https://drillinginfo.com.

Gao, Z., and Hu, Q., 2012, Using spontaneous water imbibition to measure the effective permeability of building materials. *Special Topics & Reviews in Porous Media: An International Journal*, v. 3, p. 209.

Gao, Z., and Hu, Q., 2013, Estimating permeability using median pore-throat radius obtained from mercury intrusion porosimetry. *Journal of Geophysics and Engineering*, v. 10, p. 025014.

Guo, K., B. Zhang, K. Aleklett, and M. Hook, 2016. Production patterns of Eagle Ford Shale Gas: Decline Curve Analysis Using 1084 Wells. *Sustainability* 2016, 8, 973.

Hampson, G. J., J. A. Howell, and S. S. Flint, 1999, A sedimentological and sequence stratigraphic re-interpretation of the upper Cretaceous Prairie Canyon member ("Mancos B") and associated strata, Book Cliffs Area, Utah, *U.S.A. Journal of Sedimentary Research,* 69: 414–433.

Hu, Q.H., P. Persoff, J.S.Y. Wang. 2001. Laboratory measurement of water imbibition into low-permeability welded tuff. *Journal of Hydrology*, 242: 64-78.

Hu, Q.H., R. P. Ewing, and S. Dultz. 2012. Low pore connectivity in natural rock: *Journal of Contaminant Hydrology*, 133: 76–83.

Hu, Q., R. P. Ewing, and H. D. Rowe. 2015a, Low nanopore connectivity limits gas production in Barnett formation, *Journal Geophysical Research: Solid Earth*, 120: 8073-8087.

Hu, Q.H., X.G. Liu, Z.Y. Gao, S.G. Liu, W. Zhou, W. X. Hu, 2015b. Pore structure and tracer migration behavior of typical American and Chinese shales. *Petroleum Science* 12:651-663

Jarvie, D.M., 2014. Components and processes affecting producibility and commerciality of shale resource systems. *Geological Acta*., Vol. 12, N. 4. pp. 307-325.

Johnson, R. C., 2003, Depositional framework of the Upper Cretaceous Mancos Shale and the lower part of the upper Cretaceous Mesaverde group, western Colorado and eastern Utah, in Petroleum systems and geologic assessment of oil and gas in the Uinta-Piceance province, Utah and Colorado: *U.S. Geological Survey, Digital Data Series*, DDS-69-B, compact disk.

Katz, A., and Thompson, A., 1987, Prediction of rock electrical conductivity from mercury injection measurements. *Journal of Geophysical Research: Solid Earth*, v. 92, p. 599-607.

Kellogg, H. E., 1977, Geology and petroleum of the Mancos B Formation, Douglas Creek Arch, Colorado and Utah, in H.K. Veal, ed., Exploration Frontiers of the Central and Southern Rockies: *Rocky Mountain Association of Geologists*, pp. 167–179.

Kirschbaum, M. A., 2003, Geologic assessment of undiscovered oil and gas resources of the Mancos/Mowry total petroleum system, Uinta-Piceance province, Utah and Colorado, in Petroleum systems and geologic assessment of oil and gas in the Uinta-Piceance Province, Utah and Colorado: *U.S. Geological Survey, Digital Data Series*, DDS-69-B, compact disk.

Kopper, P. K., 1962, Douglas Creek Anticline and adjoining Area, in C.L. Amuedo and M. R. Mott, eds., Exploration for oil and gas in northwestern Colorado: *Rocky Mountain Association of Geologists*, pp. 108–110.

Philip, J.R., 1957. The theory of infiltration: 4. Sorptivity and algebraic infiltration equations. *Soil Science*. 84, 257–265.

Roberts, L.N.R., and Kirschbaum, M.A., 1995, Paleogeography of the Late Cretaceous of the western interior of middle North America—Coal distribution and sediment accumulation: *U.S. Geological Survey Professional Paper* 1561, 115 pp.

Sing, K. S. W., 1985. Reporting physisorption data for gas/solid systems with special reference to the determination of surface area and porosity: *Pure and Applied Chemistry*, 57(4): 603–619.

U.S. Department of Energy, National Energy Technology Laboratory. Modern Shale Gas A Primer. April 2009.

USGS, 2016. Assessment of Continuous (Unconventional) Oil and Gas Resources in the Late Cretaceous Mancos Shale of the Piceance Basin, Uinta-Piceance Province, Colorado and Utah, 2016. *U.S. Department of the Interior, Fact sheet* 2016-3030. June 2016.

Wang, S., Javadpour, F., and Feng, Q., 2016, Confinement correction to mercury intrusion capillary pressure of shale nanopores. *Scientific Reports*, v. 6, p. 20160.

Washburn, E.W., 1921, Note on a method of determining the distribution of pore sizes in a porous material. *Proceedings of the National Academy of Sciences of the United States of America*, v. 7, p. 115-116.